### 8.1.2.2 Melilites and related silicates

The silicates of melilite type are listed in Table 1 and classified according to Mineralogical Reference Manual as the group VIIIB02a [91N1, 99M1]. The silicates from group VIIIB02b have structures closely related to those of melilites. In the following the magnetic and related properties of silicates from both groups VIIIB02 will be reviewed. In addition to minerals, there are many synthetic samples which have compositions closely related to the melilites. Some of the above silicates will be considered in our discussion. We note that silicates from this group have potential applications as laser active materials [97S2].

#### 8.1.2.2.1 Crystal structure. Lattice parameters

Many melilite type compounds with the general formula $X_2T1(T2)_2O_7$ (X = Ca, Sr, Ba, Pb, Na, Y, Er. Tb); T1 = Be, Mg, $Mn^{2+}$, $Fe^{2+}$, Co, Cu, Zn, Cd, Al, $Fe^{3+}$, Ga, Si; T2 = Si, Ge, Al, $Fe^{3+}$, Ga, Be) have been synthesized either from a melt, by sintering or under hydrothermal conditions [58D1, 84D1, 90R1, 01B1]. Several crystal structure refinements on synthetic silicates have been published: $Y_2SiBe_2O_7$ [69B1], $CaNaAlSi_2O_7$ [70L1], $Ca_2MgSi_2O_7$ [81K1], $Ca_2Al_2SiO_7$ [82K2]; $Ca_2BeSi_2O_7$ [82K3]; $Sr_2MgSi_2O_7$ [83K1]; $Ca_2CoSi_2O_7$ [83K2]; $Sr_2Al_2SiO_7$ [84K1]; $Sr_2MnSi_2O_7$ [85K1]; $Ba_2MgSi_2O_7$ [95S1]; $BaCu_2Si_2O_7$ [01Y1]; $Ca_2VOSi_2O_7$ [01R1]; $Ca_2Zn(Ge,Si)_2O_7$ [90A1]; $Ca_2MgSi_2O_7$ [97Y1], etc. In addition, some natural melilites were studied: $(Ca,Na)_2(Mg,Al)(Si,Al)_2O_7$ [30W1], melilite [53S1, 96C2], $Ca_2Al(Al,Si)_2O_7$ [71L1], okayamalite, $Ca_2SiB_2O_7$ [00G1], etc. Many of the above silicates were considered as having tetragonal structure of $P\bar{4}2_1m$ type. This structure can be described as consisting of $T2_2O_7$ dimers connected via T1 cations in tetrahedra to form a sheet like arrangement [53S1]. These sheets are linked together by large cations X so that a general formula $X_2T1T2_2O_7$ results, as for example $Ca_2MgSi_2O_7$ - Fig. 1. In [86H1] satellite reflections and thermal behaviour anomalies in synthetic $Ca_2MgSi_2O_7$ were observed. In [87S1] were reported electron diffraction patterns and TEM images of synthetic iron-bearing åkermanites exhibiting two dimensional incommensurately modulated structure. They also suggested that the formation of the incommensurate phase is due to a structural misfit between tetrahedral sheet and X-polyhedral layer. In [90R1] the role of chemical composition in the stabilization of the incommensurate phase was pointed out. According to [93S1], the modulation amplitude is temperature dependent and the dynamic disorder of the X-cations may lead to the stabilization of the unmodulated melilite structure at high temperatures, only. From theoretical principles of the incommensurability in crystal [87J1], the incommensurate phases are intermediate between a commensurate high-temperature phase (unmodulated structure) and a low-temperature commensurate superstructure (the so called "lock-in phase").

The general reason for formation of temperature dependent modulation structures in melilites is the misfit between the intermediate cation layer and the sheet-like tetrahedral framework [87S1, 90A1, 90R1]. Direct evidence of this behaviour comes from structural studies of melilites with variable composition [90R1, 98J1]. Accommodation of the misfit strains within the lattice is provided by deformation of the tetrahedral layers via rotation about ***c*** of the tetrahedra within the $[T2_2O_7]$ dimers, rotation parallel and perpendicular to the layer planes and twisting of the T1 tetrahedra [92V1, 96T1]. The rotational distortions are accompanied by considerable atomic displacements. The most prominent displacements are those of the O atoms bridging T2-T2 and T1-T2 tetrahedra, which implicates even large distortions of the coordination polyhedra of the interlayer Ca atoms [93H1, 97Y1, 99M2, 00M1, 00R1]. According to recent interpretations, the incommensurate modulation of the melilites can be directly attributed to particular ordering schemes of low-coordinated calcium sites [00R1, 01H1]. A formal solution to the problem of modulated structure in melilites was provided by [99M2] indicating the coexistence of two structurally distinct components ($P\bar{4}$ and $P2_12_12$) in the incommensurate phase.

In the following the crystal structures of representative melilites and related silicates will be presented, as well as data concerning the transitions from normal (N) to incommensurate (IC) phase. The atomic coordinates and thermal factors for some representative silicates are given in Table 2, while the crystal structures and lattice parameters are listed in Table 3. In the last years new data concerning the crystal structures were reported. There are also different point of view concerning this matter. Consequently we present parallely the data obtained by various authors.

**Åkermanite, $Ca_2MgSi_2O_7$**

Åkermanite, $Ca_2MgSi_2O_7$, is the end member of the melilite group of minerals and usually occurs in igneous and metamorphic rocks, meteorites and blast furnace slags. The åkermanite and iron-åkermanite, $Ca_2(Fe,Mg)Si_2O_7$, exhibit an incommensurate (IC) structure at room temperature with modulations, having a wavelengh about 19 Å, along [110] and [1 $\bar{1}$ 0] and they undergo a reversible phase transition to a high-temperature normal (N) structure in the temperature range 353 K to 523 K, depending on composition [86H1, 87S1]. Because the modulated structure in åkermanite is only two-dimensional and stable over a wide range of temperatures, it has been the subject of a variety of experimental studies to understand the physical properties associated with displacively-modulated phases as: differential scanning calorimetry [86H1], adiabatic calorimetry [91I1, 94M1], X-ray electron and neutron diffraction [86H1, 87S1, 89I1, 92S2], optical diffraction [94I1], transmission electron microscopy [87S1, 89I1], differential thermal analysis [87S1], dilatometry [92W1], $^{29}$Si MAS NMR [89M1], ultrasonic wave propagation [90L1], dielectric constant measurements [92S1], Raman spectroscopy [88S1], EXAFS analysis [96T1] etc. A review of earlier studies of macroscopic and microscopic changes at the IC-N phase transition in melilites has been also given [93S1].

The crystal structure of the N phases of åkermanite is tetragonal and is described by the space group P $\bar{4}$ $2_1$m. This can be characterized by tetragonal sheets consisting of $[Si_2O_7]$ dimers interconnected by tetrahedrally coordinated Mg cations in the form of five-membered rings. These sheets lie parallel to the (001) plane and are linked together along ***c*** by large Ca cations in eight-coordination sites - Fig. 1 [97Y1]. The structure commonly used at room temperature, is the "basic" structure and corresponds to the "normal" phase. The distribution of Mg and Si over T1 and T2 sites has been described as being fully ordered [81K1].

Using the $^{57}$Fe NGR method, it has been found [87S1] that in $Ca_2(Fe,Mg)Si_2O_7$ there exist two distinct $[(Fe,Mg)O_4]$ tetrahedral sites, in modulated åkermanite, and that the two sites become less distinguishable as temperature approaches the phase transition critical temperature, $T_{IC\text{-}N}$ and merge into one site in the normal structure. The $^{29}$Si MAS NMR spectra of $Ca_2MgSi_2O_7$ [89M1] demonstrate the existence of three or more nonequivalent Si sites in an incommensurately modulated sample at 298 K. At elevated temperatures, these peaks merge into a single sharp peak at 380 K, characteristic for normal structure. According to [87S1, 93H1], the phase transition between IC and N structures is of second order.

The thermal expansion of $Ca_2MgSi_2O_7$ was analyzed by [86H1] in the temperature range 373…673 K and by [92W1] between 293 and 473K. The thermal expansions and spontaneous strains associated with IC phase transitions, in $Ca_2MgSi_2O_7$ and $Ca_2ZnSi_2O_7$, were reported by [92W1] - Figs. 2 and 3. For temperatures more than 10 K, above $T_{IC\text{-}N}$, the expansivities of both åkermanite and hardystonite are quite regular and were fitted with a relation of the form $\alpha = A+BT$ - Table 4. The phase transition from the normal to incommensurate phase with decreasing temperature is marked by a slight decrease in the *a*-dimension and a relatively large increase in the *c*-dimension leading to an overall increase in the unit cell volume. The behaviour at $T_{IC\text{-}N}$ is characteristic of a second or higher order phase transition. Below the phase transition (within ~ 10 K), the thermal expansion of the ***a***-axis rapidly achieves values approximately equal to those found in normal phase, whereas the ***c***-axis shows anomalously low and irregular expansivity throughout this temperature range. Three regions can be observed in thermal expansions.

The macroscopic spontaneous strain, defined as the deformation of the crystal with respect to the normal phase, with unit cell parameters calculated using the coefficients of thermal expansion found in the normal phase, were determined. At $T < T_{IC\text{-}N}$, there are two symmetrically independent linear spontaneous strains $\varepsilon_i = l_i/l_o\text{-}1$, where i refers to [100] or [001] - Fig. 3 [92W1]. There is a considerable strain for temperatures within 10 K of the phase transition, suggestive of a high-order phase transition. A small hysteresis of $\Delta l_{[101]}$ in the transition region was observed. For this reason in [92W1] the transition was classified as "weakly first order". The temperature dependences of the lattice parameters and cell volume, in the range 297 K…773 K, are given in Fig. 4 [01K2]. The data are rather similar to those obtained from dilatometric measurements - Fig. 2. The incommensurate phase undergoes a phase transition IC-N at 360 K.

The two-dimensional modulation of the synthetic åkermanite has been studied at low temperatures [02B1]. In the 18…297 K temperature range the incommensurate phase does not transform in the commensurate one. The first order component of the modulation wave vector *q* between 18 and 297 K varies by 0.0018 and the intensity of the satellite increases with decreasing temperature by 18 % as compared to the initial value at 297 K. Thus, the incommensurate state varies slightly in the 18…297 K temperature range.

The structural changes in $Ca_2MgSi_2O_7$, associated with pressure, were analyzed [97Y1]. The IC phase, stable at room temperature and pressure, transforms to the N phase at ~ 1.33 GPa. The structural transition is marked by a small but discernible change in the slopes of unit cell parameters, as function of pressure - Fig. 5. It is reversible with an apparent hysteresis and was classified as a tricritical phase transition. The linear compressibility of the ***a***- and ***c***-axes are $280(10)\cdot10^{-5}$ and $418(6)\cdot10^{-5}$ $GPa^{-1}$ for the IC phase and $299(11)\cdot10^{-5}$ and $367(8)\cdot10^{-5}$ $GPa^{-1}$ for N phase, respectively. No significant discontinuities in Si–O, Mg–O and Ca–O distances were observed across the transition, except for the Ca-O1 distance which is more compressible in the IC phase than in the N-phase. From normal pressure to 3.79 GPa, the volume of the $[SiO_4]$ tetrahedron is unchanged (2.16 $Å^3$), whereas the volumes of the $[MgO_4]$ and $[CaO_8]$ polyhedra decrease from 3.61 to 3.55(1) and 32.8 to 30.9(2) $Å^3$, respectively. Intensities of satellite reflections were found to vary linearly with the isotropic displacement parameter of Ca and the libration amplitude of the $[SiO_4]$ tetrahedron. At normal pressure, there is a mismatch between the size of the Ca cations and the configuration of tetrahedral sheets which appears to be responsible for the formation of a modulated structure. As the pressure increases, the misfit diminished through the relative rotation and distortion of $[MgO_4]$ and $[SiO_4]$ tetrahedra and differential compression of individual Ca–O distances, concurrent with a displacement of Ca along the (110) mirror plane toward the O1 atoms. The high-pressure normal structure was considered as a result of the elimination of microdomains in the modulated structure.

The elastic stiffness moduli, $c_{ij}$, of the $Ca_2MgSi_2O_7$ incommensurate phase, at room temperature, were measured on single crystal plates oriented parallel to (100), (001), (110) and (101) planes - Table 5 [90L1, 90L2]. In (010) and (001) planes, the compressional modulus from longitudinal wave is considerably larger than the shear moduli both from in-plane and perpendicular-to-plane shear waves. The relatively small values of the shear moduli indicate the ease of tetrahedral rotations in response to in-plane and perpendicular-to-plane shears and may provide preconditions for structural changes involving shears.

### $Sr_2MgSi_2O_7$

The amount of strontium in natural åkermanite, $Ca_2MgSi_2O_7$, rarely exceeds 1 wt % SrO [81F1, 83K1]. The $Sr_2MgSi_2O_7$ was synthesized, by solid state reaction [81F1], or from melt by the Czochralski method [82L1]. $Sr_2MgSi_2O_7$ crystallizes in a tetragonal structure of $P\bar{4}2_1m$-type [83K1] and is isomorphous with the high-temperature phase of $Ca_2MgSi_2O_7$. The tetrahedral Mg–O bond length (1.942 Å) is longer than that in $Ca_2MgSi_2O_7$ (1.915 Å) which exhibits the flexibility of the Mg(2a) site. The atomic coordinates and anisotropic thermal parameters are given in Table 2. At low temperatures the crystal structure changes into $P2_12_12$ space group [97K1, 98J1].

### Co–åkermanite, $Ca_2CoSi_2O_7$

The structure of Co-åkermanite was determined initially by [83K2] but no satellite reflections were reported. Later on, diffraction patterns of a synthetic sample revealed satellite reflections at room temperature [86H1, 87S1, 93H1]. Diffraction patterns of incommensurate phase indicate that each main reflection is surrounded by eight satellites reflections and the Laue classes for both main and satellite reflections are 4/mmm and the modulation is two-dimensional with two wave vectors $\boldsymbol{k_1} = q(\boldsymbol{a^*} + \boldsymbol{b^*})$ and $\boldsymbol{k_2} = q(-\boldsymbol{a^*} + \boldsymbol{b^*})$, along reciprocal lattice directions [110]* and $[\bar{1}10]$*. Then, all the reflections were indexed with five integers and five base vectors were related to the three crystallographic axes and two wave vectors $\boldsymbol{h} = h\boldsymbol{a^*} + k\boldsymbol{b^*} + l\boldsymbol{c^*} + m\boldsymbol{k_1} + n\boldsymbol{k_2}$, where $\boldsymbol{a^*}$, $\boldsymbol{b^*}$ and $\boldsymbol{c^*}$ are the base vectors of the reciprocal lattice of the basic cell (the unit cell derived from the main reflections) [93H1, 01H1]. Thus, the whole reflections were described in the (3+2) dimensional reciprocal space [74D1] with indices hklmn, where the multiplied integers are mn = 0 or ± 1. The basic structure is tetragonal of $P\bar{4}2_1m$ type. The averaged modulated structure is also tetragonal, $P\bar{4}2_1m$. The incommensurate modulation of the structure was mainly ascribed to rotations and deformations of the tetrahedral units of the layers that cause variation of the coordination numbers of Ca atoms from six- to eightfold. We note that a variety of coordination numbers of Ca has been also found in other compounds of the group [98K1, 00B1, 01K1]. Four arrays of sixfold coordinated Ca–O polyhedra surrounding a central array of $CaO_4$ tetrahedra form a bundle along [001] and many of those bundles are distributed in incommensurate structures so as to form octagons in the (001) projection of the structure [98K1].

The transition temperatures from incommensurate (IC) to normal (N) phase, $T_{IC-N}$, given by various authors are somewhat different. In [93H1] a value $T_{IC-N}$ = 489(5) K was determined, while in [99R1] a transition temperature of 498(1) K was reported. A $T_{IC-N}$ value, smaller by ~ 5 K than the above, was also mentioned [90R1]. In [01K2] a value $T_{IC-N}$ = 493 K was reported. The crystal structure of modulated åkermanite was then studied in a large temperature range [97R1, 99K1, 01H1]. The system is characterized by the presence of three phases. The parent phase was evidenced at temperatures above $T_{IC-N}$ (489…498 K) until it decomposes to Co-monticellite ($CaCoSiO_4$) and wollastonite ($CaSiO_3$) at 953 K and 1 bar [83K1]. The intermediate incommensurate phase is stable within a temperature range $T_{IC-N} > T \geq T_{LI}$. A lock-in phase transition to a low-temperature phase at $T_{LI}$ has been reported. A transition to a nearly commensurate phase ($q$ = 0.324) was described by [97R1] at $T_{LI}$ = 158 K and a transition to a commensurate phase ($q$ = 1/3) was observed at 242.3 K [99K1]. Assuming $q$ = 1/3, the former group presented a twinned model of tetragonal ($P\bar{4}$) fragments. The latter group reported a twinned structure of orthorhombic individuals $P2_12_12$ [01H1]. An analysis of the structure in the low-temperature range was performed also by [01S1]. According to the latter report, the behaviour at low temperatures is rather complicated as will be presented latter. According to [97R1], the phase transition was also accompanied by a hysteresis of $q$. In addition, a structure model assuming $q$ = 1/3 was presented [00R1]. Although the Laue class of the diffraction data was 4/mmm they assigned the space group $P\bar{4}$ to the structure, based on the violation of the extinction rule P-$2_1$- and interpreted that the high diffraction symmetry was caused by the presence of twinning in the crystal. During the high-temperature studies of the incommensurate phase of $Ca_2CoSi_2O_7$ [99K1] it was found that the hysteresis reported by [97R1] is observable in the whole stability range of incommensurate phase and the $q$ values vary from 0.286 (468 K) to 1/3 (below 242.3 K).

Since the $Ca_2CoSi_2O_7$ crystal is twinned and the apparent diffraction symmetry is 4/mmm, the structure parameters were obtained by a least-squares program for the refinement of twinned crystals [01H1]. The structure is essentially similar to that of the melilite group, but with regular arrangement of the bundles along [001]. A bundle is formed from four arrays of the sixfold-coordinated Ca–O polyhedra surrounding a central array of $CoO_4$ tetrahedra. The distribution of the bundles determined by [01H1] is different from that reported by [00R1]. The structure reported by [01H1] is essentially similar to the structure given by [30W1], but it is characterized by the ordered arrangement of bundles of the same sixfold-coordinated Ca atoms as in the incommensurate structures of the åkermanite group [98K1, 01K2]. 28.5 % of Ca atoms are sixfold-coordinated in the incommensurate phase at 297 K, while 44.4 % of Ca atoms are sixfold-coordinated in the commensurate structure and all of them form bundles. Four bundles are consequently included in each commensurate cell [01H1]. The octagonal distribution of the bundles characterizing the incommensurate structure was not found in the commensurate phase, but many fractions of the octagons (3/4 of an octagon) are scattered in the structure instead. The feature of the structure constructed with the space group $P\bar{4}$ is quite different from the structure of $P2_12_12$ type. The number of sixfold-coordinated Ca is eight in the commensurate cell and only one bundle is included in the unit cell. Thus, only 22.2 % of the calcium sites are sixfold coordinated and the number is less than that in the incommensurate structure. Many different commensurate structures with $q$ = 1/3 can be constructed with the arbitrary initial phases and they indicate various arrangements of the bundles, although the octagonal distribution is not realized. Almost all have the symmetry P1 and no systematic extinction is expected for the structure [01H1]. The structures with initial phases (0,0) and (1/2,0) of the (3 + 2)-dimensional space group were constructed with $q$ = 0.324 in order to compare them to the structures $P\bar{4}$ and $P2_12_12$ having $q$ = 1/3 [01H1]. The two structures with $q$ = 0.324 are similar to each other, in which the greater part of the structure is similar to the structure of $P\bar{4}$ type and the rest resembles the structure of $P2_12_12$ type. The average structure of these two parts may also be similar to the structure proposed by [00R1].

The incommensurate structure modulation of $Ca_2CoSi_2O_7$ was studied, at low temperatures, by high-resolution transmission electron microscopy (HRTEM) and electron diffraction (ED) [01S1]. The transition of the incommensurate to the commensurate lock-in phase exhibits a pronounced hysteresis of a highly strained metastable state with a characteristic microdomain morphology. A network of domain walls surrounding single orientation domains develop out of the room-temperature tartan pattern; the domains increase in size and their alignment changes from crystallographic to random. According to [01S1] the transition from the incommensurately modulated room-temperature phase into the lock-in phase does not occur spontaneously, but it is time- and temperature-dependent over a rather large temperature interval. Repeated heating-cooling regimes are indicative of remarkable hysteresis effects within temperature range 155 K $\leq T_{LI} \leq$ 270 K. Significant changes in TED patterns were observed starting at a temperature of ~ 140 K. After equilibration at 100 K, the

commensurately modulated low-temperature superstructure was observed, the phase transition being almost complete. The not exact commensurate data are in agreement with [00R1, 01H1]. In parallel, the evolution of the modulation structure was described by a change from a loose arrangement of octagonal tiltings into a close-packed configuration of overlapping octagons in the commensurate low-temperature lock-in phase. Thereby, the octagon represent the ordered distribution of low-coordinated Ca clusters within a nanodomain extending over 4 x 4 subunits on average [00R1]. The modulation wave vector was found to change from $\boldsymbol{k}_{1,2} = 0.295$ ($\boldsymbol{a}^* \pm \boldsymbol{b}^*$) at 300 to $\boldsymbol{k}_{1,2} = 0.320$ ($\boldsymbol{a}^* \pm \boldsymbol{b}^*$) at 100 K [01S1].

The temperature dependences of the lattice parameters and cell volumes for $Ca_2MgSi_2O_7$, $Ca_2CoSi_2O_7$ and $Ca_2(Mg_{0.55}Fe_{0.45})Si_2O_7$ were studied in the temperature range 297 and 773 K [01K2] - Fig. 4. The curves obtained for $Ca_2MgSi_2O_7$ and $Ca_2CoSi_2O_7$ show similar characteristics, although the transition temperatures $T_{IC\text{-}N}$ are different. The variation of each $\boldsymbol{a}$-axis gives no remarkable change around $T_{IC\text{-}N}$, but the data for the $\boldsymbol{c}$-axis reveals a steep depression around the transition temperature. The change of $\boldsymbol{c}$-axis in $Ca_2(Mg_{0.55}Fe_{0.45})Si_2O_7$ is different from the other two silicates. The depression recognized on the curves of the other two compounds is not distinct, but instead, bends are seen, at around the transition temperature - Fig. 4c. The structures of the incommensurate phase of the three silicates are characterized by the presence of the six-, seven- and eight-coordinated Ca–O polyhedra and an array of $T1O_4$ (T1: Co, Mg, Mg–Fe) tetrahedra in the structure. The number of bundles in each material decreases at elevated temperatures. The incommensurate phase undergoes a phase transition into the normal phase at 493 K in $Ca_2CoSi_2O_7$, and at 510 K in $Ca_2(Mg_{0.55}Fe_{0.45})Si_2O_7$. The features of the structures of the normal phase are almost the same as those found in the basic structures and this implies that the characteristics of the structures, such as the six-coordinated Ca–O polyhedra or fragments of the bundles, should be partially preserved at high temperatures both in incommensurate structures and also in the structures of the normal phase. The analysis of the anisotropic displacement parameter showed that the disorder of the modulation waves was developed in the structure at high temperatures.

The full symmetry and structure of the $Ca_2MgSi_2O_7$, incommensurate phase, was theoretically analysed [99M2]. The average structure shows that the oxygen atoms of the $SiO_4$ groups have large displacements in the (001) plane associated with a libration axis, for this group, parallel to the $\boldsymbol{c}$-crystallographic axis. The large displacement ellipsoid for O1, the linking oxygen in the $Si_2O_7$ group, requires that this atom is displaced from the two fold axes at 1/2, 1/2, 0 implying that this symmetry element cannot be retained in the incommensurate structure. The $Ca^{2+}$ ion also shows appreciable displacement normal to the mirror plane. In the incommensurate structure, the four $\boldsymbol{k}$ vectors ($\pm \boldsymbol{k}_1$ and $\pm \boldsymbol{k}_2$) lie in the mirror planes implying that the symmetry elements of the little co-group of $\boldsymbol{k}_1$ are $\{E \mid 000\}$ and $\{\sigma_{da} \mid 1/2\ 1/2\ 0\}$. This is the group of the order two with an even and an odd irreducible representation. Since the mirror plane must be lost, the full space group irreducible representation for the incommensurate structure are based on the odd representation of the little co-group. Then, the invariant subgroup was defined which turns individual $\boldsymbol{k}$ vectors into one another. It was concluded that the incommensurate structure must be based on the first two irreducible representations of the invariant subgroup of elements that take $\boldsymbol{k}_1$ into the other members of the star of $\boldsymbol{k}_1$ in melilite, as given below:

| $\{E \mid 000\}$ | $\{C_{2z} \mid 000\}$ | $\{S_{4z}^{+} \mid 000\}$ | $\{S_{4z}^{-} \mid 000\}$ |
|---|---|---|---|
| 1 | 1 | 1 | 1 |
| 1 | 1 | –1 | –1 |
| 1 | –1 | i | –i |
| 1 | –1 | –i | i |

The appropriate representations of the space group subgroup $G^{\pm \boldsymbol{kl}}$ is written:

$$G^{\pm \boldsymbol{kl}} = [\{E \mid 000\} + \{C_{2z} \mid 000\}] \cdot [\{E \mid 000\} + \{\sigma_{da} \mid 1/2\ 1/2\ 0\}]\ T \quad (1)$$

Since the invariant subgroup element $\{C_{2z} \mid 000\}$ which turns $\boldsymbol{k}_1$ into $-\boldsymbol{k}_1$ is even in both the relevant irreducible representations of the invariant subgroup, there is only one function associated with the translation subgroup in (1) which may be writen as $\cos \boldsymbol{k}_1 \boldsymbol{t}_1$. The complete space group subgroup is

$$G = \{E \mid 000\}\ G^{\pm \boldsymbol{kl}} + \{S_{4z}^{+} \mid 000\}\ G^{\pm \boldsymbol{kl}} \quad (2)$$

where the elements {E | 000} and $S_{4z}^{+}$ | 000} take ± $\boldsymbol{k}_1$ into ± $\boldsymbol{k}_1$ and ± $\boldsymbol{k}_2$, respectively. The element { $S_{4z}^{+}$ | 000} is even and odd, respectively, implying that in the first case the modulation functions cos $\boldsymbol{k}_1\boldsymbol{t}_1$ and cos $\boldsymbol{k}_2\boldsymbol{t}_2$ are locally in phase (+1, +1) and in the second case they are in antiphase (+1, –1). The modulation functions act to create local ordering alternatives $\eta$ and $\xi$. The order parameters $\eta$ and $\xi$ were associated uniquely with component structures $P\bar{4}$ and $P2_12_12$. It is obvious from the value of the reciprocal wave vector $\boldsymbol{k}$ that the two component structures are not degenerate and it is likely that the simple rotation ($P\bar{4}$) is the favoured structure of the pair. The fact that the two structures in melilite do not overlap in space, means that possible squaring up effects, within the modulation pattern, will occur with failing temperature, though this is unlikely to affect both structures equally. The model is in agreement with $^{57}$Fe NGR study of melilite [87S1] - see section 8.1.2.2.3. It was shown [99M2] that the model of [93H1] appears to be based on the even representation of the litle co-group of $\boldsymbol{k}$, i.e. the retention of the mirror plane, which is unlikely to be correct.

In [92V1] a microdomain model was envisaged for the modulated structure of melilite $Ca_2ZrGe_2O_7$, in which there were six distinguishable distortions of the T1 tetrahedron including the two distortions analysed above [99M2]. The structure within domains involved simple rotation of the T1 tetrahedra with a reversal of the sense of rotation across the domain boundary, where additional distortions were necessarily introduced. According to [99M2], the model is partly correct but is not compatible with the strict symmetry criteria developed by [99M2].

### $(Ca_{1-x}Sr_x)_2MgSi_2O_7$

As already mentioned, the space group of the average structure of åkermanite is $P\bar{4}2_1m$ [53S1]. Below 121 K, a lock-in phase maintaining the same space group has been proposed, while in case of $Sr_2MgSi_2O_7$ the symmetry obviously changes into $P2_12_12$ at low temperatures [97K1]. The temperature, $T_{IC\text{-}N}$, of the phase transition from incommensurately modulated structure to the parent high-temperature structure mainly depends on the composition. According to [90R1], the transition temperature should vary between about 297 K for x = 0.05 and values significantly below room temperature for x ≥ 0.125. The electron paramagnetic resonance (EPR) studies on $Ca_2MgSi_2O_7$ [96G1] and $(Ca_{1-x}Sr_x)_2MgSi_2O_7$ with 0.04 ≤ x ≤0.32 [97R1] doped with 1000 ppm $Mn^{2+}$, suggested that the incommensurate structure exists for all compositions at room temperature. In [98J1] by TEM and TED methods the same compositions were studied as in [97R1]. The TEM studies revealed incommensurately modulated structures at room temperature, for all compositions, in agreement with EPR data. Electron diffraction patterns show satellite reflections typical for two-dimensional modulation, and their successive destabilization with increasing Sr content. The amplitude of the modulation decreases with increasing Sr content until it vanishes at about x = 0.32. Just around this point, crystallization experiments have shown a phase separation to take place. The wavelength of the modulation was found to vary between 19.4 Å and 21.3 Å. There is a tendency of the Sr atoms to order in direct relation to the tartan-like modulation pattern. Hence, its spatial occupational distribution contributes to the incommensurate displacive modulation. The Sr ions incorporated into the incommensurate crystal phase are distributed in an ordered fashion and are partly adapted to the displacive modulation of the pure åkermanite. This means, occupational modulation even makes a contribution to the overall modulation characteristic in $(Ca_{1-x}Sr_x)MgSi_2O_7$ system.

### Hardystonite, $Ca_2ZnSi_2O_7$

The crystal structure of hardystonite, $Ca_2ZnSi_2O_7$, was reported to be tetragonal, having $P\bar{4}2_1m$ space group [30W2, 54S1, 69L1]. The zinc tetrahedra are located at the corners and base-center of the primitive tetragonal lattice. All four tetrahedral oxygen atoms are shared by adjacent silicon tetrahedra and the silicon tetrahedra are joined in pairs forming $Si_2O_7$ groups. The linkage of zinc and silicon tetrahedra results in an heterocyclic five-membered tetrahedral ring. The rings link together to form a corrugated sheet parallel to $\boldsymbol{c}$(001) and the adjacent sheets are held together by Ca–O bonds. The Zn–O bonding appear to have considerable covalent character [69L1]. Thus, the structure of hardystonite, can be summarized, as consisting of $[ZnSi_2O_7]^{4-}$ sheets within which the nature of bonding is dominantly covalent, the adjacent sheets being held together by $Ca^{2+}$ ions with the interlayer bonding predominantly ionic in character.

The synthetic [92W1] and natural [01B1] hardystonite[5)] (see Table 3) exhibits an incommensurate modulated structure. The incommensurate to normal transition temperature is $T_{IC\text{-}N}$ = 405 K [92W1]. The modulation is

two-dimensional, with tartan-like appearance; modulations vectors are $\boldsymbol{q}_1 = \alpha(\boldsymbol{a}_1^* + \boldsymbol{a}_2^*)$ and $\boldsymbol{q}_2 = \alpha(-\boldsymbol{a}_1^* + \boldsymbol{a}_2^*)$. A modulation wavelength $\lambda$ = 19.0(4) Å was estimated by centering satellite reflection using a single crystal diffractometer. The chemical composition of the natural sample was slightly inhomogeneous, with stronger and sharper satellites in the regions where the composition approaches to $Ca_2ZnSi_2O_7$ end-member. The average structure has space group $P\bar{4}2_1m$ [01B1].

The two-dimensional modulation in hardystonite has been studied [02B1]. The incommensurate phase does not transform to the commensurate one in the range 18 K ≤ $T$ ≤ 297 K. The difference in the first order component $q$ of the modulation wave vector in the above temperature range is six time larger than the increase in $Ca_2MgSi_2O_7$, and the satellite intensity increases to 4.6 times larger than the amount in Mg analogue - Fig. 6 [02B1]. The peculiarity of the temperature dependence in the component $q$ is the plateau-like region in the temperature range 60…169 K. The increase in the satellite intensity is also very small in this temperature range. Thus, the incommensurate phase of $Ca_2ZnSi_2O_7$ was classified into two kind of states: one with a specific $q$ = 0.2924(3) value, in a definite temperature range, and the other with a variable $q$.

The thermal expansions as well as the spontaneous strains of $Ca_2ZnSi_2O_7$, are plotted in Figs. 2 and 3, respectively [92W1]. Since of their resemblences, the above data were already discussed parallely with those obtained in åkermanite.

### $Ca_2Mg_{1-x}Fe_xSi_2O_7$

Phase relations in the system åkermanite-iron åkermanite have been summarized [74S1]. Stable solid solutions can be prepared up to slightly more than x = 0.80. With increasing iron content, the stability range of melilites narrows as the solidus temperature decreases and that of the subsolidus break-down temperature (into wollastonite and Ca-olivine) increases. The Fe end member can only be produced metastably, by crystallizing a glass, at low temperatures. The refined tetragonal lattice constants, measured at room temperature, on quenched samples, are given in Fig. 7 [87S1]. These refer to the "basic" melilite structure, i.e. the presence of satellite peaks and the doubling of the $c$ lattice constant for x = 0.8 have not been taken into account. The lattice constants $a$ display a more or less continuous S-shaped variation, whereas the apparent $c$ lattice constants show little change up to x ≅ 0.7 and then an abrupt drop where the $\boldsymbol{c}$-axis is actually doubled. At room temperature, an incommensurate phase with a modulation of a wavelength of about 19 Å in the [110] direction was observed. The compositional dependence of the melilite structural transition temperature, $T_{IC\text{-}N}$, is given in Fig. 8 [87S1]. Upon increasing the iron content, the temperatures at which they transform to a commensurante structure, increase. In addition to the T2 sites, filled by Si, the incommensurate phase exhibits two distinguishable T1 sites containing $Mg^{2+}$ and $Fe^{2+}$ (see section 8.1.2.2.3). These two sites merge into one site during the phase transition from the incommensurate to commensurate phase. In [87S1] a structural model was proposed for the incommensurate phase based on the misfit between the tetrahedral $(Mg^{2+},Fe^{2+})Si_2O_7^{4-}$ sheets and the $Ca^{2+}$ ions.

The temperature dependences of the lattice parameters and volume for $Ca_2(Mg_{0.55}Fe_{0.45})Si_2O_7$ silicate were plotted in Fig. 4 and analyzed comparatively with the data obtained for other melilites [01K2].

### $Ca_2Mg_{1-x}Co_xSi_2O_7$

The single crystals of åkermanite $Ca_2Mg_{1-x}Co_xSi_2O_7$ solid solutions were synthesized by the floating zone method [89I1]. In the whole range of x, they exhibit an incommensurate phase. When increasing x the wavelength decreases and the amplitude of modulation increases. The diffuseness of satellite was not observed in this system [89I1]. The transition temperatures, $T_{IC\text{-}N}$, increase from 356 K to 493 K when increasing x - Fig. 9a [91I1]. The composition dependences of the lattice constants of the average structure are given in Fig. 10 [96T1].

### $Ca_2Mg_{1-x}Zn_xSiO_7$

$Ca_2Mg_{1-x}Zn_xSiO_7$ forms solid solutions in all the composition range. The lattice parameters $a$ decrease while $c$ increases when increasing the Zn content - Fig. 11 [91I1]. The transition temperatures, $T_{IC\text{-}N}$, from IC to N phase increase with x, from 356 K to 403 K - Fig. 9b.

### $(Ca_{1-x}Sr_x)_2CoSi_2O_7$

The refined tetragonal lattice constants are given in Fig. 12 [90I1]. The lattice constants *a* increase almost linearly while the *c* values increase slightly concavely up to Sr/(Sr+Ca) close to 0.8 and then the increasing rate of both lattice constants decrease slightly. At room temperature, for $0 \le x \le 0.3$, the electron diffraction pattern revealed satellite reflections in the (hk0) plane. The satellite peaks, at RT, disappear at x = 0.3. The modulation wavelength in the [110] direction is 18.8 Å for Sr/(Sr+Ca) = 0 and increases up to 19.2 Å (Sr/(Sr+Ca) = 0.05), 19.9 Å (Sr/(Sr+Ca) = 0.15) and to 20.5 Å for Sr/(Sr+Ca) = 0.25 [91I1]. The transition temperatures, determined from specific heat measurements, are shown in Fig. 9c [91I1]. Although no modulated structure has been reported at room temperature for $(Sr_xCa_{1-x})_2CoSi_2O_7$ solid solutions for x > 0.3 [90I1], the presence of the modulated structure may be supposed at lower temperatures [00B1].

The incommensurate structure of $(Sr_{0.13}Ca_{0.87})_2CoSi_2O_7$, at room temperature, has been determined [00B1]. The silicate has also a non-centrosymmetric tetragonal basic cell with space group $P\bar{4}2_1m$. The two-dimensional incommensurate structure is characterized by the wavevectors $\boldsymbol{q}_1 = 0.286(3)(\boldsymbol{a}^* + \boldsymbol{b}^*)$ and $\boldsymbol{q}_2 = 0.286(3)(-\boldsymbol{a}^* + \boldsymbol{b}^*)$, were $\boldsymbol{a}^*$, $\boldsymbol{b}^*$ are the reciprocal lattice vectors of the basic structure with the (3+2) dimensional superspace group $P^{P42_1m}_{p4mg}$. The structure was described in terms of displacement of atoms, rotation, distortion of $CoO_4$ and $SiO_4$ tetrahedra and the partial ordering of the Sr and Ca atoms accompanied with the modulation. Correlated evolution of these features throughout the crystal gives rise to various oxygen coordination around Ca/Sr. The wavelength of the modulation, $\lambda$ = 19.41(3) Å, is higher than in $CaCo_2Si_2O_7$ and the amplitude of modulation is smaller. Comparison of the derived modulated structure to that of $Ca_2CoSi_2O_7$ clarified that the partial substitution of Ca by large alkaline-earth atoms such as Sr should decrease the distortion of the polyhedra around the cations.

The effects of substitution at the A-site, mentioned above, are similar to the usual temperature behaviour of modulated structure [00B1]. A change in the structural misfit by isomorphous substitution, as well as variation in temperature, affect the length of the modulation vectors. Expansion of the dimensions of the tetrahedral sheet, i.e. the size of pentagonal holes, stabilizes the low-temperature structural variants and contrary, the increase in size of A-cations stabilizes the high-temperature structural variants [90A1, 90R1].

### $Ca_2Co_{1-x}Fe_xSi_2O_7$

The peak intensity and the temperature of heat capacity anomaly, related to the IC-N phase transition, decreases with increasing Fe content and are not observed at x = 0.15, whereas the satellite reflections indicating an incommensurate phase are observed up to Fe/(Fe+Co) = 0.4 [91I1].

### Gugiaite, $Ca_2BeSi_2O_7$

The silicate gugiaite, $Ca_2BeSi_2O_7$, was assumed to have the crystal structure of the melilite group [62P1] and was later refined in a tetragonal structure, having $P\bar{4}2_1m$ space group [82K3]. Be and Si atoms are completely ordered in the tetrahedral sites.

### Gehlenites, $A_2Al_2SiO_7$ (A = Ca, Sr)

The gehlenite, $Ca_2Al_2SiO_7$, crystallizes in tetragonal structure of space group $P\bar{4}2_1m$. There are alternate layers of large Ca polyhedra with eight vertices, joined via edges and faces, and layers of tetrahedra of two sorts: T1(2a) and T2(4e) in the ratio 1:2. The T2 tetrahedra contains an unshared oxygen vertex which causes preferential filling of these positions by the higher charge $Si^{4+}$ cations and displacement of the low charge $Al^{3+}$ cations to the T1 sites. The rise of synthesis temperature can lead to disorder of the Al and Si over T1 and T2 tetrahedra [82K2, 85S1, 89S1]. According to [82K2], the degree of disorder, *w*, (the fraction of Si atoms in T1 positions), in gehlenite prepared at high temperature, is only 0.014. On the basis of structural modelling, the dependence of the degree of disordering on temperature was established and a value *w* = 0.12(2) for a sample obtained at 1300°C was estimated [85S1]. In case of a $Ca_2Al_2SiO_7$ sample, crystallized from glass at 1300(10)°C for 3 h or at 1000°C for 4 days, a value *w* = 0.14(4) was experimentally obtained [89S1]. This value is by one order of magnitude greater than that calculated for a single crystal from the interatomic distances [82K2]. The ordering of Al and Si in gehlenite was computer simulated [94T1]. The enthalpy of ordering $\Delta H$ per 2Al+2Si was found to be 0.52 eV; it is dominated by the nearest neighbor interaction.

The strontium gehlenite, $Sr_2Al_2SiO_7$, was firstly synthesized by [57D1], and later the crystal structure was analysed [60B1, 61D1, 84K1]. According to [84K1], synthetic Sr-gehlenite shows the same partial ordering, with Al in T1 tetrahedra and $Al_{1/2}Si_{1/2}$ in T2 ones, as in natural samples - Table 2. This Al/Si distribution is in agreement with that derived from the "bond valence" method [82B1]. Cross-hatched and lamellar structure observed in natural gehlenite are not caused by only Al/Si ordering. It was also concluded that the variations of the lattice parameters in melilites, due to the isomorphous ionic substitution, are caused mainly by the rotation of T1 tetrahedra and enlargement of T2-O1-T2 angles. The distortions of T1 and T2 sites in $Sr_2AlSiO_7$ are larger and smaller than those of T1 and T2 sites in $Ca_2AlSiO_7$, respectively [84K1].

In [78L1], gehlenite, $Ca_2Al_2SiO_7$, was compressed at 15…20 GPa and $T \cong 1000$°C in a laser heated diamond anvil. Transformation to one or more phases was observed. A structure having cubic cell ($a$ = 14.88(2) Å) has been shown. It was also noted that the structure can be indexed on a cubic cell, one-quarter of the above, with $a_0$ = 3.719(4) Å. The density of $Ca_2Al_2SiO_7$ thus produced was 8 % higher than the equivalent mixture of $CaAl_2O_4$ and $CaSiO_3$ and it was postulated that the structure should be more closely packed than is the normal perovskite structure [78L1], in which octahedral corners are shared. The analysis of the $Ca_2Al_2SiO_7$ structure, quenched from $p$ = 16 GPa and 1700° C, showed that the material was a mixture of $Al_2O_3$ and $Ca_2AlSiO_{5.5}$. The latter phase has a structure analogous to $CaSiO_3$ perovskite but with half the Si atoms replaced by Al, and charge balance provided by vacancies in the oxygen sublattice [91F1]. The lattice parameter, at ambient conditions, is $a_0$ = 3.706(3) Å.

### $Ca_2MgSi_2O_7$–$Ca_2Al_2SiO_7$

The crystal structure of the åkermanite-gehlenite solid solution series have been refined by neutron diffraction [92S2]. The results are consistent with the ordering scheme for tetrahedrally coordinated cations, represented by the structural formula $Ca_2[Mg_xAl_{1-x}][Si_{1+x}Al_{1-x}]O_7$, where by brackets are indicated the unequivalent tetrahedral sites. No evidence was found for the existence of phase transitions, in the samples with $x \leq 0.75$, in contrast to the behaviour found in pure åkermanite. Tentatively, it was concluded that the $P\bar{4}2_1m$ phase is the stable structure at all temperatures for compositions $x \leq 0.75$ [92S2].

### $Ca_2Zn(Ge_xSi_{1-x})_2O_7$

Single crystals of the melilite related structure in the CaO–ZnO–$SiO_2$–$GeO_2$ system were grown [90A1]. The $Ca_2ZnGe_{1.25}Si_{0.75}O_7$ silicate crystallizes in $P2_1/n$ space group. The tetrahedral layers are parallel to (101) and the stacking is along [101] (stacking period 10 Å). The tetrahedral layers are different to those of melilite, as the tetrahedra not only form five-membered rings, but also occur in four- and strongly distorted six-membered units. The layers are stacked in ABAB sequence, where the sheets A and B are symmetrically equivalent but shifted along $[\bar{1}01]/2$ with respect to each other. The tetrahedral sheet structure is characterized by two channel-types, running parallel to [101]. The first channel type is formed by the stacking of five-membered rings of tetrahedra, that are rotated relative to one another, Ca occupying this kind of channel being eight-coordinated. The second narrow channel-type is formed by an alternating sequence along [101] of four-membered and elongated six-membered rings. Ca between these rings is in distorted octahedral coordination.

### $(Ca,Na)_2(Mg,Al)(Si,Al)_2O_7$

$CaNaAlSi_2O_7$, called *soda melilite*, is the end member of some natural melilites having the composition $(Ca,Na)_2(Mg,Al)(Si,Al)_2O_7$. In these melilites, order-disorder of Mg, Al and Si among the tetrahedral sites and diadochy of Ca, Na, ... in the 8-coordination sites constituted the main interest [53S1]. Pure soda melilite is stable only when obtained at pressures in excess of 4 kbar [64Y1]. For example, in [70L1] $CaNaAlSi_2O_7$ was synthesized at 10 kbar. The atom coordinates and vibrational parameters are given in Table 2. The occupancy of the T1 sites is 0.245(3) which compares well with the ideal value of 0.250. This shows that T1, in soda melilite, is occupied by $Al_{1.0}$. The site occupancy of Si deviates only marginally from the ideal value of 0.5. From the above data was concluded that Al and Si atoms are ordered in the $P\bar{4}2_1m$-type structure, while Ca and Na atoms are disordered [70L1].

**Okayamalite, $Ca_2SiB_2O_7$**

Okayamalite, $Ca_2SiB_2O_7$, exhibits a melilite-type structure having space group $P\bar{4}2_1m$ [00G1]. Si and B are ordered on the T1 and T2 sites, respectively. The structure consists of layers of corner-sharing [$T1O_4$] and [$T2_2O_7$] groups resulting in an arrangement of tetrahedra with large pentagonal interstices projected along the ***c***-axis. Stacking of adjacent layers result in channels that are occupied by Ca cations. The latter are coordinated by eight oxygen atoms at the vertices of a distorted square antiprism. In comparison with the other melilite-type compounds, the cation population in okayamalite leads to the minimum structural misfit between tetrahedral and square-antiprism layers.

**Melilite solid solutions**

A large number of melilite solid solutions were studied. The crystal structure of some of them were already presented. In addition, we mention $Ca_2MgSi_2O_7$–$Sr_2MgSi_2O_7$ [83K1]; $Ca_2MgSi_2O_7$–$NaCaFe^{3+}Si_2O_7$; $Ca_2MgSi_2O_7$–$Ca_2Fe^{3+}AlSiO_7$; $Ca_2Al_2SiO_7$–$Ca_2Fe^{3+}AlSiO_7$; $Sr_2Al_2SiO_7$–$Sr_2Fe^{3+}AlSiO_7$ [85A1]; $Ca_2Ga_2SiO_7$–$Ca_2Fe^{3+}GaSiO_7$; $Ca_2MgSi_2O_7$–$Ca_2Fe^{3+}GaSiO_7$–$Ca_2Ga_2SiO_7$ [86A1]; $Ca_2MgSi_2O_7$–$CaNaAlSi_2O_7$; $Ca_2Al_2SiO_7$–$CaNaAlSi_2O_7$ [65E1], etc.

The tetragonal lattice parameters of the solid solutions are nearly linear dependent on composition [65E1, 83K1]. This result can be explained, for example, by ideal mixing of Ca and Na in the 8-coordinated sites in gehlenite-soda melilite system and the mixing of Mg and Al in T1 tetrahedral sites in the åkermanite-soda melilite system. In both types of solid solutions there are no substitutions in T2 site which is occupied by Si.

The site occupancy by various elements have been studied. In the åkermanite-type melilites: $Ca_2MgSi_2O_7$, $Ca_2BeSi_2O_7$, $Ca_2ZnSi_2O_7$, $Ca_2CoSi_2O_7$, $Sr_2CuSi_2O_7$, $Sr_2CdSi_2O_7$ and $Sr_2MgSi_2O_7$, $M^{2+}$ and $Si^{4+}$ occupy T1 and T2 sites, respectively [85A1]. On the other hand, in gehlenite-type melilites such as $Ca_2Al_2SiO_7$, $Sr_2Al_2SiO_7$ and $Ca_2Ga_2SiO_7$, T1 and T2 sites are occupied by Al or Ga and $Al_{1.0}Si_{1.0}$ or $Ga_{1.0}Si_{1.0}$, respectively [30R1, 67K2, 71L1, 82K2, 84K1]. According to [82K2], the smaller cations occupy T2 sites, while the larger ones prefer T1 sites. In synthetic melilite solid solutions such as $Ca_2MgSi_2O_7$–$NaCaFe^{3+}Si_2O_7$, $Ca_2MgSi_2O_7$–$Ca_2Fe^{3+}AlSiO_7$, $Ca_2Al_2SiO_7$–$Ca_2Fe^{3+}AlSiO_7$, $Sr_2Al_2SiO_7$–$Sr_2Fe^{3+}AlSiO_7$ [85A1], as well as in natural samples, divalent cations such as Mg, Be, Co, Zr or Cu occupy T2 sites, but not in the case of $Y_2SiB_2O_7$ [69B1].

According to [83K2], the cation distribution in tetrahedral sites of melilites is controlled by the avoidance of a great deficiency in the electrostatic valence. Later on, [85A1] has shown that if more than two kinds of trivalent cations are distributed both in T1 and T2 sites, the distribution of trivalent cations cannot be explained by this rule and it was suggested that the average ionicity of chemical bonding in T1 and T2 sites and the electronegativity of cations are additional factors controlling the distribution of trivalent cations between T1 and T2 sites - see also section 8.1.2.2.3.

For crystal structures and lattice parameters of melilites see also: $Ca_2MgSi_2O_7$ [61D1, 72K1, 81K1]; $CaNaAlSi_2O_7$ [70L1, 72K1]; $Ca_2Al(AlSi)_2O_7$ [71L1]; $Sr_2MgSi_2O_7$ [57D1, 60B1, 81K1, 82L1]; $BaBe_2Si_2O_7$ [77R1]; $Y_2SiB_2O_7$ [69B1]; $Ca_2Al_2Si_2O_7$ [61D1, 67K2]; $(Ca,Sr)_2(Mg,Co,Zn,Fe)Si_2O_7$ [91I1]; $Ca_2Al_2SiO_7$-$Ca_2MgSi_2O_7$ [65E1]; gehlenite-ferrigehlenite [78H1]; gehlenite-soda melilite-åkermanite [65S1]; melilite-åkermanite [80B1]; strontium-copper åkermanite [69I1]; leucophane-meliphanite [80B1].

**Fresnoites ($Ba_2TiSi_2O_8$, $Sr_2TiSi_2O_8$)**

Fresnoite, $Ba_2TiSi_2O_8$, is a non-centrosymmetric tetragonal crystal, having the space group P4bm. The fresnoite structure was determined by [67M1, 67M2, 69M1, 85M1]. This is formed by $Si_2O_7$ groups linked to square pyramidal $TiO_5$ members, producing layers parallel to {001}. The $Ba^{2+}$ cation, in ten-fold coordination, connects the layers - Fig. 13 [89C1]. The bonds within the sheet are predominantly covalent and the intersheet bonds are mainly ionic in character. The elastic properties of fresnoite are given in Table 5, and in Table 4 are listed the thermal expansion coefficients. Fresnoite in one of the few titanates that luminescences efficiently at room temperature and the explanation for this has centered on the short Ti-O interatomic distance within the $TiO_5$ group [79B1] The synthetic samples were grown by means of the Czochralski method [76E1, 76K1].

The structure of $Sr_2TiSi_2O_8$ is built of $[Si_2O_7]^{6-}$ double groups linked to Ti–O square pyramids to give flat sheets, and these stacks of sheets are held together by the large $Sr^{2+}$ ions which occur in coordination polyhedra, approximating to pentagonal antiprisms. The $TiO_6$ octahedra are deformed along their 4-fold axes. The larger deformation of the anionic polyhedral group leads to a high second order electric susceptibility [00Y1].

### $Ba_2VOSi_2O_7$, $Ba_{1.5}VOSi_2O_7$

The $Ba_2VOSi_2O_7$ and $Ba_{1.5}VOSi_2O_7$ silicates are isostructural with fresnoite [69M1]. The coordination of vanadium is similar to that of titanium in $Ba_2TiOSi_2O_7$, containing V–O bonds forming a square pyramidal coordination [01R2]. However, if the sixth oxygen (O4) belonging to V in the adjacent (001) layer was included, a highly distorted octahedral coordination around V can be seen in both compounds. The highly distorted octahedra are *trans* connected to produce alternating long and short V–O distances along the ***c*** direction. A similar highly distorted octahedral coordination was visualized for $Ti^{4+}$ in $Ba_2TiOSi_2O_7$ that was considered crucial [99G1] for nonlinear optical (NLO) material showing efficient second harmonic generation (SHG).

### $Ba_2Ti_{1+x}Si_{2-x}O_8$, $Ba_2TiGe_{2x}Si_{2-2x}O_8$

Solid solutions with $0 \le x \le 0.14$ have been identified [96C1]. If the excess of Ti in fresnoite substitutes directly for Si, then it is expected to occupy tetrahedral sites. The tetrahedrally coordinated $Ti^{4+}$ has been evidenced by IR measurements [61T1, 72D1, 96C1].

The phase diagram of $Ba_2TiGe_{2x}Si_{2-2x}O_8$ has been also analysed [78S1, 82I1].

### Jeffreyite, $(Ca,Na)_2(Be,Al)Si_2(O,OH)_7$

Jeffreyite crystallizes in an orthorhombic-type structure with space group $C222_1$ [84G1]. The large supercell is most likely due to ordering of some or all of the minor constituents, sodium, aluminium and the hydroxyl ion, into distinct atomic position.

### Lovdarite, $K_2Na_6Be_4Si_{14}O_{36} \cdot 9H_2O$

The lovdarite crystallizes in an orthorhombic type lattice. The reported space group was $P2_1$ [75K1] or Pma2 [81M2]. The lovardite structure may be described as a three dimensional framework of silicon and beryllium tetrahedra with alkali cations and water molecules in the cavities of the framework. The most outstanding feature of the structure is the arrangement of five tetrahedra in two three-membered rings sharing a tetrahedron. The strain is released by the presence of a beryllium cation in each ring [81M2].

### Nordite, $Na_3(Sr,Ca)(Ce,La)(Zn,Mg)Si_6O_{17}$

The asymmetric unit of the nordite cell, projected along the ***b***-axis, is given in Fig. 14 [70B1]. The atomic coordinates and their equivalents, which enter into coordination polyhedra - Table 2 - are marked. All large cations of rare-earths (R), (Sr,Ca), Na and (Na,Mn) occur at one level $0 \le y/b \le 0.01$ in the (010) plane, between two layers of O atoms at the levels $0.24 \le y/b \le 0.35$ and $-0.36 \le y/b \le -0.22$. To a first approximation, the coordination polyhedra around R, (Sr,Ca) and Na are square antiprisms (twisted cubes), which are eight corner polyhedra, whereas those around (Na,Mn) atoms are octahedra. The polyhedra are linked to form a compact layer by sharing 4 or 5 side (oblique) edges, and one face in the case of Na. The characteristic features of this layer are the quadrangular openings of two types and tetrahedral pits between the triplets of polyhedra. These pits, of two crystallographic types, are oriented in opposite directions. Such layers translationally repeated along ***b*** are connected at the levels $0.45 \le y/b \le 0.55$ by Si and (Zn, Mg, Fe, Mn) atoms, all being tetrahedrally coordinated by O atoms. The Si tetrahedra are found in three orientations with respect to the (010) layer, one of these sharply differing. Si1 and Si2 are perched above the mentioned tetrahedral pits and share three or one common O vertices with the layer of cations in accordance with their direct or opposite orientation. The Si3 tetrahedra are situated over the quadrangular openings between R-, (Sr,Ca)- and Na-antiprisms and the Na, Mn-octahedron. The crossing edges of Si3-tetrahedra pertain to different layers of cations.

Three kinds of Si tetrahedra can be distinguished by their orientation, being of the “face”-, “vertex”- and “edge”-types. (Zn,Mg,Fe,Mn) tetrahedra, or more precisely, those which are arranged over the larger openings are all of the “edge” orientation. All Si tetrahedra have one “free” corner and three which bridge to neighboring tetrahedra. The vertices of the edge Si tetrahedra are common to three Si tetrahedra of the face and vertex type, in the ratio 2:1 or 1:2; the face and vertex tetrahedra are connected to two Si tetrahedra and one (Zn,Mg,Fe,Mn) tetrahedron, the later having only bridging vertices. The shared corners result in the appearance of a continuous, approximately flat net of tetrahedra with four-, five- and eight-membered rings in the ratio 1:2:1. The structure of

nordite is closely connected with the structures of the melilite and datolite-gadolinite groups and may be considered as an unusual combination of both. According to the dominant content of rare-earth, these silicates were classified as Nordite-Ce and Nordite-La [91N1].

**Leucophane, $CaNaBeSi_2O_6F$**

The crystal structure of leucophane, $CaNaBeSi_2O_6F$ [67C1] is analogous to that of melilite [30Z1, 31Z1, 67N1, 89G1], but the ordering of pairs Ca/Na, Si/Be and O/F produces both the doubling of the ***c***-edge and the lowering of the symmetry from the space group $P\bar{4}2_1m$ to $P2_12_12_1$ [67C1]. In addition, it was suggested that the true symmetry could be still lower, i.e. P1, because of the slight differences observed in the intensities of the equivalent reflections and the presence of three forbidden h00 reflections with h odd. Later on, [69C1, 89G1] have confirmed the orthorhombic symmetry and suggested that the observed anomalies have to be imputed to double reflection effects.

The crystal structure of leucophane is described as follows: two layers of Si–O and Be–O tetrahedra, parallel to (001), are arranged in the unit cell. The Si1 tetrahedron shares its vertices with two Si2 and two Be tetrahedra, whereas both latter tetrahedra share only three vertices: two with Si1 tetrahedra and the third with either the Be tetrahedron (Si2) or the Si2 tetrahedron (Be). The unshared fourth vertex of the Si2 tetrahedron is occupied by O2, and that of Be tetrahedron by F. All atoms of the two layers of tetrahedra are nearly superposed along the [001] direction, in which Si1-Si1 and Si2-Be tetrahedra alternate. Also, Ca and Na atoms, which lie in holes between the layers of tetrahedra, alternate in the same direction. The atomic sites are given in Table 2.

The orthorhombic symmetry $P2_12_12_1$ of leucophane is lowered to triclinic P1 by the presence of rare-earths, R, which replace calcium (roughly one R atom for 16 calcium sites) in two of the four sites equivalent in the orthorhombic unit cell [92C1]. The increase of the positive charge due to presence of trivalent rare-earth ($R^{3+}$) replacing $Ca^{2+}$ is balanced by the substitution of some oxygen for fluorine. Only very small substitutions of beryllium for silicon (Si2 site), silicon for beryllium (Be sites), or calcium for sodium (Na sites) resulted from the refinement of the crystal structure. The shifts of actual positions, from those coherent with an orthorhombic symmetry, are very low [92C1].

**Meliphanite, $Ca(Na,Ca)BeSi_2O_6F$**

Meliphanite, $Ca(Na,Ca)BeSi_2O_6F$, crystallizes in a tetragonal structure having $I\bar{4}$ space group [30Z1, 31Z1, 67C1, 67D1]. The crystal structure consists of infinite sheets of $SiO_4$ and $BeO_4$ tetrahedra, between which Ca and (Na,Ca) are arranged; the coordination polyhedra of these cations are distorted trigonal prisms. The crystal structure of meliphanite is closely related to that of melilite and leucophane. In melilite, $Si_2O_7$ groups are present. They are held together by isolated $MgO_4$ tetrahedra to form twisted sheets of tetrahedra. Between these sheets the calcium atoms are located. In meliphanite the positions occupied in melilite by magnesium are not occupied by beryllium, but by a silicon atom, and beryllium occurs in a position that in melilite is occupied by a silicon atom. Thus, no $Si_2O_7$ group is present in meliphanite, but $SiO_4$ tetrahedra form intersecting zigzag chains that build up 16-membered rings, the centers of which are occupied by isolated $SiO_4$ groups that are connected with the rings through $BeO_4$ tetrahedra. As in melilite, the whole system of tetrahedra forms twisted sheets parallel to (001), which are held together by Ca and (Na,Ca) arranged between them.

**Other silicates having crystal structure related to melilites**

**$BaM_2Si_2O_7$**

The presence of $BaM_2Si_2O_7$ silicates with M = Be [77R1], Mg [70B2, 98Y1], Mn [70B2, 98Y1], Co [93A1], Zn [70S1, 99L2] was reported. $BaBe_2Si_2O_7$ crystallizes in an orthorhombic structure, in which the barium and oxygen atoms form an approximate h.c.p. array, $[BaO_7]$, and the silicon and beryllium atoms occupy the tetrahedral sites [77R1]. Alternatively, the crystal structure can be regarded as consisting of a framework of corner-sharing silicon and beryllium tetrahedra $[Be_2Si_2O_7]$ with the barium atoms occupying the tri-capped trigonal prism sites. The skeleton of the $BaCo_2Si_2O_7$ structure is also a three-dimensional framework of corner sharing tetrahedra $[Co_2Si_2O_7]$, however, the array of the $[BaO_7]$ is highly distorted from the h.c.p. symmetry,

owing to the large size of the cobalt ions. Unlike $BaBe_2Si_2O_7$, the $[CoO_4]$ tetrahedral units, in $BaCo_2Si_2O_7$, are joined by two common oxygen vertices, forming one-dimensional chains.

The structure of $BaMn_2Si_2O_7$ consists of a $[Mn_2Si_2O_7]$ tetrahedral framework - Fig. 15 - in which the $MnO_4$ groups are linked into chains along the ***c***-axis by sharing an oxygen atom. The $MnO_4$ chains are cross linked by $Si_2O_7$ groups forming a three-dimensional structure and the barium atoms are located in a channel formed in the $[Mn_2Si_2O_7]$ tetrahedral framework with a distorted cube coordination [93A1, 98Y1, 99L2, 00L1].

The $BaCo_2Si_2O_7$ silicate crystallizes in a structure having space group C2/c [93A1]. Each cobalt ion is surrounded by four oxygen atoms arranged in a distorted tetrahedra. The tetrahedra are linked into chains through the sharing of one of the oxygen atoms. The $CoO_4$ chains are cross linked by bridging $Si_2O_7$ groups. The barium ions occupy channels that run parallel to the crystallographic ***c***-axis.

$BaZn_2Si_2O_7$ undergoes a first order phase transition of about 523 K [99L2]. The low- temperature (LT) phase is iso-structural with $BaCo_2Si_2O_7$. It crystallizes into a monoclinic structure having space group C2/c. The structure of the high-temperature (HT) phase is orthorhombic having space group $Ccm2_1$. The structures of the LT and HT phases are quite similar. In Fig. 16 the crystal structure of the LT phase projected along the ***a***-axis and of the HT phase projected along the ***a*** and ***c***-axes are shown. The crystal structure of the LT phase is composed of the tetrahedral framework $[Zn_2Si_2O_7]$ and isolated Ba atoms. Two silicon tetrahedra are connected by sharing an oxygen forming a di-silicate group, $Si_2O_7$. The di-silicate groups further share corners with the Zn tetrahedra, forming a three-dimensional framework. The tetrahedral framework, $[Zn_2Si_2O_7]$ is arranged in a manner such that six-membered ring channels are formed running parallel to the ***c***-axis. The six-member ring is not a regular hexagron, but rather is a "rugby-ball" shaped. All the barium atoms are located in the channel and coordinated by oxygen atoms in both types of structures. The geometries of di-silicate groups, $Si_2O_7^{6-}$, in the LT and HT structures, are different. In the HT structure, the Si-O-Si angle of $Si_2O_7^{6-}$ is about 132.5°, while in the LT phase, this angle reduces to 124.8°. In addition to the connection with di-silicate groups, the Zn-tetrahedra are linked via corner-sharing to form one-dimensional chains parallel to the ***c***-axes. The Zn-chains are almost linear in the HT phase and are wriggled in the LT phase. Although the inter-chain Zn-Zn distance, in HT phase, is almost as short as the intra-chain distances of the LT phase, the bond connection is different. The connection of the Zn atoms within the chain is through the sharing of an oxygen atom, i.e., through Zn–O–Zn. The connection of the Zn atoms between the chains, however, is through Zn–O–Si–O–Zn. Therefore, the Zn tetrahedra can still be considered as a one-dimensional chain. The one-dimensional character of the M-tetrahedron is of interest for magnetic ions, such as $M^{2+} = Co^{2+}$ or $Mn^{2+}$, with regard to magnetic interactions along the chains. Although all the Ba atoms are located inside the channels of the framework, the local coordination geometry is different for the LT and HT structures. The configuration of the di-silicate groups surrounding a barium atom in the HT phase seems to be more symmetrical; but only five oxygen atoms are bonded to a Ba atom. The Ba–O bonds form a square pyramidal polyhedron. In the LT phase, the di-silicate groups are tilted, but the coordination polyhedron of the barium atom becomes more regular. The lower coordination number of Ba atoms and the breaking of the Ba–O bonds in the HT phase may account for the endothermal behaviour of the phase transition. The temperature dependences of the cell parameters are plotted in Fig. 17 [99L2]. Below 523 K only the LT phase exists and above 563 K the silicate converts to the HT phase. At about 523 K, these phases coexist. The thermal expansion along the ***c***-axis is larger than that along the ***b***-axis. The lattice constant *a* decreases with increasing temperature. Around the transition temperature, a discontinuous change in the unit cell volume is observed, indicating the first order nature of the phase transition.

**$BaCu_2(Si_{1-x}Ge_x)_2O_7$**

The crystal structure of $BaCu_2Si_2O_7$ was solved by [90J1]. The silicate crystallizes in a Pnma-type structure. The key units are obviously $CuO_4$ squares (or flattened $CuO_4$ tetrahedra) and $Si_2O_7$ groups made of a pair of corner shared $SiO_4$ tetrahedra. The $CuO_4$ squares are connected to each by their corners, forming 1D chains along the ***c***-axis (see section 8.1.2.2.2). Note that they are heavily corrugated to an intrachain Cu–O–Cu bond angle $\theta$ of 121° for $BaCu_2Si_2O_7$ and 128.4° for $BaCu_2Ge_2O_7$. $BaCu_2(Si_{1-x}Ge_x)_2O_7$ forms solid solutions in all the composition range. The observed lattice expansion with increasing x - Fig. 18 - can be ascribed to the smaller ionic radius of $Si^{4+}$ (0.26 Å) as compared to $Ge^{4+}$ (0.39 Å) [01Y1]. The expansion along the chain direction ***c*** may result from the change in bond angle $\theta$. It can be expected that the chains with $\theta = 120°…130°$, in the

present compounds possess rather large antiferromagnetic couplings though these must be significantly smaller than those for the linear chains.

**$Ba_2MSi_2O_7$, $KHoCoSi_2O_7$**

The crystal structures of $Ba_2MSi_2O_7$ with M = Cu [84M1] or M = Fe [72F1] were studied. The structure of $Ba_2CuSi_2O_7$ can be described by using three kinds of polyhedra. The Ba atoms are located in irregular eight-vertex polyhedra, with almost flat upper and lower bases (along the ***c***-axis), that are pentagonal and trigonal, respectively. The Cu and Si atoms occupy slightly distorted tetrahedra. The basis of the structure consists of massive layers of Ba eight-vertex polyhedra that are joined by shared edges and lie approximately on one level along the ***c***-axis in the (*ab*) plane of the cell. Such large cation layers alternate along the ***c***-axis with layers of tetrahedra. The silicate tetrahedra are condensed into a diorthogroup by a bridge O atom lying on a twofold axis. The vertices of the $[CuO_4]$ tetrahedron link the diorthogroups into a plane network of composition $[CuSi_2O_7] = [T_3O_7]$. The free vertices of the $[SiO_4]$ tetrahedra are turned alternately to either side of the network, imparting a distinct polarity to the structure. The tetrahedral $[T_3O_7]$ network is characteristic for melilite-åkermanite groups.

The structure of $KHoCoSi_2O_7$ [80R1] is similar to $Ba_2CuSi_2O_7$ and is formed of $[Si_2O_7]$ diorthogroups and "special" $[CoO_4]$ tetrahedra. It is this network which is topologically identical to that in $Ba_2CuSi_2O_7$. Replacement of K and Ho by BaBa leads only to centering of the unit cell and to a change of the symmetry group, while replacement of Co atoms by Cu ones, in the $[T_3O_7]$ network, leads to a slight deformation of this special tetrahedron as result of the Jahn-Teller effect.

**$R_2Si_3O_3N_4$, where R is yttrium or rare-earth**

Yttrium silicon oxynitrides are formed when yttrium oxide is used to promote sintering in silicon nitride and sialons (= Si, Al, O, N) [86B1, 94C1, 95S2]. $Y_2Si_3O_3N_4$, one of the most commonly encountred compound in sintering, is named N-melilite, because of its similarities with melilite-type silicates. The suggested structure of $Y_2Si_3O_3N_4$ was derived from åkermanite by substitution of Ca by Y, of Mg by Si and of four of the seven oxygen atoms by nitrogen. The positions of Y and Si atoms are well established - Table 2. The O/N distribution has been a subject of discussion [84R1, 86B1, 86S1, 96K1, 96M1, 97W1, 97W2, 98D1, 00F1]. Three different models concerning the occupation of the anions have been suggested: I (O2c, O4e, N8f); II (O/N2c, O/N4e, O/N8f); III (N2c, O4e, O/N8f) [00F1]. In [84R1], analyzing the structure of $R_2Si_3O_3N_4$ melilites, it was suggested that the favoured structure is that in which O atoms are at 2c and 4e sites, while N atoms are at the 8f site with two Si atoms (at 4e) in a $SiO_2N_2$ tetrahedron and the third Si (at 2a) forming a $SiN_4$ tetrahedron - Fig. 19 [00F1]. This model was used for the refinement of the structure of $Y_2Si_3O_3N_4$ [97W1]. By $^{29}Si$ MAS NMR measurements [98D1] was found a single broad peak at about –56.7 ppm, which was related to the $SiO_2N_2$ clusters. It was suggested that N atoms would partially occupy the 4e site and of importance is partial occupation of the 8f site by oxygen to removing presence of $SiN_4$ tetrahedra. In [96M1] was reached a satisfactory refinement by assuming that the anion sites are occupied randomly by O/N (model II). The $^{15}N$ NMR studies [96K1] suggested that N atoms occupy the bridging site 2c, and O atoms occupy the terminal site 4e (model III) in the two $Si_2(O,N)_7$ units with Si at 4e, while for the remaining two tetrahedra for Si at 2a in the unit cell, oxygen and nitrogen atoms (at 8f) are disordered but with an overall composition of three nitrogen and one oxygen in each tetrahedron ($SiON_3$). An O/N ordering at the 8f site was proposed according to the intensity of the three peaks in the $^{15}N$ NMR spectra [00F1]. In [97W2] the O/N ordering was investigated by neutron diffraction. It was found that the 2c site was occupied by 1.7 N and 0.3 O, while the remaining 6.3 N atoms were disposed at the 8f site. They preferred the model III. These conclusions were also drawn from X-ray single crystal determination of the $Sm_2Si_3O_3N_4$ structure [99L1]. In [00F1] has been shown theoretically that N atoms fully occupy the bridging site (2c) and O atoms fully occupy the terminal site (4e) with 2O and 6N atoms at the bridging 8f site, in agreement with neutron diffraction studies [97W2]. In addition, the calculations show that there is a preferential distribution of the O and N atoms at the 8f site, resulting in two different local coordination of Y, as compared to only a single averaged crystallographic Y site.

**$Y_2SiBe_2O_7$**

Diyttrium beryllate, $Y_2SiBe_2O_7$, is tetragonal, having space group $P\bar{4}2_1m$ [69B1]. Y atoms lie, within distorted square oxygen antiprisms and silicon atoms, in isolated $SiO_4$ tetrahedra. Beryllium atoms occupy distorted tetrahedra linked at one corner to form double $Be_2O_7$ pyramids oriented upward and downward relative to the ***c***-axis. The compound is isostructural with silicate minerals of the melilite family. The $M_2O_7$ group is capable of accepting various small ions of different valences, giving this structural arrangement of remarkable versatility.

**$Na_2Mn_2Si_2O_7$**

$Na_2Mn_2Si_2O_2$ crystallizes in a monoclinic structure having space group $P2_1/c$ [67A1]. The cell is formed from 4 molecules, i.e.8 magnetic atoms. There are two types of lattice sites for Mn ions with different oxygen environment. The $Mn1^{2+}$ ions are situated in the center of distorted tetrahedra, formed by four $O^{2-}$ ions. The $Mn2^{2+}$ ions are situated in centers of triangular prisms.

**$Li_6[Si_2O_7]$**

$Li_6[Si_2O_7]$ crystallizes in a tetragonal lattice having $P\bar{4}2_1m$ space group [69W1].

**$Na_2Si[Si_2O_7]$, $Li_2Si_3O_7$, $SiP_2O_7$**

*$Na_2Si_3O_7$* was prepared by [89K1, 95F1]. The single crystals have been grown in the presence of melt at 9 GPa and 1200°C [95F1]. The silicate crystallizes in a monoclinic structure having C2/c space group. Silicon occurs in both tetrahedral and octahedral coordination ($^{[6]}Si : {}^{[4]}Si = 1 : 2$). The $SiO_4$ tetrahedra form a diorthosilicate $[Si_2O_7]$ group and are linked by isolated $SiO_6$ octahedra via shared corners into a framework of 6-membered ($^{[4]}Si - {}^{[4]}Si - {}^{[6]}Si - {}^{[4]}Si - {}^{[4]}Si - {}^{[6]}Si$) and 4-membered ($^{[4]}Si - {}^{[6]}Si - {}^{[4]}Si - {}^{[6]}Si$) rings:
$< {}^{[6]}Si - O > = 1.789$ Å, $< {}^{[4]}Si - O >= 1.625$ Å; $^{[4]}Si - O - {}^{[4]}Si = 132.9°$ and the bridging oxygen is overbonded (s = 2.22) [95F1]. Channels parallel to the ***b***-axis and [110] accommodate Na in irregular 6-fold coordination. The $Na_2Si_3O_7$ structure has some topological similarity to the structure of the melilite group (e.g. åkermanite, [53S1]) in which the tetrahedral groups are linked via shared corners to form 5-membered ($^{[4]}Si - {}^{[4]}Si - {}^{[4]}Mg - {}^{[4]}Si - {}^{[4]}Mg$) rings. Melilite phases have analogous stoichiometry to sodium trisilicate. There is even closer topological similarity with the structure of *$SiP_2O_7$* [79H1] in which the sixfold coordination of Si is induced, at normal pressure, by a compositional control. This is built of a framework of 5-membered ($^{[4]}P - {}^{[4]}P - {}^{[6]}Si - {}^{[4]}P - {}^{[6]}Si$) rings. The tetrahedral and octahedral groups are again linked via shared corners. According to [91F2], the $Na_2Si_3O_7$ structure belongs to the group of structures characterized by both tetrahedral and octahedral Si and is stable at about 10 to 20 GPa.

The crystal structure of $Li_2Si_3O_7$ was reported to be orthorhombic [70W1].

For crystal structure of other silicates see Table 3 as well as the reports on $Na_3TmSi_2O_7$ [85S2], $Na_3(YSc)Si_2O_7$ [79M1].

### 8.1.2.2.2 Magnetic properties. Neutron diffraction data

**Gehlenite**

The temperature dependence of the magnetization in Fe-doped gehlenite in a field of 0.3 T is plotted in Fig. 20 [83N1]. The maximum magnetization, at 4.2 K, in a field of 7 T, where an asympthotic approach to saturation was shown, is 1.12 emu. At low external field and 278 K it was concluded that different magnetic domains occur which must be postulated as consisting of mutually interacting antiparallel spins. The hysteresis loop is very small. An ordered state for gehlenite with many parallel spins is only reached at low temperature, but whether the magnetic order observed for gehlenite is a consequence of the tetrahedral groups (which are arranged in sheets) remains to be understood. It can be only supposed that the observed magnetization and small hysteresis arise from the structural pecularities of the disordered iron doped melilite structure [83N1].

**$BaMn_2Si_2O_7$**

The distances between Mn atoms, in the $MnO_4$ chain, are not equally distributed, but appears in an alternative fashion, with the Mn-Mn distances of 3.398 and 3.636 Å - Fig. 15 [00L1]. The interchain Mn-Mn distances are 3.226 Å and 3.686 Å, smaller than those of the intrachain distances. Within the chains, the manganese atoms are connected by sharing an oxygen atom at the tetrahedral corner (Mn–O–Mn), while the Mn atoms between the chains are linked through Mn–O–Si–O–Mn. The intrachain magnetic interaction should be therefore much stronger than that of the interchain interaction.

The temperature dependences of the magnetic susceptibility and of the effective magnetic moments are plotted in Fig. 21 [00L1]. The broad maximum near 60 K in the susceptibility is typical for a linear Heisenberg antiferromagnetic behaviour, describing the magnetic coupling along the individual chains of Mn ions. In the 20 K $\leq T \leq$ 160 K temperature range, the fit with a one-dimensional model [69D1] give $J/k_B = -7.41$ K and $g = 1.98$. The increase of $\chi$ values at $T < 20$ K is expected to be due to long-range ordering between the chains. In the low-temperature range, the magnetic coupling between the chains is non-negligible and thus the system becomes two-dimensional [00L1].

**$BaCo_2Si_2O_7$**

The magnetic moments, at 12 K and 18 K, increase rapidly with the field to a saturation value $p \cong 0.4$ $\mu_B$/Co atom - Fig. 22a [93A1]. At 2.5 K and 5 K there is a little increase up to a field of 0.2 T and 0.05 T, respectively [93A1]. The temperature dependence of the magnetic susceptibility shows a broad maximum at ≈ 35 K and for $120 < T < 220$ K a Curie-Weiss type behaviour was evidenced - Fig. 22b. The paramagnetic Curie temperature is negative, $\Theta = -46$ K. There is an antiferromagnetic coupling of the spins between nearest neighbor cobalt. According to [93A1], the silicate undergoes a three-dimensional magnetic transition, into a field induced weak ferromagnet, that is characteristic of a one-dimensional metamagnet.

**$Na_2Mn_2Si_2O_7$**

The $Na_2Mn_2Si_2O_7$ crystal is magnetically isotropic at $T > 26$ K [67K1]. In the temperature range 100 K $< T <$ 300 K, a Curie-Weiss type behaviour is evidenced - Fig. 23. A very diffuse susceptibility peak is observed at 60 K - Fig. 23c. It was suggested that the peak is due to the appearance of antiferromagnetic ordering within the $Mn^{2+}$ ion groups. An uniaxial anisotropy of the magnetic susceptibility and a ferromagnetic moment appear below 26 K - Fig. 23a. This was attributed to a transition at an antiferromagnetic state with weak ferromagnetism. The magnetic data are given in Table 6.

**$Ba_2VOSi_2O_7$, $Ba_{1.5}VOSi_2O_7$**

The temperature dependences of the magnetic susceptibilities for the above compounds are plotted in Fig. 24 [01R2]. In case of $Ba_{1.5}VOSi_2O_7$, the vanadium is in the $V^{5+}$ state ($3d^o$), the silicate showing diamagnetism. The susceptibility is not temperature dependent. For $Ba_2VOSi_2O_7$ the magnetic susceptibilities follow a Curie-Weiss behaviour. The effective moment of 1.73 $\mu_B$/V ion suggests that vanadium has $3d^1$ ($V^{4+}$) configuration.

**$BaCu_2(Si_{1-x}Ge_x)_2O_7$**

The temperature dependences of the magnetic susceptibilities of a $BaCu_2Si_2O_7$ single crystal along ***a***, ***b*** and ***c***-axes are shown in Fig. 25 [99T1]. Below 9.2 K a substantial drop was observed in $\chi_c$, while both $\chi_a$ and $\chi_b$ change little from 9 K to 2 K. This points to the presence of an antiferromagnetic long-range order below $T_{N1} =$ 9.2 K, with the crystallographic ***c***-axis being the magnetic easy axis of the system. At $T \rightarrow 0$, $\chi_c$ retains substantial nonzero value, suggesting a reduction of ordered moment, presumably due to the 1D nature of the system. The one-dimensional character of the magnetic behaviour is also observed in the paramagnetic phase; the susceptibility shows a broad maximum around 180 K along all the three crystallographic directions. Fitting these data with a Bonner-Fisher (BF) curve [64B1] and assuming an anisotropic $g$ factor, values $g_a = 2.5$ and $g_b = g_c = 2.2$ were obtained [99T1]. We note that by fitting the thermal variation of the susceptibility for a polycrystalline sample with a BF curve a value $g = 2.1$ was obtained [00Y1]. According to [00Y1] the critical temperature of $BaCu_2Si_2O_7$ is somewhat lower, $T_{N1} = 8.9$ K.

Some magnetization isotherms for $BaCu_2Si_2O_7$ and $BaCu_2Ge_2O_7$ are plotted in Fig. 26. [01Y1]. The field dependence of magnetization for $BaCu_2Si_2O_7$ is nearly linear at 5 K, in agreement with antiferromagnetic ordering, while $BaCu_2Ge_2O_7$ shows a nonlinear variation revealing the presence of weak ferromagnetism.

The magnetic structure determined by neutron diffraction experiments in $BaCu_2Si_2O_7$ [99T1, 01K1], shows that the ordered moment at low temperature, $p_o$ = 0.15(3) $\mu_B$, is parallel to the crystallographic ***c***-axis. Relative nearest-neighbor spin alignment is ferromagnetic along the ***a***-axis and antiferromagnetic along the ***b*** and ***c***-axes, respectively. The (001) peak intensity which is the sum of nuclear and magnetic (proportional to the square of sublattice magnetization) peak intensities follows a power law $I(T) = I_o[(T_N - T)T_N^{-1}]^{2\beta}$+const with $T_N$ = 9.00(5) K and $\beta$ = 0.25(5) [01K1].

The magnetic data [80S1, 99T1, 00Y1] and neutron studies [99Y1] showed that $BaCu_2Si_2O_7$ should be considered as a quasi-1D system, dominated by strong intrachain antiferromagnetic exchange interactions. Long range ordering, at low temperatures, occurs owing to a much weaker interchain coupling. According to [01K1] the intrachain coupling is $J$ = 24.1 meV (280 K) in $BaCu_2Si_2O_7$. For $BaCu_2Ge_2O_7$ a BF analysis of the high-temperature part of the experimental $\chi(T)$ curve - Fig. 27a, yields $J/k_B \cong$ 540 K ($J$ = 46.5 meV) [99T1]. The AF exchange constant is nearly two times higher in $BaCu_2Ge_2O_7$ as compared to $BaCu_2Si_2O_7$. The AF spin chains in these two systems are formed by corner sharing $CuO_4$ plaquettes, and the main contribution to AF interactions is expected to be the superexchange mechanism involving the shared O sites. The $Cu^{2+}$ ions are not perfectly lined up, the Cu–O–Cu bond angle being smaller than 180° - Fig. 27d. The difference in $J$ is most likely due to the difference in bonding angle, 124° in $BaCu_2Si_2O_7$ and 135°in the Ge-based system [99T1]. A large bond angle is more favorable for superexchange involving oxygen.

An experimental study of the double gap, i.e. the separation between the magnon branch and the two-particle continuum, was performed by using cold neutrons [00Z1]. It was shown that the transverse excitation spectrum, in $BaCu_2Si_2O_7$, was divided into two well-defined regions. Below ~ 4 meV the weight is entirely consolidated into long-lived single particle excitations. These excitations carry only a small fraction of the total spectral weight at higher energies, where a continuum of states becomes the dominant contribution. The spin wave dispersion at the 1D AF zone $q_{\|} = \pi$ was measured along the [100] and [110] reciprocal-space directions, at $T$ = 1.5 K [01K1]. Most measurements were performed below 4.5 meV which, as above mentioned, is the threshold of the excitation continuum [00Z1]. Below this energy, the spectrum is expected to be dominated by single-particle spin-wave excitations. The corresponding dynamic structure factor and the spin-wave dispersion relation were analyzed by using the chain mean-field (chain-MF) approximation [97E1]. As mentioned above, a single nearest-neighbor Heisenberg exchange coupling constant, $J$, was sufficient to describe in-chain interactions. In order to reproduce the observed dispersion, in the perpendicular directions, three independent interchain exchange constants were required. The $Cu^{2+}$ chain in $BaCu_2Si_2O_7$ forms a rectangular lattice with nearest-neighbor Cu–Cu distances of $a/2$ and $b/2$ along ***a*** and ***b***-axes, respectively. The corresponding exchange constants were denoted by $J_x$ and $J_y$ - Fig. 27d. In addition, the exchange interaction $J_3$ along the [110] direction (third nearest-neighbor interchain Cu–Cu distance) was considered. The parameters $D_x$ and $D_y$, which are the anisotropy gaps for the two spin-wave branches, were included also in the dispersion relation. The in-chain exchange constant was fixed at $J$ = 24.1 meV and other parameters were refined. Values $J_x$ = −0.460(7) meV (ferromagnetic), $J_y$ = 0.200(6) meV, $2J_3$ = 0.152(7), $D_x$ = 0.36(2) meV and $D_y$= 0.21(1) meV were obtained. The gap induced in the quantum spin chains by the effective staggered exchange field in magnetically ordered state (which corresponds to the excitation energy at a point in the reciprocal space where interchain interactions cancel out at the RPA level) was $\Delta$ = 2.51 meV.

The temperature dependences of the magnetic susceptibilities for $BaCu_2(Si_{1-x}Ge_x)_2O_7$ polycrystalline samples are plotted in Fig. 27 a-c [01Y1]. As compared to $BaCu_2Si_2O_7$ the position of the broad maximum gradually shifts to higher temperature and height become lower with increasing x. By fitting the experimental data with a BF curve [64B1], the $J$ parameters were determined. These increase almost linearly when increasing the Ge content - Fig. 27a (inset). On the Si side, the kink at 8.9 K ($T_{N1}$) tends to fade away when increasing x, and instead another peak grows at lower temperature ($T_{N2}$), its position shifting to the lower temperatures as x increases. The two anomalies coexist in the samples with x = 0.025 and 0.05. The Curie-like divergence, which is already present in the Si compound, apparently increases with x. On the Ge side, the ferromagnetic contribution shifts to lower temperature and disappears for x < 0.9. There are neither AF or F anomalies for intermediate compositions of 0.25 ≤ x ≤ 0.75 above 2 K. According to [01Y1], $BaCu_2(Si_{1-x}Ge_x)_2O_7$ presents a

unique $S = 1/2$ 1D Heisenberg antiferromagnetic (HAF) system, comprising corner-sharing but corrugated CuO chains with strongly composition dependent intrachain AF interactions. A tentative magnetic phase diagram at low temperatures is given in Fig. 28. A long-range order (LRO) sets in at $T_{N1}$(Si) = 8.9 K for x = 0. As x increases, this transition tends to fade away and is replaced by another one with a lower $T_{N2}$(Si) which decreases to below 2 K at x = 0.25. $BaCu_2Ge_2O_7$ exhibits a weak ferromagnetism at $T_{N1}$(Ge) = 8.6 K. This transition is sensitive to the applied field and the Si substitution as well, disappearing for (x, $H$) = (0.95, 0 and 1.9T). Similarly to the case of the Si-rich side, a low-temperature transition appears at $T_{N2}$(Ge) ≅ 4 K and shows a peculiar field dependence. In [01Y1] a possible model was proposed to analyze the experimental data in the $BaCu_2(Si_{1-x}Ge_x)_2O_7$ system. The sensitivity of the transitions to magnetic field suggests that interchain interactions and $-\mu_o M_{chain} \cdot H$ are of comparable magnitude, leading to the broadening and/or the disappearance of the magnetic and thermal anomalies due to the LRO. The small interchain coupling changes with the composition from ferromagnetic, at the Si side, to antiferromagnetic at the Ge side. It was pointed out that the interchain coupling can be diminished near x = 0.75, were almost completely magnetically isolated chains would be expected.

#### 8.1.2.2.3 $^{57}$Fe nuclear gamma resonance (NGR) data

The melilite group of silicates was studied by the $^{57}$Fe NGR method [85A1, 86A1]. The $^{57}$Fe NGR spectrum of a $Ca_2MgSi_2O_7$–$NaCaFe^{3+}Si_2O_7$ sample consists of one doublet, identified to belong to $Fe^{3+}$ in T1 sites. The spectra of $Ca_2MgSi_2O_7$–$Ca_2Fe^{3+}AlSiO_7$, $Ca_2Al_2SiO_7$–$Ca_2Fe^{3+}AlSiO_7$ or $Sr_2Al_2SiO_7$–$Sr_2Fe^{3+}AlSiO_7$ systems consist of two doublets - Table 7 [85A1]. The inner and outer doublets were identified to belong to $Fe^{3+}$, in less distorted T1 and in more distorted T2 sites, respectively. The analysis of area ratios shows that the site occupancy of $Fe^{3+}$(T1) in gehlenite is less than that in åkermanite in which the distribution of $Fe^{3+}$ in T1 and T2 sites is apparently random. The different distributions were explained, as discussed in section 8.1.2.2.1, in terms of competition between minimizing the deficiency in the electrostatic valence and the preference of Al for T1 sites, which the isomer shift measurements show to be more ionic.

The quadrupole splitting was correlated with the angular distortion of the tetrahedra. The distortion was described in terms of $\sigma_{tet}$ parameter defined as $\sigma_{tet} = \sum_i (\theta_i - 109.47°)^2 / 5$ where $\theta_i$ is the O–T–O angle [71R1, 82K2, 84K1]. As mentioned above, the quadrupole splitting, $\Delta Q$, of $Fe^{3+}$ ions located in T1 sites are smaller than those in T2 sites. The variation of $\Delta Q$ values as function of $\sigma_{tet}$ is described by the empirical relation $\Delta Q$[mm/s] = 0.042 + 0.371$\sigma_{tet}$ – 0.016 $\sigma_{tet}^2$ ($0 < \sigma_{tet} < 8$) - Fig. 29. The above data seem to support the suggestion that $\Delta Q$ values of $Fe^{3+}$, in the tetrahedral sites, depend primarily on the angular distortion of the tetrahedra [81H2].

In the $0.50Ca_2Ga_2SiO_7$–$0.50Ca_2Fe^{3+}GaSiO_7$ silicate, the distribution of $Fe^{3+}$ and $Ga^{3+}$ in T1 and T2 sites, as determined by $^{57}$Fe NGR, is apparently random - Table 7 -, which can be explained in terms of the electrostatic valence rule [86A1]. However, in the melilites 0.52 $Ca_2MgSi_2O_7$–0.42 $Ca_2Fe^{3+}GaSiO_7$–0.06 $Ca_2Ga_2SiO_7$ and 0.62 $Ca_2MgSi_2O_7$–0.36 $Ca_2Fe^{3+}GaSiO_7$–0.02 $Ca_2Ga_2SiO_7$, $Fe^{3+}$ shows the preference for the more ionic T1 site and $Ga^{3+}$ for the more covalent T2 site - Table 7. If the electronegativity of $Ga^{3+}$ is assumed to be larger than that of $Fe^{3+}$, the mode of distribution of $Fe^{3+}$ and $Ga^{3+}$ can be explained in terms of the above mentioned hypothesis that a large electronegativity induces a stronger preference for the more covalent T2 site.

The $^{57}$Fe NGR spectra of synthetic $CaMg_{1-x}Fe_xSi_2O_7$ silicates with iron content $x \leq 0.8$ exhibit, at or below room temperature, two more or less clearly resolved doublets - Fig. 30 [87S1]. In as-prepared samples, ferric iron is absent or is very close to the limit of detection (< 0.01 atoms per formula unit). The two doublets were attributed to $Fe^{2+}$ situated in tetrahedral sites. The two sites become less distinguishable as temperature approaches the phase transition critical temperature and merge into one site in the normal structure. The temperature dependences of the isomer shifts, $\delta$, and quadrupole splittings, $\Delta Q$, for a sample with x = 0.3, are shown in Fig. 31 [87S1]. Both, $\delta$ and $\Delta Q$ values of the inner doublet show much less change with temperature than the outer doublet, until the two merge into each other.

The $^{57}$Fe NGR spectra of $Sr_2FeSi_2O_7$ and $Ba_2FeSi_2O_7$ melilites exhibit only one $Fe^{2+}$ doublet [74I1].

#### 8.1.2.2.4 Perturbed angular correlation (PAC)

**$Ba_2(Ti_{0.95}Hf_{0.05})(Ge_{2x}Si_{2-2x})O_8$**

The hafnium was introduced in $Ba_2(Ti_{0.95}Hf_{0.05})(Ge_{2x}Si_{2-2x})O_8$ fresnoites to provide PAC probe nuclei $^{181}Hf/^{181}Ta$ [89C1]. High-frequency, static nuclear electric quadrupole interactions, were observed in samples with x = 1.0 and 0.2 and chemical considerations indicated that these interactions occurred at the Ti sites. Because the electric field gradients associated with these interactions were produced primarily by the apical O atoms in $TiO_5$ tetragonal pyramids, neither the strength nor the symmetry of these interactions was very sensitive to the differences in the Ge–Si composition. These high-frequency interactions showed similar, non zero asymmetry parameters, $\eta$, at low temperatures and small-to-vanishing $\eta$ values at high temperatures. A phase change is supposed to occur between 500 K and 700 K - Fig. 32 [89C1]. Although the perturbation functions for samples with x = 1.0 and 0.2 differ in the character of the respective second interactions, they both show well defined, high frequency static interactions over the entire temperature range. The quadrupole frequencies, $\omega_Q$, show a slow decrease in magnitude with temperature and the $\omega_Q$ values, for the x = 0.2 sample, are higher by ~ 11 % than the x = 1.0 ones. The asymmetry parameters show a systematic decrease with temperature. The site populations, $f_1$, are relatively constant with average values 0.67 and 0.35 for x = 1.0 and x = 0.2 samples, respectively. Thus, approximately 2/3 of the probe sites for x = 1, and around 1/3 of the probe sites for x = 0.2 undergo this high-frequency interaction. The temperature dependence of the electric field gradient (EFG) at the Ti site was best described by a 3/2 power dependence. This result indicates that the vibrational motion of the quasi-one-dimensional Ti–O structure was not significantly anharmonic or anisotropic.

#### 8.1.2.2.5 Nuclear magnetic resonance (NMR) data

**Åkermanite, $Ca_2MgSi_2O_7$**

$^{29}Si$ MAS NMR studies were performed on $Ca_2MgSi_2O_7$ [83S2, 85J1, 89M1]. The $^{29}Si$ MAS NMR spectra, obtained in a variable temperature range, are shown in Fig. 33a [89M1]. The spectrum, at 290 K, consits of an intense band, at high frequency, which is not completely resolved from a number of aditional bands which stretch to low frequency. The $^{29}Si$ chemical shift, $\delta$, of the most intense band is –71.5 ppm. The remaining bands span the region to –73 ppm. The $^{29}Si$ chemical shifts fall within the limits expected for the $Si_2O_7$ dimer (i.e. $Q^1$ unit) [84M2]. The same values, $\delta$, were also obtained (–73.7 ppm) by [85J1], although the fine structure was not reported. Considering the remaining spectra, it may be seen that, with increasing temperature, there is a gradual decrease in width of the band. This is accompanied by an inward shift of intensity. Up to, and including the 370 K spectrum, a range of sites is present, as indicated by the partially resolved fine structure to low frequency. At 380 K the band has collapsed into a central resonance, but with shoulders still clearly present on both sides of the band. The shift of the central resonance of the high-temperature form (380 K and 385 K) is –72.0 ppm [89M1]. The $^{29}Si$ MAS NMR spectrum was decomposed in a number of Gaussian lines - Fig. 33b [89M1]. The result of the fitting of the variable temperature spectra are given in Fig. 33c. The intensity of each of the Gaussian band is shown in percentage. The figure emphasizes the continuous nature of the reduction of the number of different silicon environments. The incommensurate nature of the structure can produce a large number of Si sites. As temperature increases, the amplitude of the wave decreases and its wavelength increases until, at the phase transition, it disappears. Thus, it was concluded [89M1] that a manifold of sites exists at low temperatures, differing slightly in their Si–O–Si angles and/or Si–O bond lengths and that these sites become more similar with increasing temperature and merge into a single site at a phase transition, $T_{IC\text{-}N}$. The strongest structural changes occur at 371 K. The persistence of more than one Si position to some 385 K, as contrasted to $T_{IC\text{-}N}$ = 349(1) K obtained by calorimetric method, could be rationalized if it is assumed that long-range is lost at 349 K and that NMR data reflect only short-range order and do not seem responsible to long-range ordering effects [89M1].

**Gehlenite**

The chemical shifts, $\delta$, the chemical shift tensor components and the asymmetry parameters are listed in Table 8 [83S2].

**$Y_2Si_3O_3N_4$ (N-melilite)**

The $^{29}$Si MAS NMR study on $Y_2Si_3O_3N_4$ shows the presence of $SiO_2N_2(Q^3)$ and $SiO_2N_2(Q^4)$ environments. The isomer shift was –56.7 ppm (relative to tetramethylsilane) and full width at half height was 430 Hz [88D1, 89H1].

The $^{15}$N NMR measurements suggested that N atoms occupy the bridging site 2c and O atoms occupy the terminal site 4e, in the two $Si_2(O,N)_7$ units with Si at 4e, while the remaining two tetrahedra for Si at 2a in the unit cell, oxygen and nitrogen atoms (at 8f) are disordered but with an overall composition of three nitrogen and one oxygen in each tetrahedron ($SiON_3$) [96K1]. They proposed an O/N ordering at the 8f sites according to the intensity of the three peaks in the $^{15}$N spectra.

For EPR study of $Cr^{4+}$ in åkermanite see [93W1].

### 8.1.2.2.6 EXAFS data

The local structure around Co, Zn and Sr atoms in incommensurately modulated melilite-type $X_2T1Si_2O_7$ (X = Ca, Sr) and T1 = Mg, Co, Zn solid solutions have been investigated by EXAFS analyses [96T1]. The modulated structure was confirmed in $Ca_{2-x}Sr_xCoSi_2O_7$ solid solutions, with $0.0 \le x \le 0.6$ and for both $Ca_2Mg_{1-y}Co_ySi_2O_7$ and $Ca_2Mg_{1-y}Zn_ySi_2O_7$ solid solutions, over the whole compositional range, at room temperature.

The actual bond distances, determined by the EXAFS method for the T1 site (Co–O, Zn–O) in the modulated structure, are longer than the mean bond distance obtained from the X-ray diffraction method. This was attributed to the libration of the T1 tetrahedra [96T1]. In $Ca_{2-x}Sr_xCoSi_2O_7$ solid solutions, both the Sr–O and Co–O distances increase, from Ca end-member to Sr end-member. These increases are 0.8 % and 0.6 %, respectively. This means that the local expansions of the tetrahedral sheets and of the XO polyhedra are well matched. In the modulated $Ca_2Co_{1-y}Mg_ySi_2O_7$ and $Ca_2Zn_{1-y}Mg_ySi_2O_7$ solid solutions, the actual Co–O and Zn–O distances for T1 sites are nearly constant in the whole compositional range. The compositional variations of the local structure around the cations in the solid solutions are different for the X and T1 sites. It was concluded that the local geometrical restriction for the size of substitued cation in X site is larger than that in T1 site. The dimension of the tetrahedral sheet puts restriction on the size of cations situated at the interlayer X site. According to [96T1], different behaviour of the local geometric restriction between the X and T1 sites is an important feature of the melilite structure and is also related to the modulated structure.

### 8.1.2.2.7 Heat capacity

**$Ca_2Mg_{1-x}Co_xSi_2O_7$; $Ca_2Co_{1-x}Fe_xSi_2O_7$**

The temperature dependences of the specific heat around the phase transitions of $Ca_2Mg_{1-x}Co_xSi_2O_7$ and $Ca_2Co_{1-x}Fe_xSi_2O_7$ solid solutions are plotted in Fig. 34 [91I1]. At the IC-N transition point, the heat capacity anomalies show the λ-type characteristic behaviour, indicating a second order transition. In case of the $Ca_2Mg_{1-x}Co_xSi_2O_7$ system a little broadening peak is observed in the solid solutions, because of the composition variations, while the anomaly shape is very sharp for the end member. We note that the heat capacity of Mg-åkermanite shows λ-peaks at a temperature which depends on the density of dislocations and misfit dislocation at the twin boundary. In $Ca_2Mg_{1-x}Fe_xSi_2O_7$ [87S1] and $Ca_2Co_{1-x}Fe_xSi_2O_7$ [91I1], the λ anomalies in $C_p$ decrease with increasing Fe content while the transition temperature, $T_{IC\text{-}N}$, determined by electron microscopy observation, rises. This unusual behaviour is ascribed to the microdomains observed in high- resolution lattice images.

For the specific heat anomaly at the IC-N phase transition see also: $Ca_2MgSi_2O_7$ [86H1]; $(Ca_{1-x}Sr_x)_2CoSi_2O_7$ [91I1], $Ca_2Mg_{1-x}Zn_xSi_2O_7$ [91I1].

The entropy of gehlenite, $Ca_2Al_2SiO_7$ at 298.15 K and 1 kbar was reported to be 210.1(6) J/molK which includes a configurational contribution of 11.506 J/molK [84H1].

**$BaMn_2Si_2O_7$**

The zero-field specific heat of $BaMn_2Si_2O_7$ is shown in Fig. 35 [00L1]. The magnetic contribution to the specific heat was obtained by subtracting the lattice contribution. The broad maximum in the magnetic specific heat indicates that the entropy of the magnetic phase transition changes in a continuous fashion in the whole

temperature range. The maximum in the specific heat is shifted to lower temperatures as compared with that evidenced in magnetic susceptibilities. This suggests that at low temperatures the rising part of the susceptibility originates from further magnetic coupling. Thus, it is believed that the magnetic interactions consist of two stages. At high temperatures, predominant magnetic coupling occurs among the intrachain Mn ions. At low temperatures, long range order between the chains becomes more significant and, in this temperature range, the magnetic interactions become two-dimensional [00L1].

**$BaCu_2(Si_{1-x}Ge_x)_2O_7$**

The temperature dependences of the specific heat, $C/T$, are plotted in Fig. 36. In case of $BaCu_2Si_2O_7$ and $BaCu_2Ge_2O_7$ the peaks located at $T_{N1}$ = 8.9 K and 8.6 K, respectively, indicate the occurrence of magnetic order, the above values corresponding to critical temperatures. The peaks are small and broad suggesting that the transition is of second order [01Y1]. The small peaks, as well as the low Néel temperatures, imply that most of magnetic entropy is lost by short range ordering at high temperature below $J/k_B$. Under a field of 9T the peak in specific heat, for $BaCu_2Si_2O_7$, is pushed by 0.2 K to lower temperatures. In case of $BaCu_2Ge_2O_7$ the peak is broadened with increasing magnetic field and another peak grows at 3…4 K. The 9 K peak is completely replaced by one at 3.6 K for a field of 9 T. We note that a shoulder was already present around 3 K, at zero field. The initially weakly ferromagnetic state of $BaCu_2Ge_2O_7$ was replaced by another one at high magnetic field, while the antiferromagnetic order in $BaCu_2Si_2O_7$ is robust. This fact can be related to the nature of interchain coupling [01Y1] - see section 8.1.2.2.2.

Two peaks at 9 K and 5 K coexist for sample with x = 0.025 and a trace of the 9 K peak is discernible up to x = 0.15. The low-temperature peak shifts to lower temperatures as x increases, down to below 2 K for x = 0.25, for which a steep leading increase is visible near 2 K [01Y1]. On the Ge-rich side, the peak at 8.6 K, characteristic for x = 1, disappears completely for x = 0.95 and instead another peak is seen at 4 K, as on the Si-rich side. However, the low-temperature peak seems to appear only below 2 K even at x = 0.90. A nearly flat temperature dependence for $C/T$ was seen below 5 K for x = 0.75, suggesting that the specific heat $C/T$ contains a large linear term in $T^2$ - Fig. 36b (inset) - although a sudden jump follows below 2.4 K. In this case a value $\gamma \cong$ 23 mJ/K$^2$ mol Cu was obtained, which corresponds to $J/k_B \cong 240$ K. This value is about half of $J/k_B$ = 448 K estimated from magnetic data - Fig. 27a. The discrepancy was attributed to an overestimation of $\gamma$. A considerable amount of Schottky contribution to the specific heat must be involved in the $C/T$ data. This sample may be an almost ideal ½ Heisenberg AF chain system without any magnetic order above 2 K. According to [01Y1] it might be possible to realize perfect isolated 1D chains in a sample with certain composition near x = 0.75 were AF and F interchain interactions cancel each other.

### 8.1.2.2.8 Piezoelectric properties

**$Ba_2Si_2TiO_8$**

The fresnoite received attention for its pyroelectric, piezoelectric and surface acoustic properties [76K1, 77H1, 77K1, 78M1, 78Y1, 79Y1, 85M1, 97H1]. In addition, the possibility of making polar glass-ceramics by the recrystallization of a glass having $Ba_2TiSi_2O_8$ composition has been reported [81H1]. The fresnoite glass-ceramics show a sharp sign reversal in the pyroelectric coefficient at 433 K. This effect is also characteristic for single crystals. Other electrical properties (dielectric constant, frequency constant, electromechanical coupling) show anomalies at 433 K [85M1]. The temperature dependence of the pyroelectric coefficient of a $Ba_2TiSi_2O_8$ single crystal is plotted in Fig. 37 for $T > 123$ K. We note that the first sign reversal was evidenced at 93 K (not shown in figure). This was attributed to a secondary effect which gradually becomes smaller with decreasing temperature. A second sign reversal of the pyroelectric effect is shown at 433 K. High-temperature X-ray powder diffraction data, DTA and specific heat measurements gave no indication of a phase transition. To explain this effect, a model was developed that gave the pyroelectric coefficient in terms of changes in the atomic (primarily O atom) displacement with temperature [85M1]. The model, which used atomic displacement derived from X-ray diffraction, did not give a satisfactory explanation of the experimental data.

The main piezoelectric properties are listed in Table 9. The surface acoustic waves were calculated [78M1, 79Y1]. Favorable properties were measured for the $z$-cut $x$-propagating wave [78M1]. For $Ba_2TiGe_{2-x}Si_{2-2x}O_8$, the pyroelectric coefficient is positive and increases over the temperature range 298 K to 263 K [78S1].

**$Sr_2TiSi_2O_8$**

The silicate shows second harmonic generation effect, about eight times larger than that of KDP. The ultraviolet absorption edges of $Sr_2TiSi_2O_8$ is around 270 nm [00Y1].

### 8.1.2.2.9 Optical properties

**$(Ca_{2-x}Nd_x)Ga_{2+x}Si_{1-x}O_7$**

Because of interesting acoustic and nonlinear characteristics, due to the absence of an inversion center, silicates with melilite-type structure doped with luminescent ions such as $Nd^{3+}$ have been synthesised. The crystal structure, luminescence properties and stimulated emission of $(Ca_{2-x}Nd_x)Ga_{2+x}Si_{1-x}O_7$ have been studied [86K1]. Using conventional lamp-pumping technique, pulsed stimulated emission of the wavelengths of two channels ($^4F_{3/2} \rightarrow {}^4I_{11/2,13/2}$) was excited and investigated at low and room temperatures.

**Cr doped melilites**

The melilite-type compounds have been doped also with chromium ions [91A1, 91D1, 91G1, 92D1, 97S1]. There is no octahedral site in melilite-type structure. Thus, if melilite crystals were grown with addition of Cr ions, no suitable site is provided for $Cr^{3+}$ ions. Therefore, if the growth atmosphere is suitable controlled, Cr species such as $Cr^{4+}$ may selectively be doped into crystal, while preventing the presence of $Cr^{3+}$ ions. The reports published so far agreed in the point that the most probable optical center in melilites was a $Cr^{4+}$ ion, substituted in tetrahedral sites. The interest of melilite crystals as a laser host of $Cr^{4+}$ diminished because of their weak emission intensity.

The room temperature polarized absorption spectra of $Cr^{4+}$ doped åkermanite and Ga-gehlenite are shown in Fig. 38. Each of them exhibit a characteristic peak at around 590 nm when $\boldsymbol{E} \parallel \boldsymbol{c}$ and double natured peaks around 760 nm and 690 nm when $\boldsymbol{E} \perp \boldsymbol{c}$ [91A1, 91G1, 97S1]. Polarized photoluminescence spectra of melilite crystals, at room temperature, show luminescence peaks around 1200 nm…1300 nm. No luminescence was observed in the visible range. Besides $Cr^{4+}$, which is regarded as a major species in melilites, the existence of $Cr^{6+}$ in gehlenite was also suggested from the change in absorption spectra by annealing and the dependence of distribution coefficient of chromium ions on growth atmosphere [97S1]. The possibility of existence of $Cr^{3+}$ was ruled out because of a lack of luminescence in the visible range and the absence of a site of suitable size for $Cr^{3+}$ to substitute. In melilites, since only the tetrahedral sites are available, substitution of $Cr^{3+}$ was more difficult to take place than in the case of $Cr^{4+}$ or $Cr^{6+}$ even in $N_2$ atmosphere. For melilites, the absorption peaks are due to the $^3A_2 \rightarrow {}^3T_1$ transition and the photoluminescence peaks are ascribed to the $^3T_2 \rightarrow {}^3A_2$ transition of the $3d^2$ system in a tetrahedral field. The temperature dependence of the lifetime and integrated intensity indicated that for $Cr^{4+}$ not only non-radiative transition probability, but also radiative probability is temperature dependent, which is different from $Cr^{3+}$. Spectral peak shifts are not obvious if the host crystal field is altered in melilites, because the local environment of the sites for Cr ions is possibly changed by reforming the packing feature of the host lattice.

**$Ca_2Al_2SiO_7$, $Ca_2MgSi_2O_7$, $CaNaAlSi_2O_7$**

The prominent features of the Raman spectrum of $Ca_2Al_2SiO_7$ are strong and polarized bands at 84 and 552 $cm^{-1}$ and a very strong and polarized band at 896 $cm^{-1}$. In addition, weak bands appear at ~ 371 $cm^{-1}$ in the $I_\perp$ spectrum and two weak and polarized shoulders at ~ 662 and 1004 $cm^{-1}$ - Fig. 39 [83S1]. The $\nu_3$(T-O-T) band appears at lower frequency (552 $cm^{-1}$) in glass than that of crystalline phase (626 $cm^{-1}$), and the intensity of the band in the 900…1200 $cm^{-1}$ range in the glass spectrum is much stronger than the intensities of the corresponding bands in the spectrum of crystalline gehlenite. The shift of the band to lower frequency in the spectrum of the glass indicated that most of the $Al^{3+}$ ions are tetrahedrally coordinated and act as network formers. The strong band at approximately ~ 896 $cm^{-1}$ in the spectrum of gehlenite glass, was attributed to the presence of an appreciable amount of $SiO_4^{4-}$ groups in the glass network. The structure of glass having gehlenite composition is thus highly polymerized, with $CaAl_2O_4$ present in the network. The 0.33 nonbridging oxygens per

network-forming cation (Si-Al), as required by the stoichiometry of the glass to charge-balance the $Ca^{2+}$ ion, exist in the form of $SiO_4^{4-}$ groups in the glass network.

The Raman spectra of $Ca_2MgSiO_7$ and $NaCaAlSi_2O_7$ were reported by [79S1, 83S1]. The IR spectra of the above silicates, as well as of $Ca_2Al_2Si_2O_7$, were also analysed by [87S1]. In [87D1], normal coordinate calculations producing synthetic IR and Raman spectra were carried out on melilites. The symmetric T-Onb stretching vibrations of Si and Al tetrahedra, with different numbers of bridging oxygens, were separated from each other, but may combine individually with oscillations of bridging oxygens between Si and Al tetrahedra. The latter type of vibrations tends to dominate as Al/Si ratio increases. The frequencies of these vibrational components and the degree of such intermixing depend on T–O force constants, which vary greatly, depending on local bonding configurations; individual bands in the high-frequency Raman spectra cannot, in general, be assigned to single structural entities or fixed combinations thereof.

Polarized optical absorption spectra of natural gehlenite, in which $Fe^{2+}$ substitutes for Al in a tetrahedral site, are plotted in Fig. 40 [01R1]]. There are multiple bands. Two bands with maxima around 4970 $cm^{-1}$ (2012 nm, $\boldsymbol{E} \perp \boldsymbol{c}$) and 6250 $cm^{-1}$ (1600 nm, $\boldsymbol{E} \parallel \boldsymbol{c} > \boldsymbol{E} \perp \boldsymbol{c}$) were assigned to components of the $^5E \rightarrow {}^5T_2$ transition of $^{[4]}Fe^{2+}$. A band near 9220 $cm^{-1}$ (1085 nm, $\boldsymbol{E} \perp \boldsymbol{c}$) seen in spectrum, as a shoulder on the high- energy side of the 1600 nm band, is at too high an energy to be attributed to d-d transitions of tetrahedral $Fe^{2+}$ and at too low an energy to be caused by $Fe^{2+}/Fe^{3+}$ intervalence charge transfer transition. Another cation site in the gehlenite structure that can accommodate some amount of $Fe^{2+}$ is the Ca-bearing polyhedron. According to [01R1] it is quite possible that the shoulder is caused by spin allowed dd transitions in $^{Ca}Fe^{2+}$. The band assignments at about 2800…3000 nm (3570…3330 $cm^{-1}$) are difficult. The band at 2800 nm, is in a region appropriate for OH (probably in small amounts). The possibility to be assigned also to $Fe^{2+}$ complicated the analysis. The splitting of the $^5T_2$ level of $^{[4]}Fe^{2+}$ into two components, 4970 $cm^{-1}$ ($\boldsymbol{E} \perp \boldsymbol{c}$) and 6250 $cm^{-1}$ ($\boldsymbol{E} \parallel \boldsymbol{c} > \boldsymbol{E} \perp \boldsymbol{c}$) is consistent with a comparatively high symmetry of the tetrahedral site that keeps all Fe–O distances equal [01R1].

In [94I1] was investigated the origin of the circular diffuse scattering which appears when åkermanite is in a transitional state between the incommensurate and either the normal and commensurate phase, by exchanging the Ca atom for larger alkali- earth atoms, such as Sr, or by exchanging Mg atoms for larger atoms such as Fe and/or increasing the temperature, by using an optical diffraction method. Under this transitional state, the structure consists of many layers, whose modulation waves repeat with a layer-to-layer phase difference and with constant phase differences within each layer. When the incommensurate phase transforms to normal phase, the wavelength increases and decreases, respectively, when it transforms to the commensurate phase.

### $Ba_2VOSi_2O_7$, $Ba_{1.5}VOSi_2O_7$

The diffuse reflectance spectra of $Ba_2VOSi_2O_7$ and $Ba_{1.5}VOSi_2O_7$ - Fig. 41 - are consistent with the presence of $V^{4+}$ and $V^{5+}$ oxidation states, respectively [01R2]. $Ba_2VOSi_2O_7$ shows three characteristic absorption bands at 470, 620 and > 800 nm, which are due to short vanadyl $[V = O]^{2+}$. $Ba_{1.5}VOSi_2O_7$ does not show these absorptions; instead it shows an absorption edge at ~ 455 nm, which is likely due to $V^{5+} \leftarrow$ O charge transfer. The second harmonic generation (SHG) response of both $Ba_2VOSi_2O_7$ and $Ba_{1.5}VOSi_2O_7$ was measured to the 1064 nm Nd: YAG laser radiation. While $Ba_2VOSi_2O_7$ shows a weak response (~ 10 times that of α-quartz), $Ba_{1.5}VOSi_2O_7$ gives a much stronger response (~ 200 times that of α-quartz) almost comparable to that of $K_2(NbO)_2Si_4O_{12}$ [99G1].

### $Ba_2Ti_{1+x}Si_{2-x}O_8$ ($0 \leq x \leq 0.14$)

If was shown [61T1] that tetrahedrally coordinated Ti, $[TiO_4]$, has a characteristic vibration between 720 and 740 $cm^{-1}$, while $[TiO_6]$ octahedra absorb at 500…600 $cm^{-1}$. Comparing the IR spectra for x = 0 and x = 0.2 - Fig. 42 - shows the appearance of a prominent band at 740 $cm^{-1}$ for the sample with x = 0.2 that is absent for x = 0 [96C1]. This suggests the presence of tetrahedrally coordination $Ti^{4+}$ in the x = 0.2 sample.

### Jeffreyite

The jeffreyite crystal is biaxial negative. The refractive indices are $n_\alpha = 1.625(2)$; $n_\beta = 1.641(2)$; $n_\gamma = 1.643(2)$ and $2V_x(\text{meas}) = 40(2)^o$, $2V_x(\text{calc}) = 39^o$ [84G1].

For Raman spectra see also: melilites [81S1]; åkermanite, sodium melilite glasses [79S1].

## Tables and figures

**Table 1.** Melilites and related silicates[1)] [91N1, 99M1].

| Silicate | Composition | Group |
|---|---|---|
| Åkermanite | $Ca_2MgSi_2O_7$ | VIIIB02a |
| Hardystonite | $Ca_2ZnSi_2O_7$ | VIIIB02a |
| Gugiaite | $Ca_2BeSi_2O_7$ | VIIIB02a |
| Gehlenite | $Ca_2Al(Si,Al)_2O_7$ | VIIIB02a |
| Melilite | $(Ca,Na)_2(Al,Mg)(Si,Al)_2O_7$ | VIIIB02a |
| Okayamalite | $Ca_2SiB_2O_7$ | |
| Fresnoite | $Ba_2TiO(Si_2O_7)$ | VIIIB02a |
| Chkalovite | $Na_2BeSi_2O_6$ | VIIIB02b |
| Jeffreyite | $(Ca,Na)_2(Be,Al)Si_2(O,OH)_7$ | VIIIB02b |
| Lovdarite | $K_2Na_6Be_4Si_{14}O_{36}\cdot 9H_2O$ | VIIIB02b |
| Nordite-(Ce) | $Na_3(Sr,Ca)(Ce,La)(Zn,Mg)Si_6O_{17}$ | VIIIB02b |
| Nordite-(La) | $Na_3(Sr,Ca)(La,Ce)(Zn,Mg)Si_6O_{17}$ | VIIIB02b |
| Leucophane | $NaCaBeSi_2O_6F$ | VIIIB02b |
| Meliphanite | $Ca(Na,Ca)BeSi_2O_6F$ | VIIIB02b |

[1)] in addition to these minerals, the magnetic and related properties of other synthetic silicates with related structures will be reviewed. ($BaM_2Si_2O_7$ and $Ba_2MSi_2O_7$ with M = Be, Mg, Mn, Co, Cu, Zn; $KHoCoSi_2O_7$; $Na_2Mn_2Si_2O_7$; $Na_2Si_3O_7$; $Li_6Si_2O_7$; $Li_2Si_3O_7$; $Y_2SiBe_2O_7$; $R_2Si_3O_3N_4$ where R is Y or a rare-earth).

**Table 2.** Coordinates and thermal vibration parameters.

a) Melilite, $CaAlNaSi_2O_7$ – space group $P\bar{4}2_1m$ [70L1].

| Atom | *x* | *y* | *z* | $\beta_{ij}\cdot 10^4$ | | | | | | Site occupancy | |
|---|---|---|---|---|---|---|---|---|---|---|---|
| | | | | $\beta_{11}$ | $\beta_{22}$ | $\beta_{33}$ | $\beta_{12}$ | $\beta_{13}$ | $\beta_{23}$ | ideal | observed |
| $(Ca_{1/2}Na_{1/2})$ | 0.3399(2) | 1/2-*x* | 0.5134(3) | 50(2) | $\beta_{11}$ | 71(5) | 15(3) | 9(2) | $-\beta_{13}$ | 0.50 | 0.4976(27) |
| Al | 0 | 0 | 0 | 18 [1)] | $\beta_{11}$ | 47(7) | 0 | 0 | 0 | 0.25 | 0.2448(21) |
| Si | 0.1416(2) | 1/2-*x* | 0.9531(3) | 9(2) | $\beta_{11}$ | 10(4) | –3(2) | –2(2) | $-\beta_{13}$ | 0.50 | 0.4554(31) |
| O1 | 1/2 | 0 | 0.1687(12) | 34(6) | $\beta_{11}$ | 34(16) | –23(9) | 0 | 0 | 0.25 | nv[2)] |
| O2 | 0.1428(6) | 1/2-*x* | 0.2652(9) | 74(6) | $\beta_{11}$ | 75(12) | 7(10) | –12(7) | $-\beta_{13}$ | 0.50 | nv[2)] |
| O3 | 0.0852(4) | 0.1747(5) | 0.8120(6) | 45(6) | 35(6) | 59(8) | –13(5) | 13(6) | 10(6) | 1.00 | nv[2)] |

b) Åkermanite, $Sr_2MgSi_2O_7$ – space group $P\bar{4}2_1m$ [83K1].

| Atom | Site | *x* | *y* | *z* | $\beta_{ij}\cdot 10^4$ | | | | | | Site occupancy |
|---|---|---|---|---|---|---|---|---|---|---|---|
| | | | | | $\beta_{11}$ | $\beta_{22}$ | $\beta_{33}$ | $\beta_{12}$ | $\beta_{13}$ | $\beta_{23}$ | ideal |
| Sr | 4e | 0.3345(5) | 1/2-*x* | 0.5077(1) | 265(4) | $\beta_{11}$ | 564(15) | 60(6) | 58(9) | $-\beta_{13}$ | 1/2 |
| Mg | 2a | 0 | 0 | 0 | 145(41) | $\beta_{11}$ | 324(84) | 0 | 0 | 0 | 1/4 |
| Si | 4e | 0.1387(2) | 1/2-*x* | 0.9438(4) | 88(14) | $\beta_{11}$ | 256(49) | 59(17) | –58(18) | $-\beta_{13}$ | 1/2 |
| O1 | 2c | 0.5 | 0 | 0.1603(5) | 199(113) | $\beta_{11}$ | 479(213) | –93(78) | 0 | 0 | 1/4 |
| O2 | 4e | 0.1396(6) | 1/2-*x* | 0.2528(10) | 322(52) | $\beta_{11}$ | 340(142) | –87(61) | –34(63) | $-\beta_{13}$ | 1/2 |
| O3 | 8f | 0.0793(5) | 0.1915(5) | 0.8034(7) | 304(53) | 110(49) | 526(101) | –10(36) | 25(36) | –30(59) | 1 |

**Table 2** (continued)

c) Gehlenite, $Sr_2Al_2SiO_7$ – space group $P\bar{4}2_1m$ [84K1].

| Atom | Site | $x$ | $y$ | $z$ | $\beta_{ij} \cdot 10^4$ | | | | | | Site occupancy |
|---|---|---|---|---|---|---|---|---|---|---|---|
| | | | | | $\beta_{11}$ | $\beta_{22}$ | $\beta_{33}$ | $\beta_{12}$ | $\beta_{13}$ | $\beta_{23}$ | ideal |
| Sr | 4e | 0.3382(1) | 1/2-$x$ | 0.5094(2) | 37(11) | $\beta_{11}$ | 65(2) | 16(1) | 3(2) | $-\beta_{13}$ | 1/2 |
| T1 | 2a | 0 | 0 | 0 | 17(6) | $\beta_{11}$ | 55(10) | 0 | 0 | 0 | 1/4 |
| T2 | 4e | 0.1413(2) | 1/2-$x$ | 0.9620(5) | 6(2) | $\beta_{11}$ | 21(7) | 5(3) | 0 | $-\beta_{13}$ | 1/2 |
| O1 | 2c | 0.5 | 0 | 0.1602(19) | 30(18) | $\beta_{11}$ | 55(30) | 16(13) | 0 | 0 | 1/4 |
| O2 | 4e | 0.1419(8) | 1/2-$x$ | 0.2735(13) | 30(7) | $\beta_{11}$ | 79(20) | –5(10) | –6(10) | $-\beta_{13}$ | 1/2 |
| O3 | 8f | 0.0839(7) | 0.1711(7) | 0.8221(9) | 44(9) | 22(8) | 61(13) | –3(8) | 17(10) | –8(1) | 1 |

d) Fresnoite, $Ba_2TiSi_2O_8$, having tetragonal structure, space group P4bm, at room temperature [85M1].

| Site | $x$ | $y$ | $z$ | $B_{eq}$ [Å$^2$][3)] |
|---|---|---|---|---|
| Ba | 0.32701(3) | 0.82701(3) | 0.0 | 0.99(1) |
| Ti | 0.0 | 0.0 | –0.5354(3) | 0.70(4) |
| Si | 0.1280(2) | 0.6280(2) | –0.5129(8) | 0.70(3) |
| O1 | 0.0 | 0.5 | –0.6293(19) | 1.44(16) |
| O2 | 0.1259(5) | 0.6259(5) | –0.2051(12) | 1.01(11) |
| O3 | 0.2924(6) | 0.5772(8) | –0.6429(1) | 1.84(13) |
| O4 | 0.0 | 0.0 | –0.2096(20) | 1.82(18) |

e) Nordite – space group Pcca [70B1].

| Atom | $x$ | $y$ | $z$ | $B$ [Å$^2$][3)] |
|---|---|---|---|---|
| R | 0.2500 | 0 | 0.3194 | 0.39(3) |
| (Sr,Ca) | 0.2500 | 0 | 0.0217(2) | 0.06(5) |
| $M^{2+}$ | 0.2500 | 0.5000 | 0.1687(3) | 0.91(7) |
| Si1 | 0.0980(7) | 0.4542(23) | 0.0623(4) | 0.61(14) |
| Si2 | 0.1019(7) | 0.5433(23) | 0.2747(4) | 0.46(13) |
| Si3 | 0.1116(5) | 0.5516(7) | –0.0819(4) | 0.31(11) |
| (Na,Mn) | 0 | 0 | 0 | 2.05(36) |
| Na | 0.0696(10) | 0.0125(81) | 0.1693(8) | 2.10(26) |
| O1 | 0.9955(16) | 0.3389(53) | 0.0811(14) | 0.84(10) |
| O2 | 0.1701(18) | 0.2995(71) | 0.1101(12) | 0.70(10) |
| O3 | 0.1172(18) | 0.3537(59) | –0.0131(12) | 1.49(46) |
| O4 | 0.1019(6) | 0.7640(68) | 0.0672(12) | 1.64(45) |
| O5 | 0 | 0.6366(96) | 0.2500 | 1.28(58) |
| O6 | 0.1783(18) | 0.7090(69) | 0.2321(12) | 0.83(33) |
| O7 | 0.1221(19) | 0.6503(58) | 0.3532(13) | 1.00(77) |
| O8 | 0.1178(18) | 0.2392(58) | 0.2714(12) | 1.26(40) |
| O9 | 0.1857(15) | 0.2226(58) | 0.4173(14) | 1.11(33) |

**Table 2** (continued)

f) Leucophane, $CaNaBeSi_2O_6F$ – space group $P2_12_12_1$ [67C1].

| Atom | *x* | *y* | *z* | $B_{eq}$·[Å$^2$][3)] |
|---|---|---|---|---|
| Ca | 0.1050(4) | 0.8265(5) | 0.9894(3) | 1.23 |
| Na | 0.0670(11) | 0.8535(13) | 0.5059(8) | 2.33 |
| Si1 | 0.7406(5) | 0.0132(7) | 0.2507(4) | 0.85 |
| Si2 | 0.1080(5) | 0.1508(7) | 0.2265(4) | 0.71 |
| Be | 0.1091(24) | 0.1268(50) | 0.7174(32) | 1.84 |
| O1 | 0.2421(20) | 0.0037(23) | 0.1623(14) | 1.38 |
| O2 | 0.1052(20) | 0.1607(29) | 0.3829(22) | 1.46 |
| O3 | 0.8382(12) | 0.8484(21) | 0.3381(12) | 1.28 |
| O4 | 0.8383(14) | 0.8308(20) | 0.8476(12) | 1.33 |
| O5 | 0.9130(14) | 0.0746(19) | 0.6574(10) | 1.46 |
| O6 | 0.9087(17) | 0.1000(18) | 0.1627(13) | 1.35 |
| F | 0.1021(13) | 0.1315(17) | 0.8753(9) | 1.66 |

g) N-Melilite, $Y_2Si_3O_3N_4$ – space group $P\bar{4}2_1m$ [97W1][4)].

| Atom | Site | *x* | *y* | *z* |
|---|---|---|---|---|
| Y | 4e | 0.3363 | 0.1637 | 0.5028 |
| Si1 | 2a | 0.0 | 0.0 | 0.0 |
| Si2 | 4e | 0.1442 | 0.3558 | 0.9407 |
| O1 | 2c | 0.5 | 0.0 | 0.1942 |
| O2 | 4e | 0.1435 | 0.3565 | 0.2827 |
| N | 8f | 0.0926 | 0.1623 | 0.7948 |

h) $BaCu_2Si_2O_7$ – space group Pnma [01Y1].

| Atom | Site | *x* | *y* | *z* | $B_{eq}$ [Å$^2$] |
|---|---|---|---|---|---|
| Ba | 4c | –0.0115(3) | 0.25 | 0.9558(2) | 1.77(4) |
| Ca | 8d | 0.2214(3) | 0.0052(2) | 0.7927(3) | 1.80(6) |
| Si | 8d | 0.0045(9) | 0.1337(2) | 0.4732(6) | 0.66(8) |
| O1 | 4c | 0.0775(13) | 0.25 | 0.4781(14) | –0.01(30) |
| O2 | 8d | –0.1617(13) | 0.1311(8) | 0.6238(12) | 1.97(25) |
| O3 | 8d | –0.0698(13) | 0.1155(8) | 0.2619(10) | 2.33(30) |
| O4 | 8d | 0.1809(9) | 0.0649(5) | 0.5299(12) | 0.58(22) |

[1)] since different scales were used for the different k layers, $\beta_{11}$ of Al was not varied;
[2)] was not varied as a least-square parameter;
[3)] isotropic temperature factor;
[4)] model I (see text).

**Table 3.** Crystal structures and lattice parameters.

| Silicate | $T$ [K] | Space group | Lattice parameters | | | | Refs. |
|---|---|---|---|---|---|---|---|
| | | | $a$ [Å] | $b$ [Å] | $c$ [Å] | $\beta$ | |
| Åkermanite[1)] | RT | $P\bar{4}2_1m$ | 7.835(1) | | 5.010(1) | | 81K1, 83K1 |
| $Ca_2MgSi_2O_7$ | RT | $P\bar{4}2_1m$ | 7.8348(4) | | 5.0087(3) | | 01K2 |
| Åkermanite[2)] | RT | $P\bar{4}2_1m$ | 7.8332(6) | | 5.0070(6) | | 90L1 |
| Sr-åkermanite[3)] | RT | $P\bar{4}2_1m$ | 7.9957(10) | | 5.1521(9) | | 83K1 |
| $(Sr_{0.75}Ca_{0.25})_2MgSi_2O_7$ | RT | $P\bar{4}2_1m$ | 7.970(1) | | 5.122(1) | | 83K1 |
| $(Sr_{0.50}Ca_{0.50})_2MgSi_2O_7$ | RT | $P\bar{4}2_1m$ | 7.933(1) | | 5.083(1) | | 83K1 |
| $(Sr_{0.25}Ca_{0.75})_2MgSi_2O_7$ | RT | $P\bar{4}2_1m$ | 7.887(1) | | 5.045(1) | | 83K1 |
| $Ca_2CoSi_2O_7$ | RT | $P\bar{4}2_1m$ | 7.8436(4) | | 5.0256(3) | | 90I1 |
| $Ca_2CoSi_2O_7$ | RT | $P\bar{4}2_1m$ | 7.8417(6) | | 5.0249(3) | | 93H1, 94I1 |
| $Ca_2CoSi_2O_7$ | 170 | $P2_12_12$ | 23.510(4) | 23.510(4) | 5.025(1) | | 01H1 |
| $Ca_2ZnSi_2O_7$ | RT | $P\bar{4}2_1m$ | 7.83 | | 4.99 | | 30W2 |
| $Ca_2ZnSi_2O_7$ | RT | $P\bar{4}2_1m$ | 7.75(5) | | 5.01 | | 54S1 |
| $Ca_2ZnSi_2O_7$ | RT | $P\bar{4}2_1m$ | 7.8240(4) | | 5.0159(5) | | 02B1 |
| $Ca_2ZnSi_{0.75}Ge_{1.25}O_7$ | RT | $P2_1/n$ | 9.112(1) | 7.900(2) | 9.380(1) | 114.03(1)° | 90A1 |
| Hardystonite[4)] | RT | $P\bar{4}2_1m$ | 7.8287(16) | | 5.0140(4) | | 69L1 |
| Hardystonite[4)] | RT | $P\bar{4}2_1m$ | 7.8279(10) | | 5.0138(6) | | 69L1 |
| Hardystonite[5)] | RT | $P\bar{4}2_1m$ | 7.800(1) | | 5.000(1) | | 01B1 |
| $Ca_2(Mg_{0.55}Fe_{0.45})Si_2O_7$ | RT | $P\bar{4}2_1m$ | 7.8679(3) | | 5.0144(2) | | 98K1 |
| $Ca_2BeSi_2O_7$ | RT | $P\bar{4}2_1m$ | 7.48 | | 5.04 | | 62P1 |
| $Ca_2BeSi_2O_7$ | RT | $P\bar{4}2_1m$ | 7.501 | | 4.981 | | 53G1 |
| $Ca_2BeSi_2O_7$ | RT | $P\bar{4}2_1m$ | 7.419(1) | | 4.988(1) | | 82K3 |
| $Ca_2Al_2SiO_7$ | RT | $P\bar{4}2_1m$ | 7.688 | | 5.065 | | 89S1 |
| $Ca_2Al_2SiO_7$ | RT | $P\bar{4}2_1m$ | 7.6770(3) | | 5.0594(3) | | 82K2 |
| $Sr_2CoSiO_7$ | RT | $P\bar{4}2_1m$ | 8.0294(9) | | 5.1639(3) | | 90I1 |
| $Sr_2Al_2SiO_7$ | RT | $P\bar{4}2_1m$ | 7.820(1) | | 5.264(1) | | 84K1 |
| $Sr_2Al_2SiO_7$ | RT | $P\bar{4}2_1m$ | 7.82 | | 5.27 | | 60B1 |
| $(Sr_{0.13}Ca_{0.87})_2CoSi_2O_7$ | RT | | 7.8743(4) | | 5.0417(2) | | 00B1 |
| $Ca_2Ga_2SiO_7$ | RT | $P\bar{4}2_1m$ | 7.793(3) | | 5.132(2) | | 86K1 |
| $Ca_2SiB_2O_7$ (okayamalite) | RT | $P\bar{4}2_1m$ | 7.1248(2) | | 4.8177(2) | | 00G1 |
| $CaNaAlSi_2O_7$ | RT | $P\bar{4}2_1m$ | 7.6344(6) | | 5.0513(6) | | 70L1 |
| Melilite[6)] | RT | $P\bar{4}2_1m$ | 7.803(1) | | 5.058(1) | | 85A1 |
| Melilite[7)] | RT | $P\bar{4}2_1m$ | 7.816(1) | | 5.039(1) | | 85A1 |
| Melilite[8)] | RT | $P\bar{4}2_1m$ | 7.728(3) | | 5.084(4) | | 85A1 |
| Melilite[9)] | RT | $P\bar{4}2_1m$ | 7.828(1) | | 5.068(1) | | 86A1 |
| Melilite[10)] | RT | $P\bar{4}2_1m$ | 7.829(1) | | 5.056(1) | | 86A1 |

**Table 3** (continued)

| Silicate | $T$ [K] | Space group | Lattice parameters | | | | Refs. |
|---|---|---|---|---|---|---|---|
| | | | $a$ [Å] | $b$ [Å] | $c$ [Å] | $\beta$ | |
| Melilite[11)] | RT | $P\bar{4}2_1m$ | 7.813(3) | | 5.134(2) | | 86A1 |
| Melilite[12)] | RT | $P\bar{4}2_1m$ | 7.805(4) | | 5.014(2) | | 85A1 |
| Sr-melilite[13)] | RT | $P\bar{4}2_1m$ | 7.875(4) | | 5. 273(4) | | 85A1 |
| Fresnoite[14)] | RT | $P\bar{4}2_1m$ | 8.52(1) | | 5.210(1) | | 65A1 |
| Fresnoite[15)] | RT | P4bm | 8.518(2) | | 5.211(1) | | 69M1 |
| $Ba_2TiSi_2O_8$ | RT | P4bm | 8.55 | | 5.22 | | 76K1 |
| $Ba_2TiSi_2O_8$ | 297 | P4bm | 8.527(1) | | 5.2104(9) | | 85M1 |
| | 473 | P4bm | 8.542(1) | | 5.219(1) | | 85M1 |
| | 773 | P4bm | 8.550(2) | | 5.235(2) | | 85M1 |
| $Sr_2TiSi_2O_8$ | RT | | 8.3135 | | 5.0190 | | 00Y1 |
| Jeffreyite[16)] | RT | $C222_1$ | 14.90(1) | 14.90(1) | 40.41(8) | | 84G1 |
| Lovdarite[17)] | RT | $P2_1$ | 78.88 | 6.91 | 7.15 | | 75K1 |
| Lovdarite | RT | Pma2 | 39.58 | 6.93 | 7.15 | | 81M2 |
| Nordite[18)] | RT | Pcca | 14.27(3) | 5.16(1) | 19.45(15) | | 70B1 |
| Leucophane[19)] | RT | $P2_12_12_1$ | 7.401(8) | 7.420(8) | 9.939(5) | | 67C1 |
| Leucophane[20)] | RT | $P2_12_12_1$ | 7.401(2) | 7.412(2) | 9.990(2) | | 89G1 |
| Leucophane[21)] | RT | P1 | 7.417(4) | 7.398(4) | 9.984(4) | | 92C1 |
| Meliphanite[22)] | RT | $I\bar{4}$ | 10.516(2) | | 9.887(2) | | 67D1 |
| $Na_2Mn_2Si_2O_7$ | RT | $P2_1/n$ | 8.757(3) | 13.294(6) | 5.744(2) | 90°10(2)' | 69A1, 82O1 |
| $BaZn_2Si_2O_7$ | RT | C2/c | 7.2782(4) | 12.8009(7) | 13.6869(7) | 90.093(6)° | 99L2 |
| $BaZn_2Si_2O_7$ | 553 | $Ccm2_1$ | 7.6199(4) | 13.0265(6) | 6.7374(2) | | 99L2 |
| $Ba_2CuSi_2O_7$ | RT | A2/a | 8.461(2) | 8.437(3) | 10.712(2) | 111.12(2)° | 84M1 |
| $BaMn_2Si_2O_7$ | RT | C2/c | 7.2953(3) | 12.9632(5) | 14.0321(5) | 90.248(2)° | 00L1 |
| $BaCo_2Si_2O_7$ | RT | C2/c | 7.2131(6) | 12.781(1) | 13.762(1) | 90.299(8)° | 93A1 |
| $BaCu_2Si_2O_7$ | RT | Pnma | 6.862(2) | 13.178(1) | 6.897(1) | | 01K1 |
| $BaCu_2Si_2O_7$ | RT | Pnma | 6.866 | 13.190 | 6.906 | | 90J1 |
| $BaCu_2Si_2O_7$ | RT | Pnma | 6.86058(8) | 13.17507(17) | 6.89589(8) | | 01Y1 |
| $BaCu_2Ge_2O_7$ | RT | Pnma | 7.04765(6) | 13.40700(9) | 7.02755(5) | | 01Y1 |
| $Ba_2VOSi_2O_7$ | RT | P4bm | 8.495(2) | | 5.215(2) | | 01R2 |
| $Ba_{1.5}VOSi_2O_7$ | RT | P4bm | 8.424(3) | | 5.198(2) | | 01R2 |
| $Ba_3NaSi_2O_7$ | RT | $P6_3/mmc$, $P6_3mc$ or $P\bar{6}2c$ | 5.791(4) | | 14.748(8) | | 71F1 |
| $Na_3YSi_2O_7$ | RT | $P6_3/m$ | 9.422(1) | | 13.790(2) | | 81M1 |
| $Na_3LuSi_2O_7$ | RT | $P6_3/m$ | 9.385(1) | | 13.716(2) | | 88T1 |
| $Na_3ScSi_2O_7$ | RT | Pbnm | 5.354(3) | 9.347(4) | 13.089(4) | | 69S1 |
| $Na_3AlBeSi_2O_8$ | RT | $P2_12_12_1$ | 7.18 | 6.82 | 7.48 | | 74H1 |
| $Na_2Si_3O_7$[23)] | RT | C2/c | 8.922(2) | 4.8490(5) | 11.567(1) | 102.64(1)° | 95F1 |
| $Na_2Si_3O_7$[24)] | RT | $P2_1c$ | 7.1924(5) | 10.6039(8) | 9.8049(7) | 120.2478(4)° | 02K1 |
| $Na_2Si_3O_7 \cdot H_2O$ | RT | | 7.3087 | 12.7246 | 9.0913 | 119.01° | 00M2 |
| $Na_2Cu_2Si_2O_7$ | RT | I2/a | 10.4906(5) | 10.3762(6) | 24.5349(12) | 91.217° | 02K1 |
| $NaBaNdSi_2O_7$ | RT | $P2_12_12_1$ | 9.3274(9) | 10.497(2) | 14.95(2) | | 83B1 |
| $KHoCoSi_2O_7$ | RT | P2, Pm or P2/m | 8.491(2) | 10.755(4) | 8.488(3) | 111.35(2)° | 80R1 |

**Table 3** (continued)

| Silicate | *T* [K] | Space group | Lattice parameters | | | | Refs. |
|---|---|---|---|---|---|---|---|
| | | | *a* [Å] | *b* [Å] | *c* [Å] | $\beta$ | |
| $Y_2SiBe_2O_7$ | RT | $P\bar{4}2_1m$ | 7.283(2) | | 4.755(1) | | 69B1 |
| $Y_2Si_3O_3N_4$ | RT | $P\bar{4}2_1m$ | 7.6137 | | 4.9147 | | 97W1, 97W2 |
| $Y_2Si_3O_3N_4$ | RT | $P\bar{4}2_1m$ | 7.6083 | | 4.9113 | | 96M1 |
| $Li_6[Si_2O_7]$ | RT | $P\bar{4}2_1m$ | 7.715 | | 4.88 | | 69W1 |
| $Li_2Si_3O_7$ | RT | Orth. | 6.00 | 19.69 | 4.86 | | 70W1 |

1) $Ca_2MgSi_2O_7$;
2) $Ca_{1.97}Mg_{1.00}Si_{2.01}O_7$;
3) $Sr_2MgSi_2O_7$;
4) $(Ca_{1.93}Mn_{0.06}Na_{0.04}K_{0.01}Pb_{0.01})[Zn_{0.93}Mg_{0.09}Al_{0.05}Fe_{0.04}Si_{1.93}]O_7$; two data sets are for X-ray analysis by $FeK_\alpha$ (first line) and $CuK_\alpha$ radiation, respectively
5) $(Ca_{1.85}Na_{0.14}Pb_{0.01})(Zn_{0.85}Al_{0.07}Mg_{0.03}Mn^{3+}_{0.04}Fe^{3+}_{0.02})Si_{2.00}O_7$ (average structure);
6) $(Ca_{1.99}Mg_{0.01})(Mg_{0.49}Fe^{3+}_{0.24}Al_{0.27})_{T1}(Fe^{3+}_{0.24}Al_{0.24}Si_{1.52})_{T2}O_7$;
7) $(Ca_{1.98}Mg_{0.01})(Mg_{0.68}Fe^{3+}_{0.14}Al_{0.18})_{T1}(Fe^{3+}_{0.15}Al_{0.15}Si_{1.70})_{T2}O_7$;
8) $Ca_{2.00}(Al_{0.79}Fe^{3+}_{0.21})_{T1}(Al_{0.71}Fe^{3+}_{0.29}Si_{1.00})_{T2}O_7$;
9) $Ca_{2.00}(Mg_{0.52}Fe^{3+}_{0.28}Ga_{0.20})_{T1}(Fe^{3+}_{0.14}Ga_{0.34}Si_{1.52})_{T2}O_7$;
10) $Ca_{2.00}(Mg_{0.62}Fe^{3+}_{0.24}Ga_{0.14})_{T1}(Fe^{3+}_{0.12}Ga_{0.25}Si_{1.63})_{T2}O_7$;
11) $Ca_{2.00}(Fe^{3+}_{0.25}Ga_{0.75})_{T1}(Fe^{3+}_{0.25}Ga_{0.75}Si_{1.00})_{T2}O_7$;
12) $(Na_{0.47}Ca_{1.53})(Mg_{0.52}Fe^{3+}_{0.48})_{T1}(Fe^{3+}_{0.01}Si_{1.99})_{T2}O_7$;
13) $Sr_{2.00}(Al_{0.74}Fe^{3+}_{0.26})_{T1}(Al_{0.76}Fe^{3+}_{0.24}Si_{1.00})_{T2}O_7$;
14) natural sample;
15) $(Ba_{1.95}Ca_{0.05})(Ti_{0.96}Mn_{0.01}Mg_{0.02}Fe_{0.05})Si_{2.00}O_7$;
16) $Ca_{1.69}Na_{0.19}(Be_{0.82}Al_{0.14})Si_{1.97}(O_{6.49}OH_{0.51})$;
17) $K_2Na_6Be_4Si_{14}O_{36}\cdot 9H_2O$;
18) $(La_{2.1}Ce_{1.7}Ca_{0.2})(Sr_{2.1}Ca_{1.9})Na_2(Na_{0.8}Mn_{0.2})(Zn_{1.5}Mg_{1.3}Fe^{2+}_{0.7}Mn_{0.5})(Si_{5.85}Fe^{3+}_{0.15})O_{17}$;
19) $CaNaBeSi_2O_6F$;
20) $Ca_{0.85}Na_{0.95}(Be_{0.89}Al_{0.02})Si_{2.07}O_6(F_{0.97}OH_{0.12})$;
21) $(Ca,R)CaNa_2Be_2Si_4O_{12}(F,O)_2$;
22) $Ca_{1.37}Na_{0.63}Be(Si_{1.87}Al_{0.13})O_{6.25}F_{0.75}$.
23) Growth in the presence of melt at 9 GPa, 1200 °C
24) Heating hydrous precursor $Na_2Si_3O_7\cdot H_2O$ in air stream at 440 °C

**Table 4.** Thermal expansion coefficients.

| Sample | $\alpha_a$ [°C$^{-1}$] | $\alpha_c$ [°C$^{-1}$] | Refs. |
|---|---|---|---|
| Fresnoite ($Ba_2TiSi_2O_8$) | $9.8 \cdot 10^{-6}$ | $10.3 \cdot 10^{-6}$ | 77K1 |
| | $8.7 \cdot 10^{-6}$ | $9.3 \cdot 10^{-6}$ | 77H1[3] |
| | $5.7 \cdot 10^{-6}$ | $9.9 \cdot 10^{-6}$ | 85M1[4] |
| Åkermanite ($Ca_2MgSi_2O_7$)[1] | $\alpha_{[100]} = 6.901(5) \cdot 10^{-6} + 1.834(2) \cdot 10^{-8}\ T$ | $\alpha_{[100]} = -2.856(1) \cdot 10^{-6} + 11.280(1) \cdot 10^{-8}\ T$ | 92W1 |
| Hardystonite ($Ca_2ZnSi_2O_7$)[2] | $\alpha_{[100]} = 15.562(5) \cdot 10^{-6} - 1.478(3) \cdot 10^{-8}\ T$ | $\alpha_{[100]} = -11.115(5) \cdot 10^{-6} + 11.326(3) \cdot 10^{-8}\ T$ | 92W1 |

[1] above ~ 95 °C; [2] above ~ 140 °C ($T$ in °C); [3] near 273 K; [4] near room temperature.

**Table 5.** Elastic properties, at room temperature.

| Silicate | $c_{ij}$ [GPa] | | | | | | Young modulus $E$ [GPa] | Bulk modulus $K$ [GPa] | Shear modulus $G$ [GPa] | Poisson ratio $\nu$ | Refs. |
|---|---|---|---|---|---|---|---|---|---|---|---|
| | $c_{11}$ | $c_{33}$ | $c_{44}$ | $c_{66}$ | $c_{12}$ | $c_{13}$ | | | | | |
| Åkermanite[1] | 159.40 | 149.43 | 30.26 | 58.1 | 76.53 | 57.80 | 106.7 | 94.4 | 40.7 | 0.312 | 90L1 |
| Fresnoite[2] | 165.5 | 99.9 | 31.7 | 69.4 | 57.7 | 43.6 | | | | | 77H1 |
| Fresnoite[2] | 140 | 83 | 33 | 59 | 36 | 24 | | | | | 77K1 |

[1] $Ca_{1.97}Mg_{1.00}Si_{2.01}O_7$;
[2] $Ba_2TiSi_2O_8$.

**Table 6.** Magnetic properties.

| Silicate | $T$ [K] | $p_s$ [$\mu_B$/M atom] | $T_{ord}$ [K] | $\Theta$ [K] | $p_{eff}$[1] [$\mu_B$/M atom] | Refs. |
|---|---|---|---|---|---|---|
| $Na_2Mn_2Si_2O_7$ | | | 26 | –91 | 5.28 | 67K1 |
| $BaCo_2Si_2O_7$ | 2 | 0.4 | | –46 | 4.70 | 93A1 |
| $Ba_2VOSi_2O_7$ | | | | | 1.73 | 01R2 |
| $Ba_{1.5}VOSi_2O_7$ | | | | | diamagnetic | 01R2 |
| $BaCu_2Si_2O_7$ | 2 | 0.15(3)‖***c***-axis | 9.00(5) | | | 01K1 |
| $BaCu_2Ge_2O_7$ | | | 8.6 | | | 01Y1 |
| $Ca_2CoSi_2O_7$ | | | | –24 | 4.17 | 82S1 |
| $Sr_2CoSi_2O_7$ | | | | –20 | 4.13 | 82S1 |

[1] determined from the Curie constant.

**Table 7.** Data obtained by $^{57}$Fe NGR method.

| Sample | Site | $\delta$ [1] [mm/s] | $\Delta Q$ [mm/s] | $DH$ [mm/s] | $A$ [%] | Refs. |
|---|---|---|---|---|---|---|
| $(Na_{0.47}Ca_{1.53})(Mg_{0.52}Fe^{3+}_{0.48})_{T1}(Fe^{3+}_{0.01}Si_{1.99})_{T2}O_7$(a) | $Fe^{3+}$(T1) | 0.100 | 1.202(6) | 0.41(1) | 100 | 85A1 |
| | $Fe^{3+}$(T2) | – | – | – | – | |
| $(Ca_{1.99}Mg_{0.01})(Mg_{0.49}Fe^{3+}_{0.24}Al_{0.27})_{T1}(Fe^{3+}_{0.24}Al_{0.24}Si_{1.52})_{T2}O_7$(b) | $Fe^{3+}$(T1) | 0.095(3) | 1.161(5) | 0.36(1) | 50(1) | 85A1 |
| | $Fe^{3+}$(T2) | 0.078(2) | 1.825(4) | 0.29(1) | 50(1) | |
| $(Ca_{1.98}Mg_{0.01})(Mg_{0.68}Fe^{3+}_{0.14}Al_{0.18})_{T1}(Fe^{3+}_{0.15}Al_{0.15}Si_{1.70})_{T2}O_7$(c) | $Fe^{3+}$(T1) | 0.107(4) | 1.256(7) | 0.33(1) | 47(1) | 85A1 |
| | $Fe^{3+}$(T2) | 0.096(2) | 1.930(5) | 0.28(1) | 53(1) | |
| $Ca_{2.00}(Al_{0.79}Fe^{3+}_{0.21})_{T1}(Al_{0.71}Fe^{3+}_{0.29}Si_{1.00})_{T2}O_7$(d) | $Fe^{3+}$(T1) | 0.154(3) | 1.086(6) | 0.37(2) | 43(2) | 85A1 |
| | $Fe^{3+}$(T2) | 0.125(4) | 1.888(6) | 0.30(1) | 57(2) | |
| $Sr_{2.00}(Al_{0.74}Fe^{3+}_{0.26})_{T1}(Al_{0.76}Fe^{3+}_{0.24}Si_{1.00})_{T2}O_7$(e) | $Fe^{3+}$(T1) | 0.184(3) | 1.322(7) | 0.38(2) | 52(2) | 85A1 |
| | $Fe^{3+}$(T2) | 0.145(4) | 1.780(7) | 0.29(1) | 48(2) | |
| $Ca_{2.00}(Mg_{0.52}Fe^{3+}_{0.28}Ga_{0.20})_{T1}(Fe^{3+}_{0.14}Ga_{0.34}Si_{1.52})_{T2}O_7$ | $Fe^{3+}$(T1) | 0.216(6) | 0.866(8) | 0.53(1) | 66(2) | 86A1 |
| | $Fe^{3+}$(T2) | 0.119(6) | 1.841(5) | 0.30(1) | 34(2) | |
| $Ca_{2.00}(Mg_{0.62}Fe^{3+}_{0.24}Ga_{0.14})_{T1}(Fe^{3+}_{0.12}Ga_{0.25}Si_{1.63})_{T2}O_7$ | $Fe^{3+}$(T1) | 0.219(5) | 0.895(6) | 0.558(8) | 68(1) | 86A1 |
| | $Fe^{3+}$(T2) | 0.129(5) | 1.856(4) | 0.309(7) | 32(1) | |
| $Ca_{2.00}(Fe^{3+}_{0.25}Ga_{0.75})_{T1}(Fe^{3+}_{0.25}Ga_{0.75}Si_{1.00})_{T2}O_7$ | $Fe^{3+}$(T1) | 0.151(9) | 0.84(1) | 0.52(2) | 50(2) | 86A1 |
| | $Fe^{3+}$(T2) | 0.125(5) | 1.816(9) | 0.35(2) | 50(2) | |

[1] relative to $\alpha$-Fe.

**Table 8.** Data obtained by $^{29}$Si MAS NMR spectroscopy.

| Silicate | $\delta_{ij}$ [ppm] [1] | | | | | $\eta$ [4] | Refs. |
|---|---|---|---|---|---|---|---|
| | $\delta_i$ [2] | $\delta_{11}$ | $\delta_{22}$ | $\delta_{33}$ | $\Delta\delta$ [3] | | |
| Åkermanite ($Ca_2MgSi_2O_7$) | –73 | –134 | –84 | –1 | 108 | 0.69 | 83S2 |
| Åkermanite | –73.3 | | | | | | 85J1 |
| Åkermanite: | | | | | | | |
| central line | –71.5 | | | | | | 89M1 |
| other lines | –73 | | | | | | |
| Gehlenite ($Ca_2Al_2SiO_7$) | –72 | –122 | –74 | –20 | 78 | 0.92 | 83S2 |
| $Y_2Si_3O_3N_4$ | –56.7 | | | | | | 88D1, 89N1 |
| $Na_2Si_3O_7$ | –91.9 ($Q^3$) | | | | | | 02K1 |
| | –102.5 ($Q^4$) | | | | | | |

[1] relative to TMS; [2] isotopic chemical shift; [3] $\Delta\delta = \delta_{33} - 1/2(\delta_{11} + \delta_{22})$; [4] $\eta = (\delta_{22} - \delta_{11})\,(\delta_{33} - \delta_i)^{-1}$.

**Table 9.** Piezoelectric properties ($k_{ij}$: electromechanical coupling factor, $f$: resonance frequencies, $d_{ij}$: piezoelectric constant; $\varepsilon_{ij}$: dielectric constant).

| Sample | $k_{ij}$ | $f$ [Hz] | $d_{ij}$ [C/N] · $10^{12}$ | $\varepsilon_{ij}$ | Piezoelectric coupling constant ($k^2$) | Temperature coeff. of resonance frequency [$10^{-6}$/K] | Temperature coeff. of delay $10^{-6}$ [$K^{-1}$] | Refs. |
|---|---|---|---|---|---|---|---|---|
| $Ba_2TiSi_2O_8$ | $k_{15} = 0.28$ | 1400 | $\|d_{15}\| = 18$ | $\varepsilon_{11}^T = 15$ [1)] | 0.0053 | –33(2); –38(1) [2)] for (110) plate | 38 | 76K1, 77K1 |
| | $k_{31} = 0.10$ | 2700 | $\|d_{31}\| = 2.7$ | | | 253 K ≤ $T$ ≤ 353 K | for $Y$-propagation direction on the | |
| | $k_{33} = 0.11$ | 2100 | $d_{33} = 3.8$ | $\varepsilon_{33}^T = 11$ [1)] | | –47 | $X$-cut surface | |
| $Ba_2TiSi_2O_8$ | $k_{15} = 0.34$ | | $d_{113}^T = 28$ [3)] | $\varepsilon_1 = 12.5$ [4)] | | | | 77H1 |
| | $k_t = 0.23$ | | $d_{311}^T = 9.5$ [3)] | $\varepsilon_3 = 8.55$ [4)] | | | | |
| | | | $d_{333}^T = 12$ [3)] | | | | | |
| $Ba_2TiSi_2O_8$ | | | | | 0.016(3) | | 51 $Z$-cut, $X$ propagating surface | 78M1 |
| $Ba_2TiSi_2O_8$ | | | | | 0.0158… 0.0165 | | 38 $Z$-axis cylinder cuts | 79Y1 |

[1)] at 1 kHz; [2)] values for fundamental and second mode; [3)] in $10^{-8}$ esu $dyn^{-1}$; [4)] at 10 MHz and 293 K.

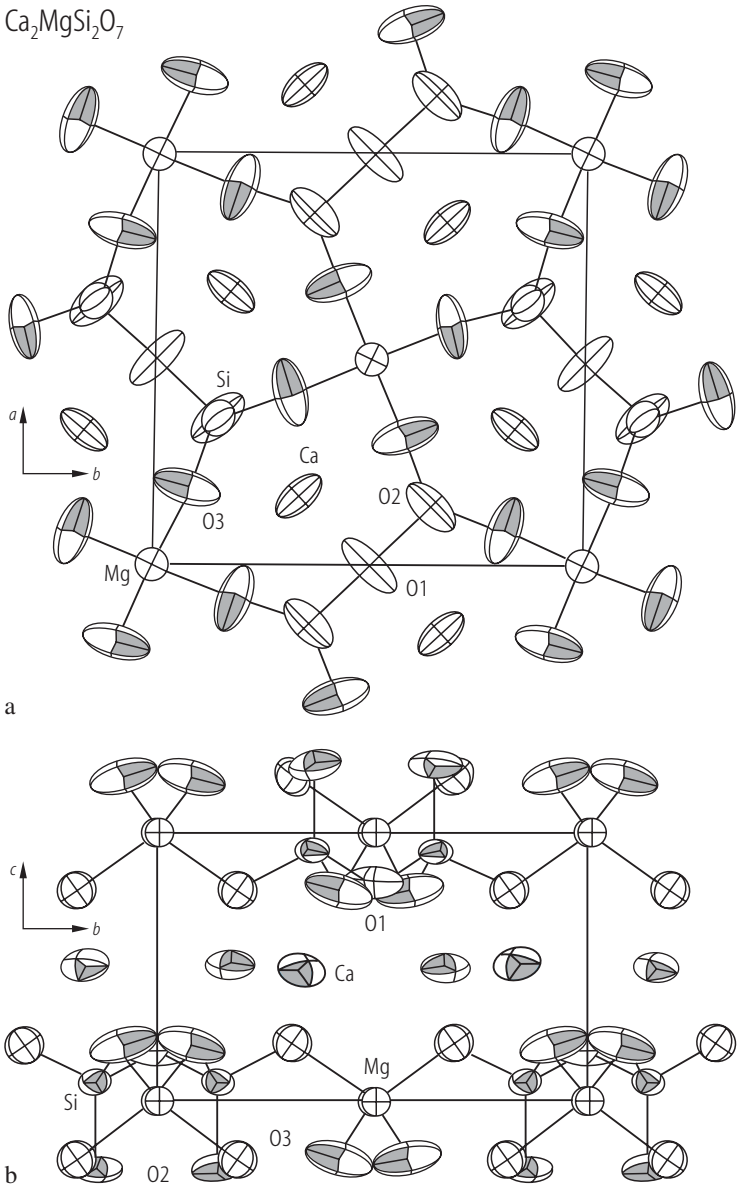


**Fig. 1.** $Ca_2MgSi_2O_7$. Crystal structure at room temperature **(a)** viewed along [001] and **(b)** viewed along [100]. Atomic displacement ellipsoids are drawn at the 99 % probability density level [97Y1].

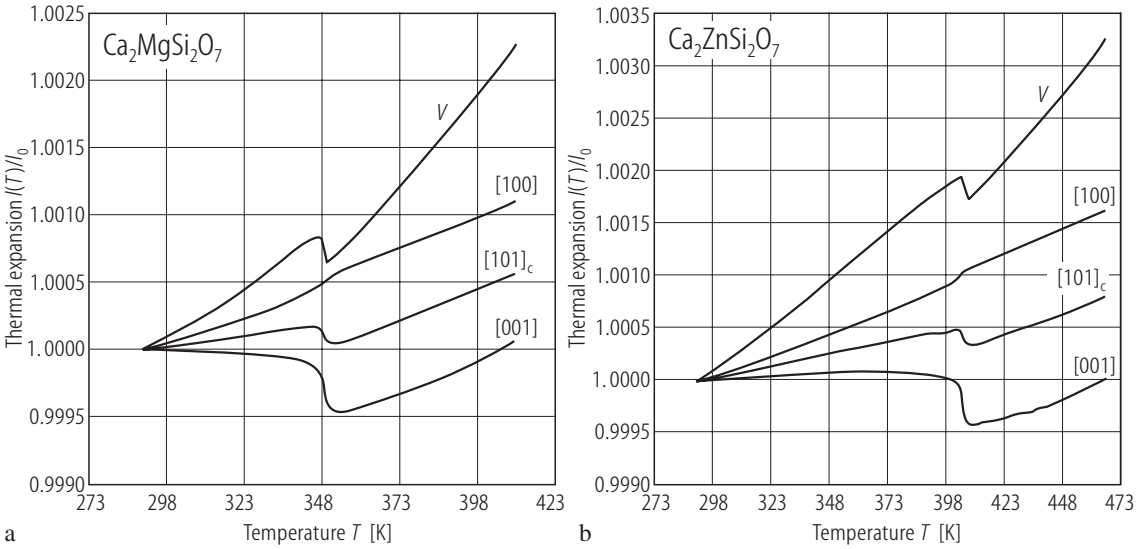


**Fig. 2.** $Ca_2MgSi_2O_7$ **(a)**, $Ca_2ZnSi_2O_7$ **(b)**. Linear and volume expansions. Curves for [100] and $[101]_c$ were directly measured and those for [001] and *V* were calculated [92W1].

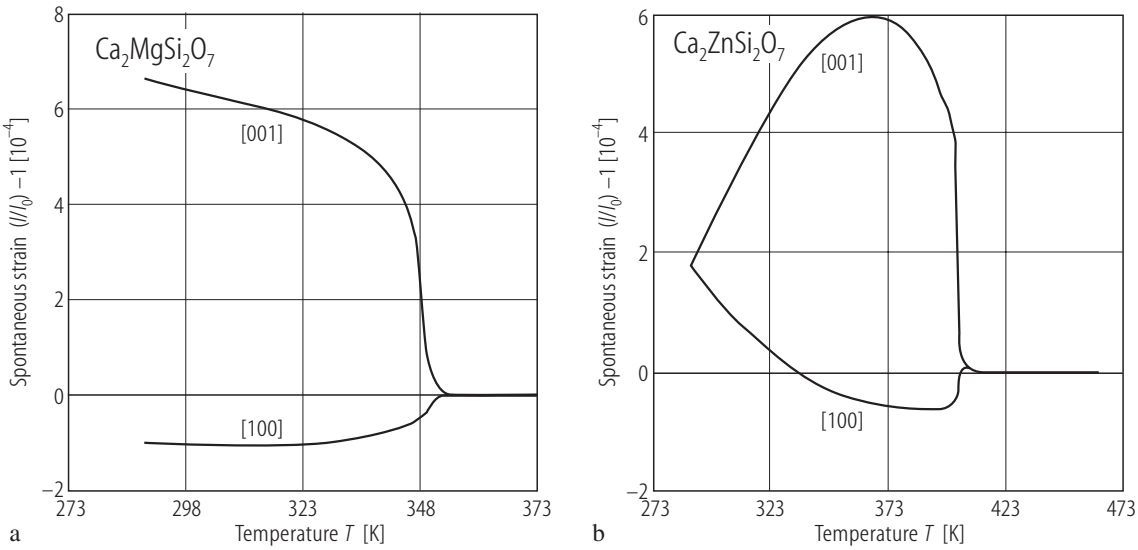


**Fig. 3.** $Ca_2MgSi_2O_7$ **(a)**, $Ca_2ZnSi_2O_7$ **(b).** Spontaneous strain calculated from the thermal expansion [92W1].

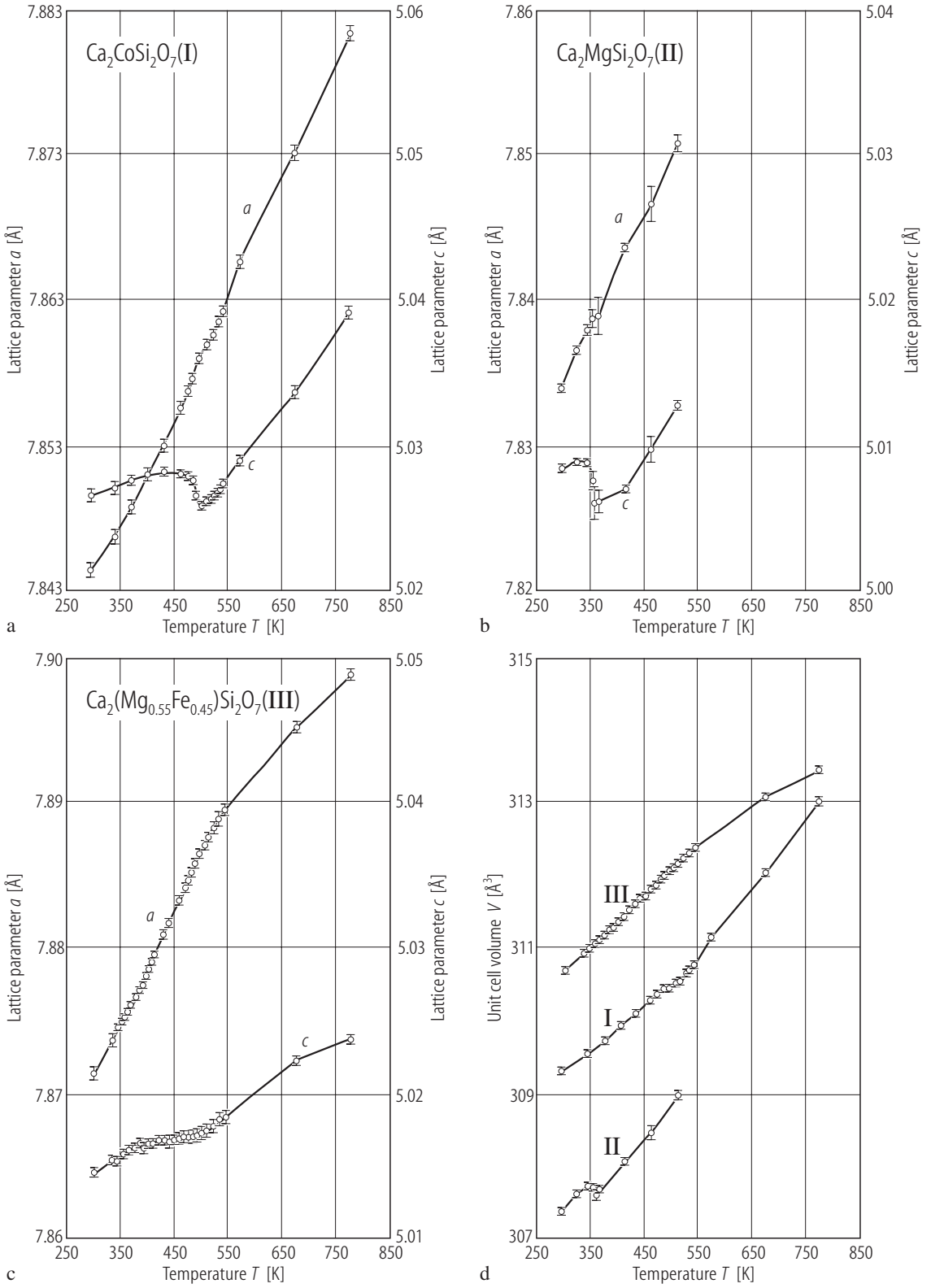


**Fig. 4.** $Ca_2CoSi_2O_7$ **(a)**; $Ca_2MgSi_2O_7$ **(b)**; $Ca_2(Mg_{0.55}Fe_{0.45})Si_2O_7$ **(c)**. Variation of cell parameters with temperature. In **(d)** are plotted the variation of the volumes for Co(I)-, Mg(II)- and $Mg_{0.55}Fe_{0.45}$(III)- **(c)** silicates [01K2].

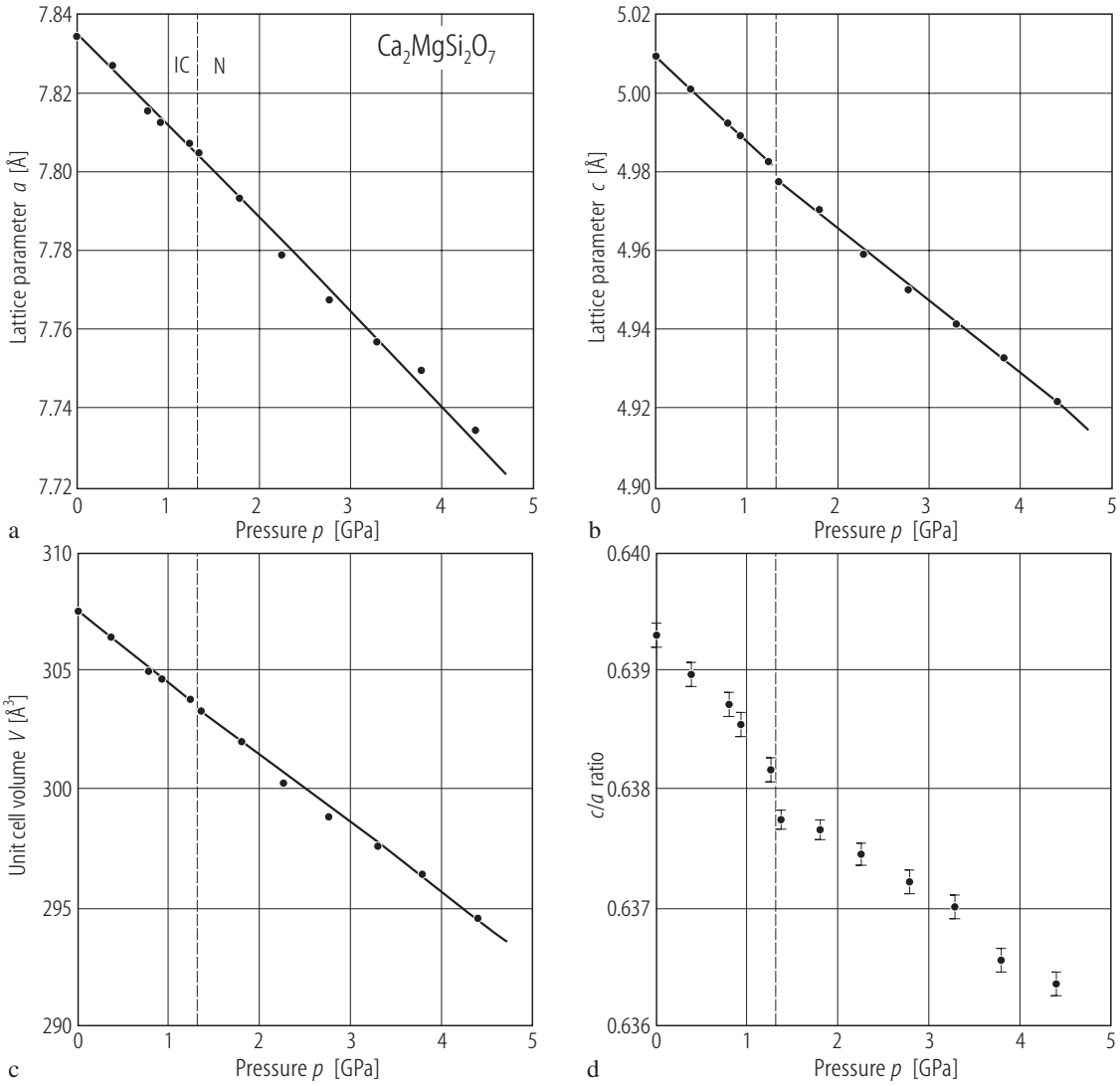


**Fig. 5.** $Ca_2MgSi_2O_7$. Variation of unit cell parameters with pressure at room temperature [97Y1].

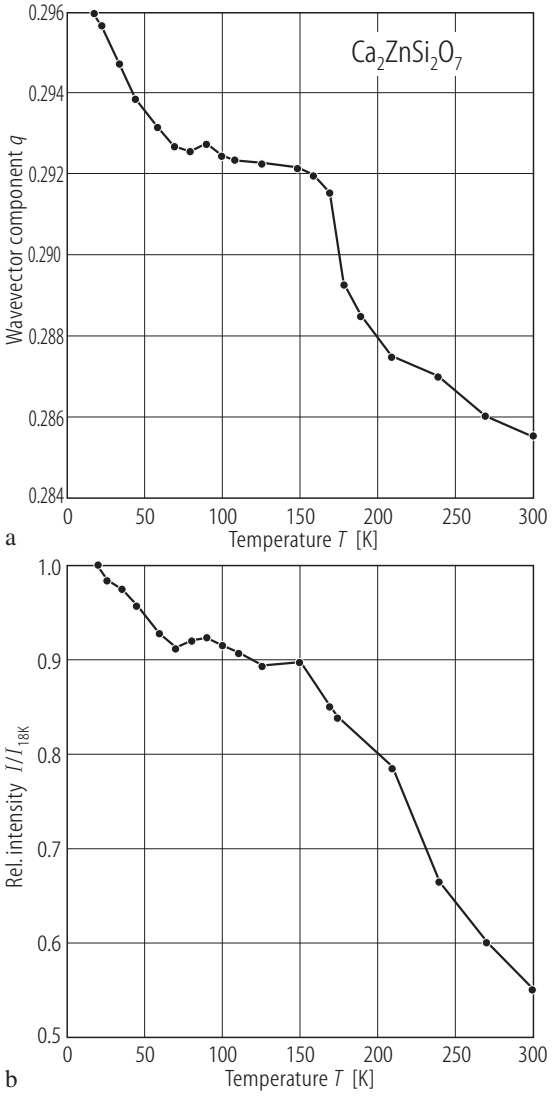


**Fig. 6.** $Ca_2ZnSi_2O_7$. Temperature dependences of **(a)** $q$ component of the modulation wave vector and **(b)** intensity of the satellite reflection $(25\bar{1}10)$.The magnitude of the intensity was normalized to the intensity observed at 18 K [02B1].

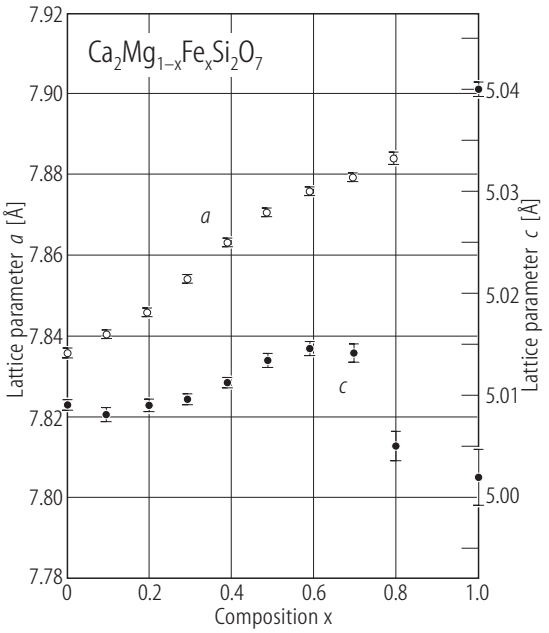


**Fig. 7.** $Ca_2Mg_{1-x}Fe_xSi_2O_7$. Lattice constants of a sample synthesized at 1170°C, 1 bar [87S1].

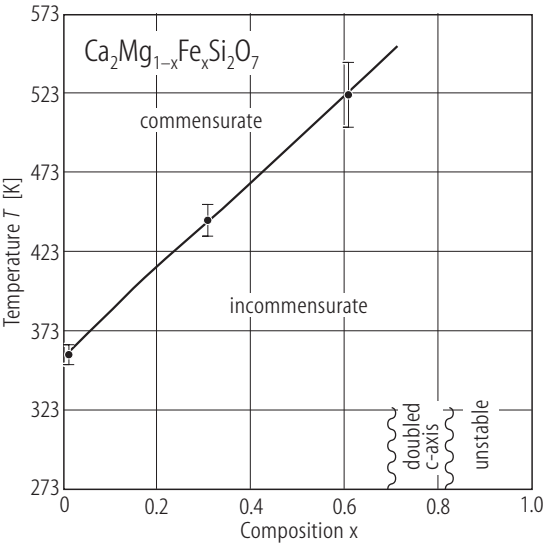


**Fig. 8.** $Ca_2Mg_{1-x}Fe_xSi_2O_7$. Composition dependence of the transition temperature [87S1].

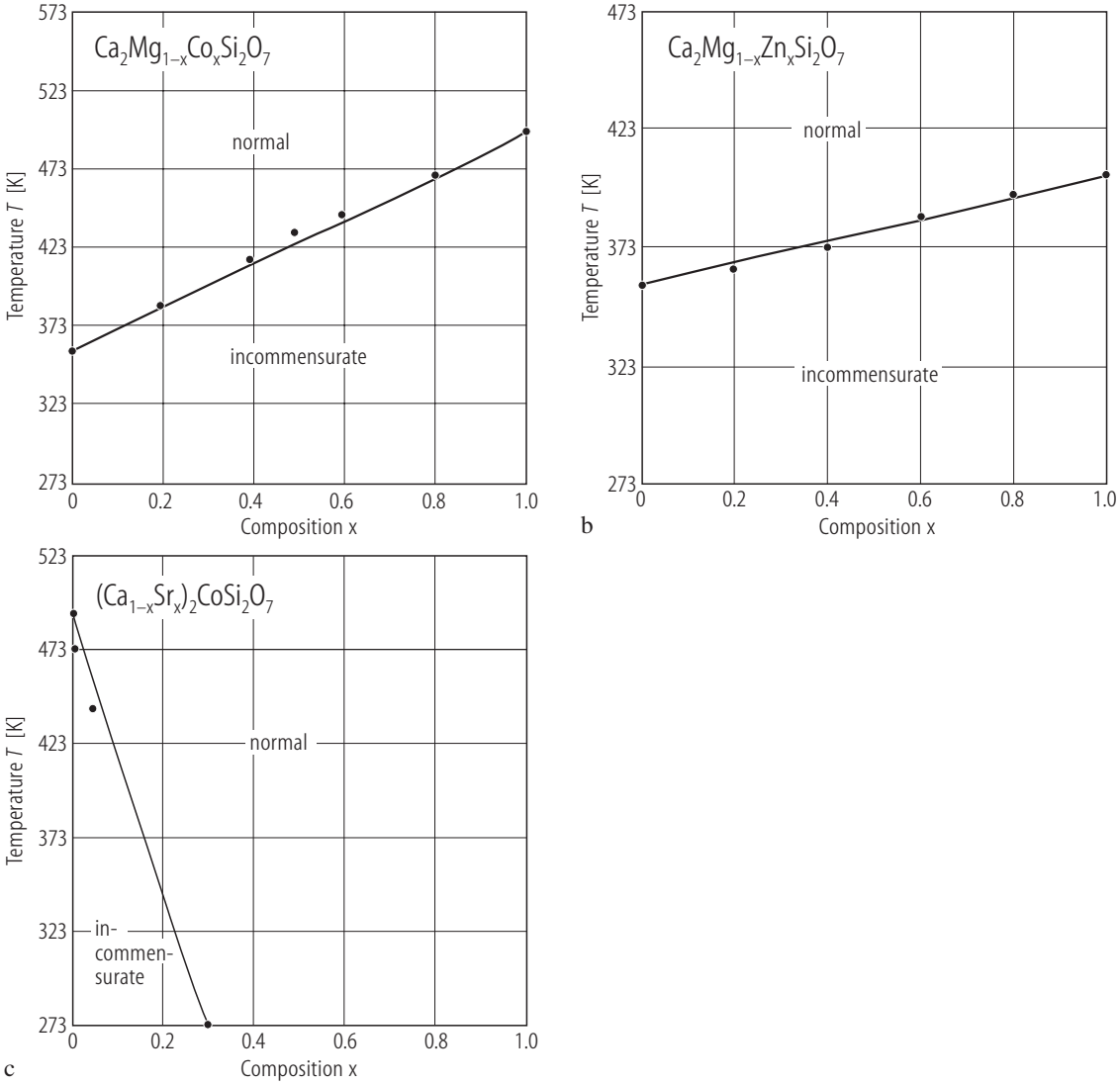


**Fig. 9.** $Ca_2Mg_{1-x}Co_xSi_2O_7$ **(a)**; $Ca_2Mg_{1-x}Zn_xSi_2O_7$ **(b)**; $(Ca_{1-x}Sr_x)CoSi_2O_7$ **(c)**. Phase diagrams of solid solutions [91I1].

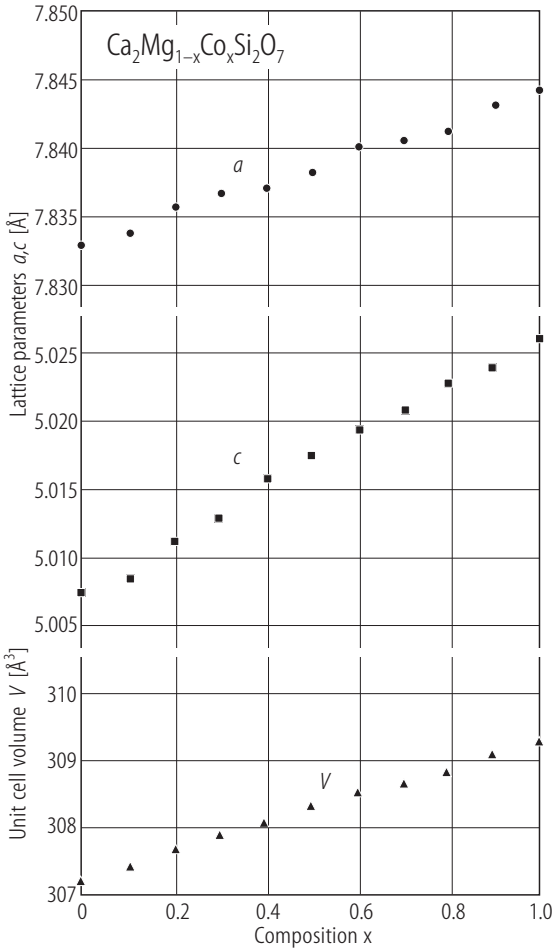


**Fig. 10.** $Ca_2Mg_{1-x}Co_xSi_2O_7$. Composition dependences of lattice parameters [96T1].

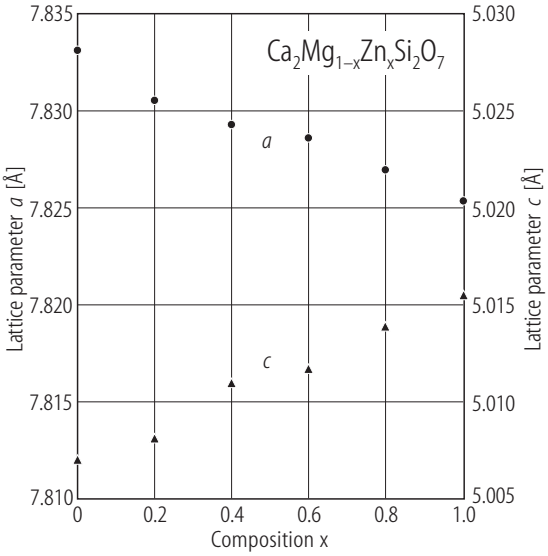


**Fig. 11.** $Ca_2Mg_{1-x}Zn_xSi_2O_7$. Composition dependences of lattice parameters [91I1].

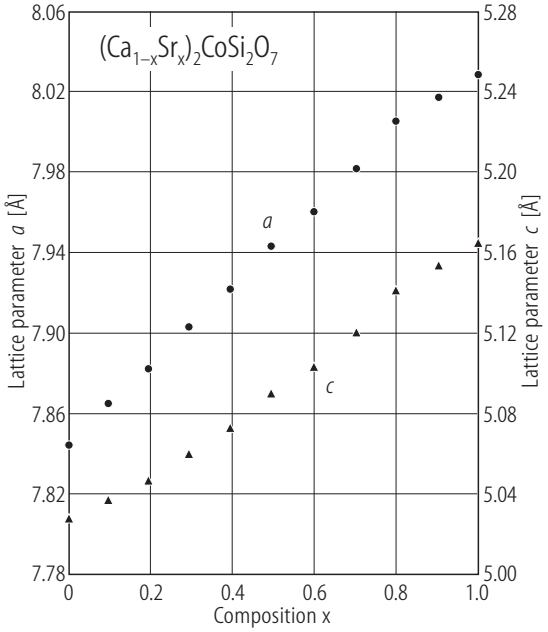


**Fig. 12.** $(Ca_{1-x}Sr_x)_2CoSi_2O_7$. Composition dependences of lattice parameters [90I1].

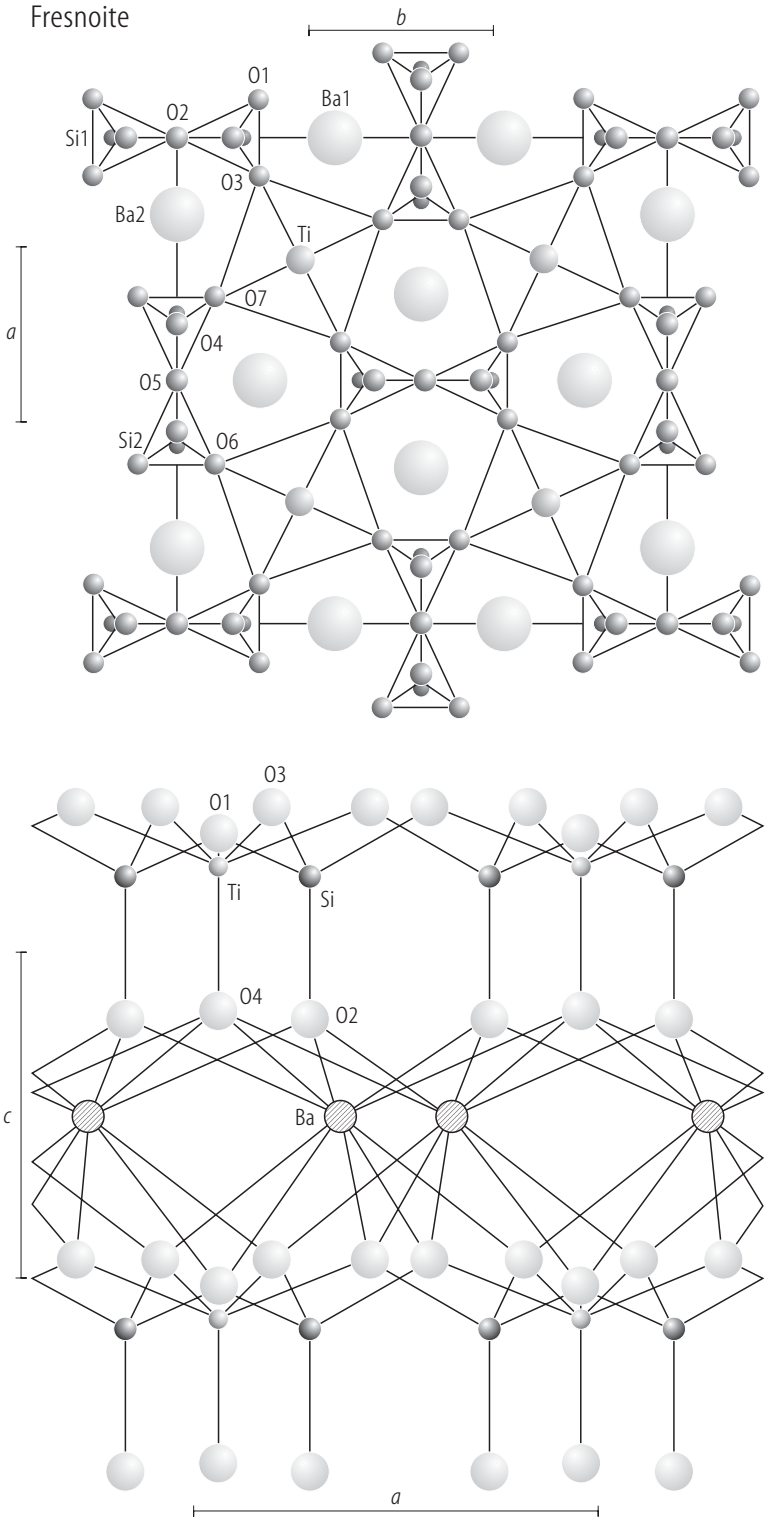


**Fig. 13.** Fresnoite, $Ba_2TiSi_2O_8$. Structure projected onto the ***c***-axis (top) and ***b***-axis (bottom) [89C1].

Nordite

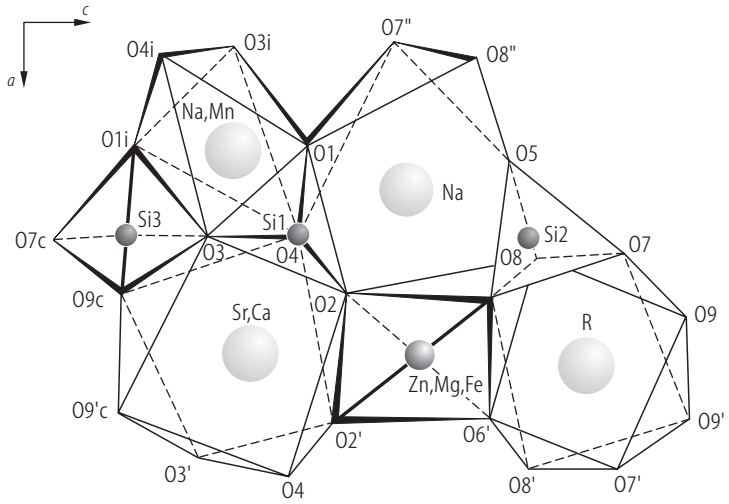


**Fig. 14.** Nordite. Crystal cell [70B1]. The atoms related by a glide plane, center of inversion and two kinds of twofold axes are denoted by the indices c, i, ‘, “.

$BaMn_2Si_2O_7$

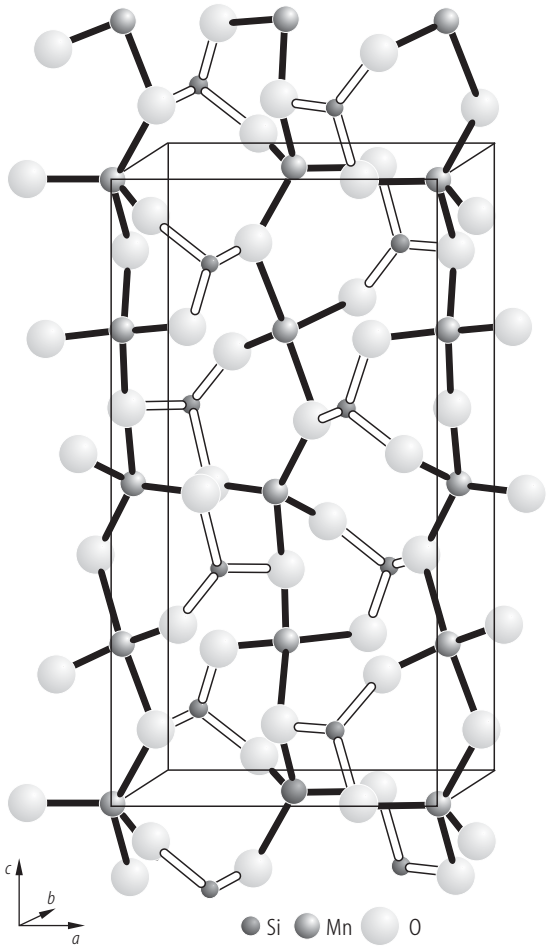


**Fig. 15.** $BaMn_2Si_2O_7$. Crystal structure where the one-dimensional chain arrangement of $MnO_4$ groups, as well as the interchain linkage, is emphasized [00L1].

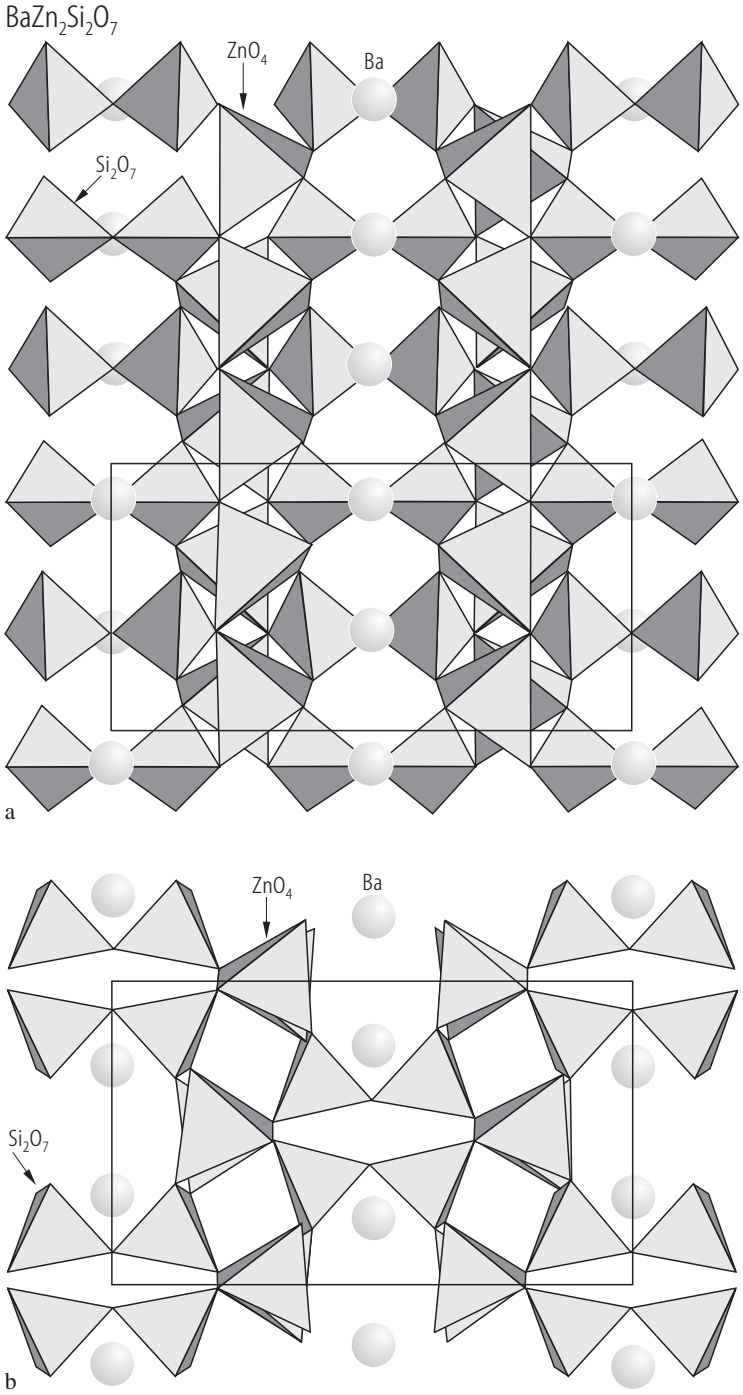


**Fig. 16(a, b)**. For caption see next page

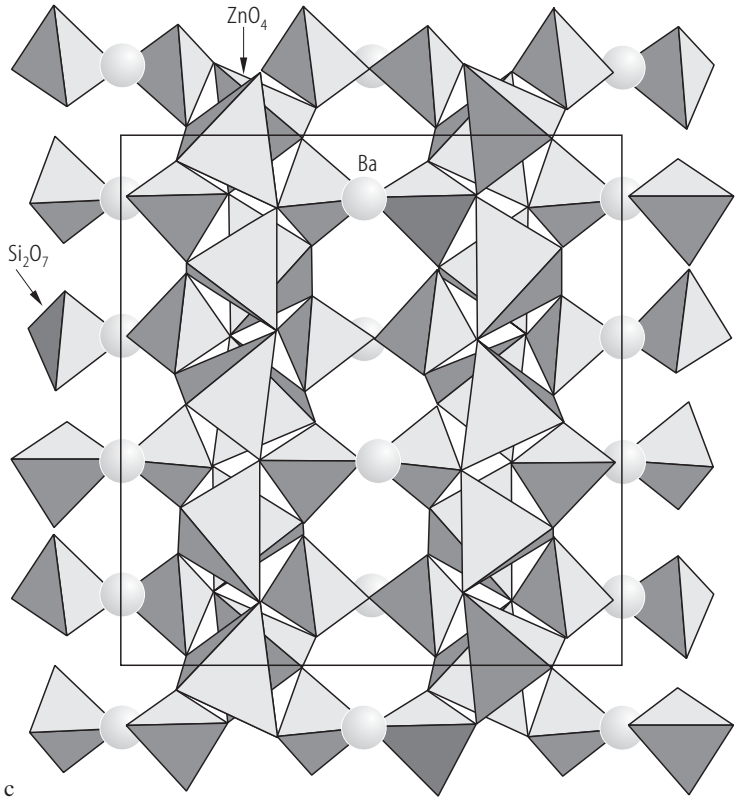


**Fig. 16.** $BaZn_2Si_2O_7$. The crystal structure. High-temperature phase projected along ***a***- **(a)** and ***c***-axis **(b)**; **(c)** low-temperature phase projected along ***a***-axis [99L2].

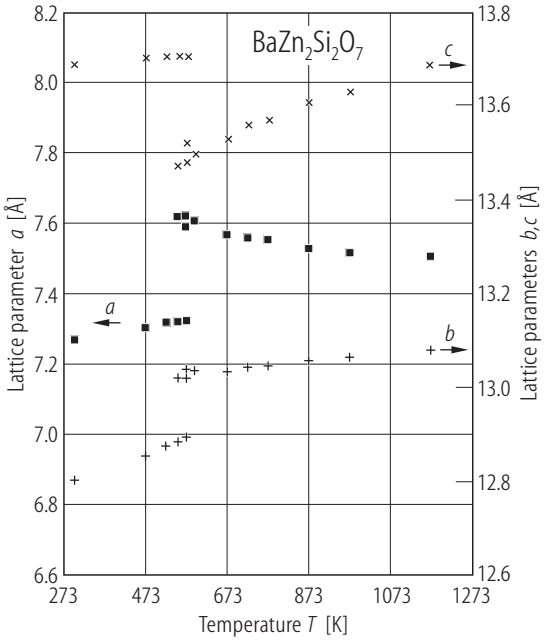


**Fig. 17.** $BaZn_2Si_2O_7$. Temperature dependences of the lattice constants [99L2]. The lattice parameter *c* of the HT phase is doubled in figure (for comparison).

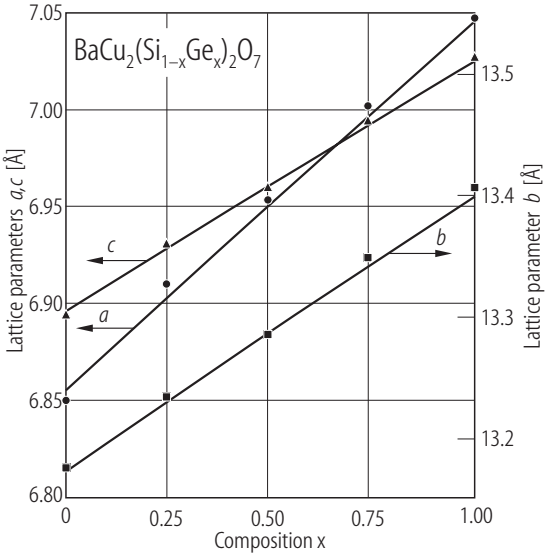


**Fig. 18.** $BaCu_2(Si_{1-x}Ge_x)_2O_7$. Composition dependence of the lattice parameters [01Y1].

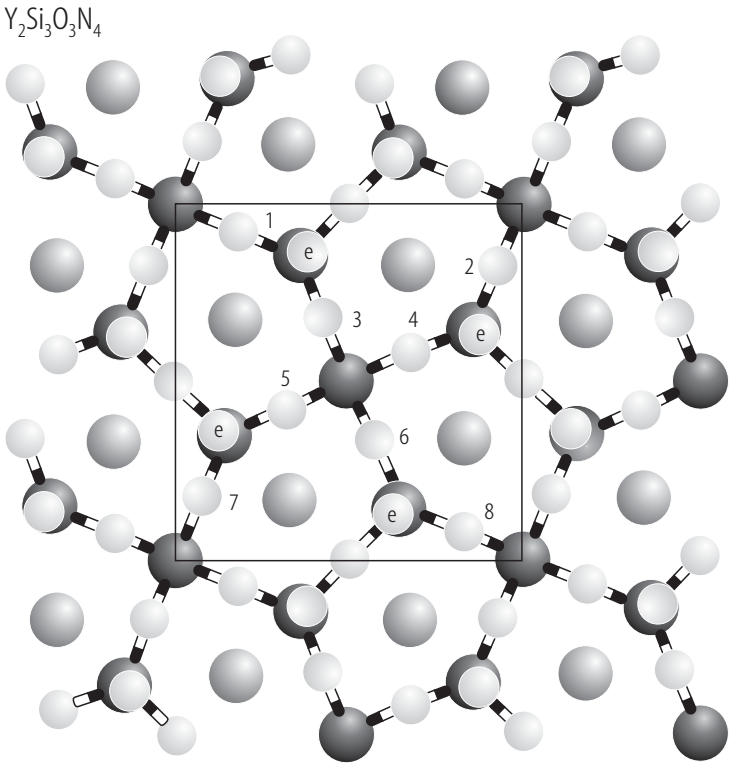


**Fig. 19.** $Y_2Si_3O_3N_4$ (melilite type I model). Schematic projection along [001]. The large lighter circles represent the Y atoms. The large darker circles represent the Si atoms. The medium open circles represent the anions (e for the 4e site, circles on lines for the 2c site, and the numbers for the 8f site) [00F1].

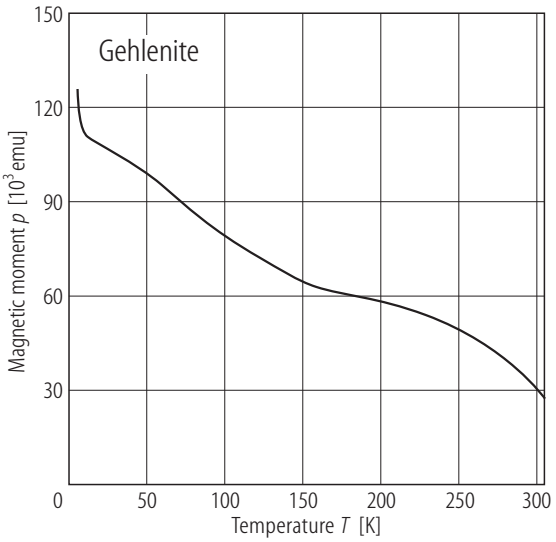


**Fig. 20.** Gehlenite. Temperature dependence of the magnetic moment in a field of 0.3 T [83N1].

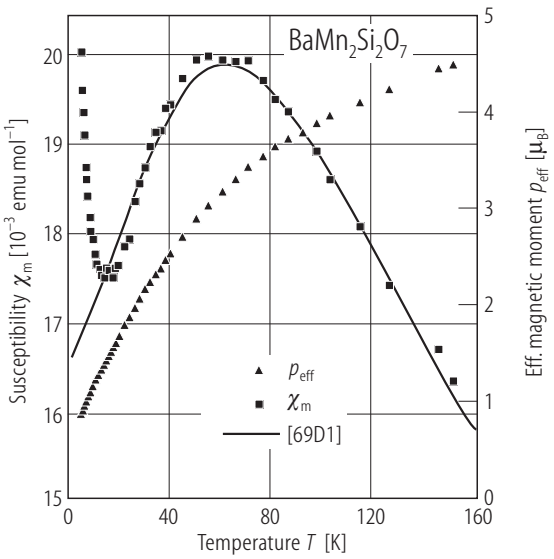


**Fig. 21.** $BaMn_2Si_2O_7$. Temperature dependences of the magnetic susceptibility and of effective magnetic moment [00L1]. Solid line is from [69D1].

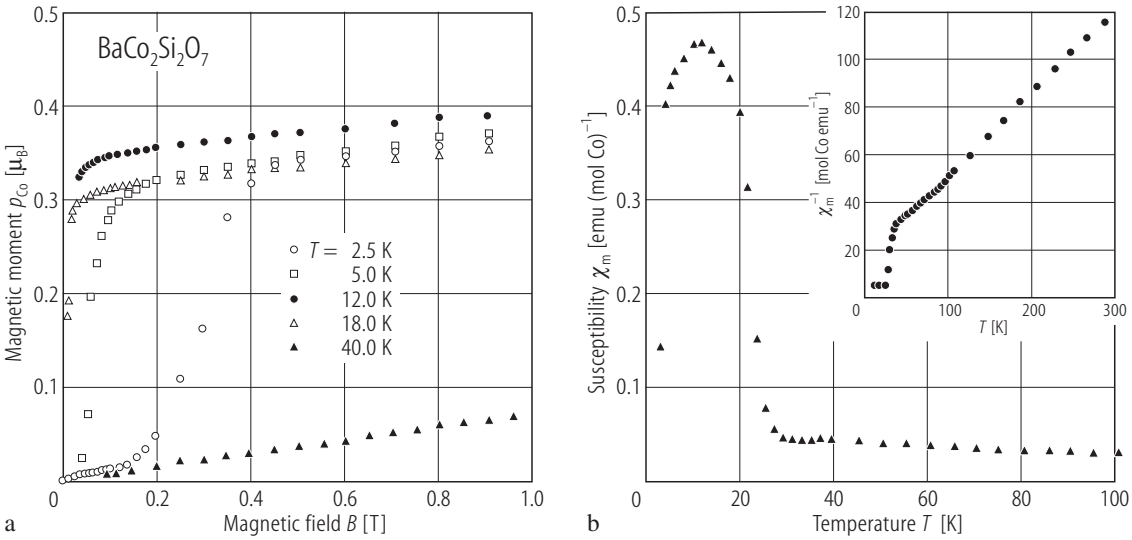


**Fig. 22.** $BaCo_2Si_2O_7$. **(a)** Magnetic moment per Co atom vs. magnetic field at different temperatures. **(b)** Temperature dependence of the magnetic susceptibilities in a field of 0.5 T. The insert shows a plot of the temperature dependence of the reciprocal susceptibilities [93A1].

For Fig. 23 see next page

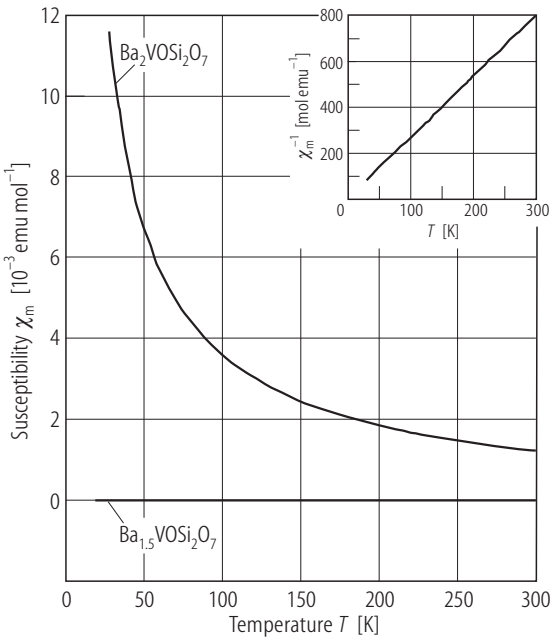


**Fig. 24.** $Ba_2VOSi_2O_7$ **(a)**, $Ba_{1.5}VOSi_2O_7$ **(b)**. Temperature dependences of the magnetic susceptibilities. In inset is shown $\chi^{-1}$ vs. $T$ plot for $Ba_2VOSi_2O_7$ [01R2].

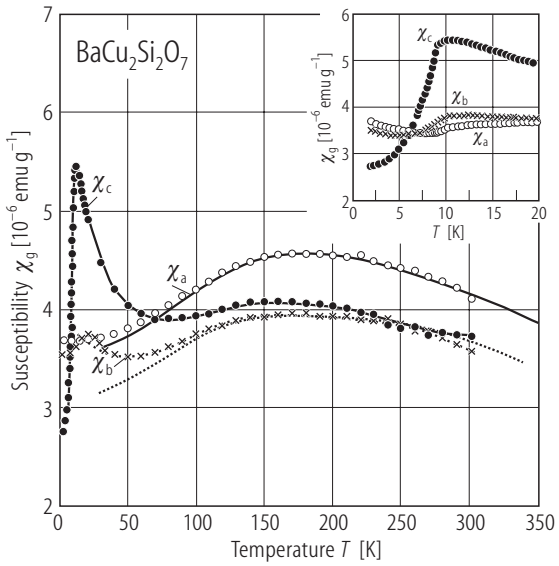


**Fig. 25.** $BaCu_2Si_2O_7$. Magnetic susceptibilities of a single crystal measured along the principal axes in a field of $\mu_o H$ = 0.1 T. Solid and dotted lines are the fits to the theoretical Bonner-Fisher (BF) curve. The inset shows magnified curves around $T_N$ [99T1].

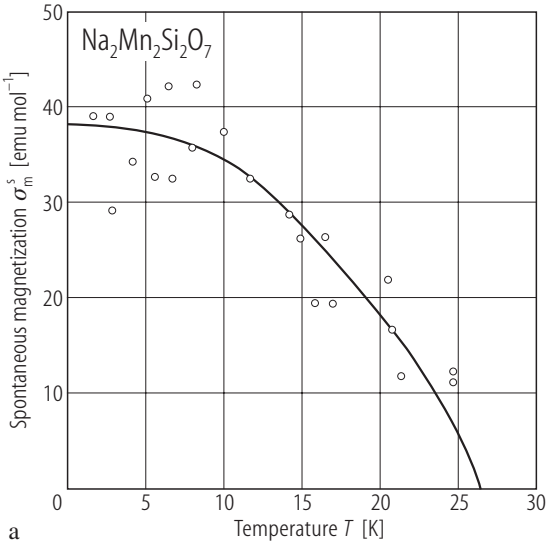


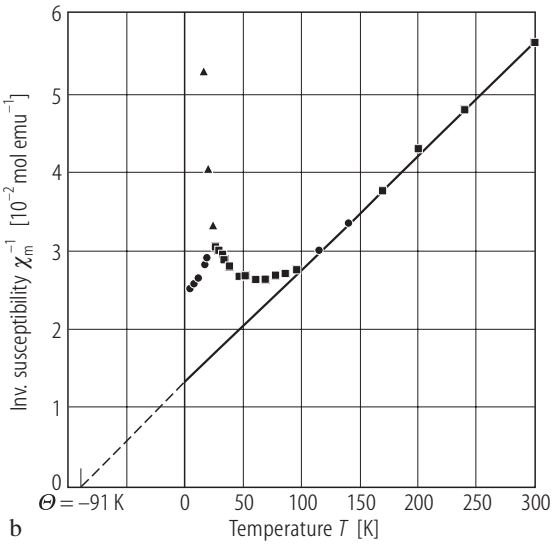


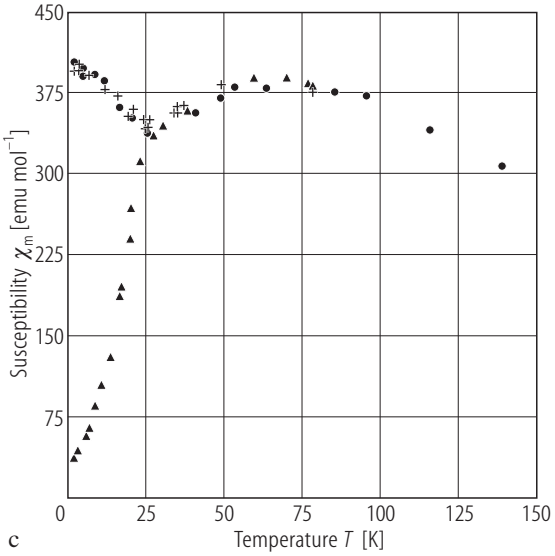


**Fig. 23.** $Na_2Mn_2Si_2O_7$. Temperature dependences of **(a)** spontaneous magnetization; **(b)** inverse magnetic susceptibilities in the symmetry plane (●) and along ***b***-axis (▲), isotropic values (■); **(c)** magnetic susceptibility in the symmetry plane (+, ●), along ***b***-axis (▲) [67K1]. Solid line in **(a)** is only guide for the eye.

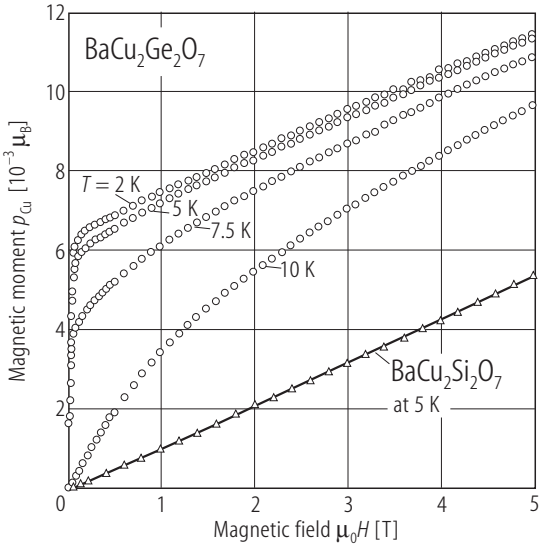


**Fig. 26.** $BaCu_2Si_2O_7$, $BaCu_2Si_2O_7$. Magnetic moment per Cu atom vs. magnetic field at various temperatures [01Y1].

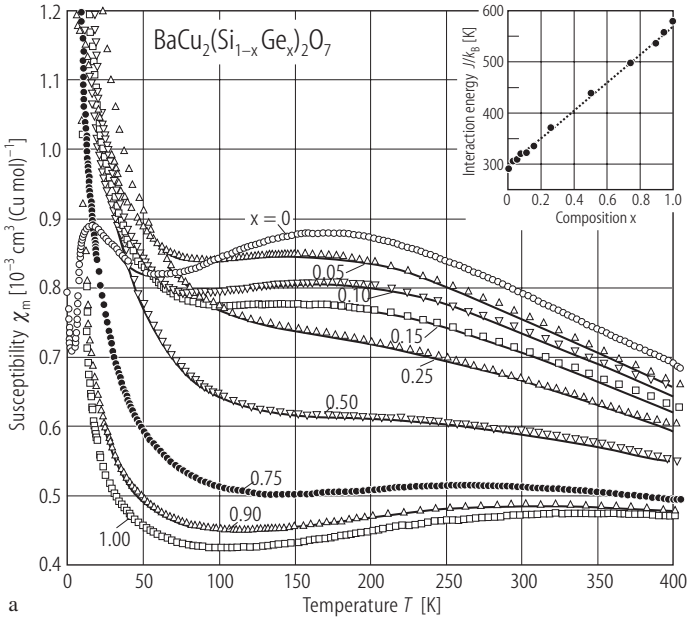


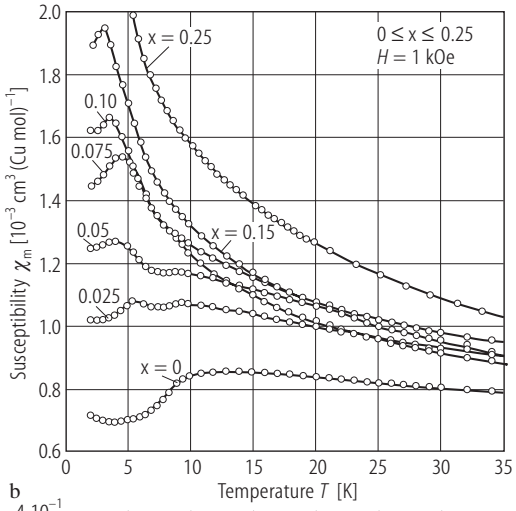


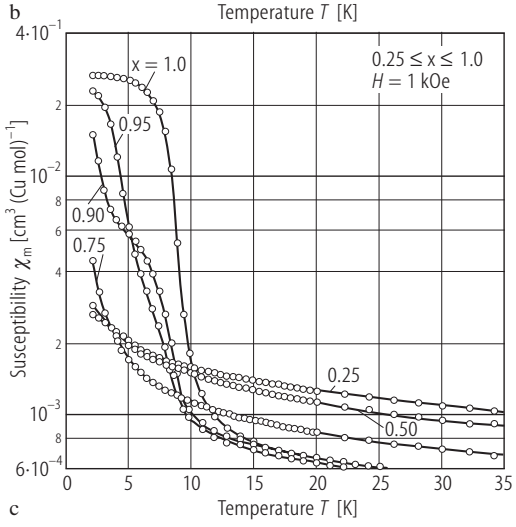


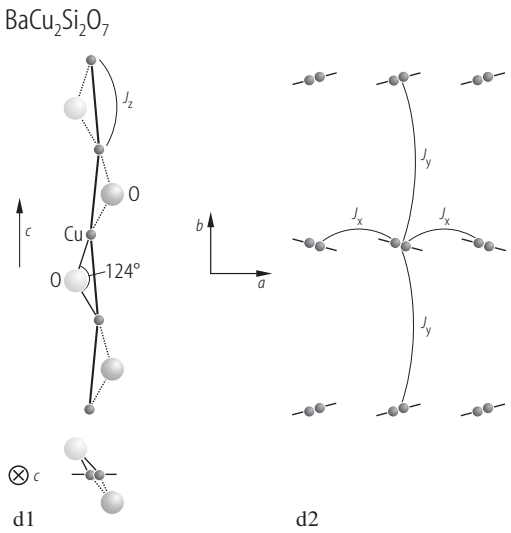


**Fig. 27.** $BaCu_2(Si_{1-x}Ge_x)_2O_7$. **(a)** Magnetic susceptibilities vs temperature at $T \leq 400$ K. The solid lines on each set of data points is a fit to the BF curve. The inset presents the composition dependence of the interchain interaction $J$. **(b, c)** Magnetic susceptibilities at low temperature for $0 \leq x \leq 0.25$ **(b)** and $0.25 \leq x \leq 1$ **(c)** [01Y1]. In **(d)** a schematic representation of magnetic ion arrangement in $BaCu_2Si_2O_7$ is shown. **(d1)** A single Cu–O chain. Cu–O–Cu bond angles are shown explicitely; **(d2)** relative arrangement of individual chains projected onto the (*ab*) crystallographic plane. Interchain interactions are characterized by two nearest-neighbor exchange constants $J_x$ and $J_y$ [99T1].

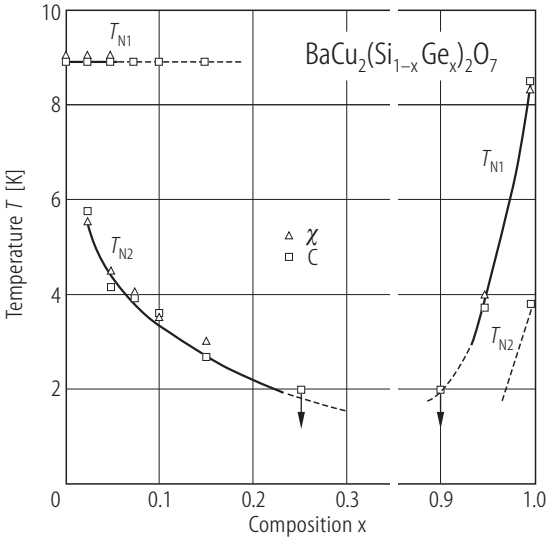


**Fig. 28.** $BaCu_2(Si_{1-x}Ge_x)_2O_7$. Magnetic phase diagram. The transition temperatures marked with diamond and squares were determined from $\chi(T)$ and $C(T)$, at low temperature [01Y1].

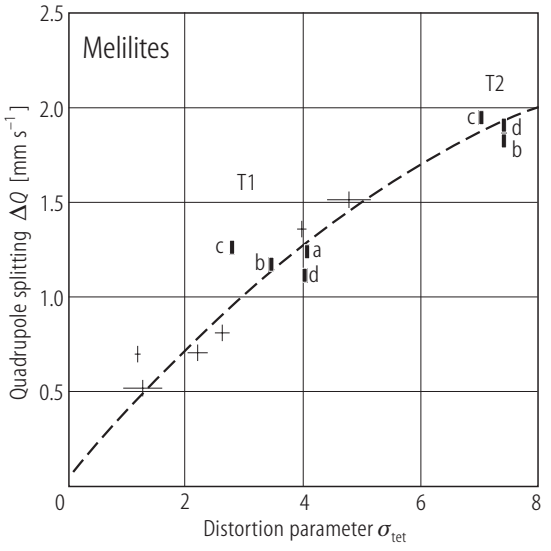


**Fig. 29.** Melilites. Relationship between quadrupole splitting, $\Delta Q$, of $Fe^{3+}$ (T1) and $Fe^{3+}$ (T2) and angular distortion parameter, $\sigma_{tet}$ (see text). Labels a-d refer to the composition given in Table 7. Crosses indicate the plots for various silicates. Broken line represents an empirical fit [81H2].

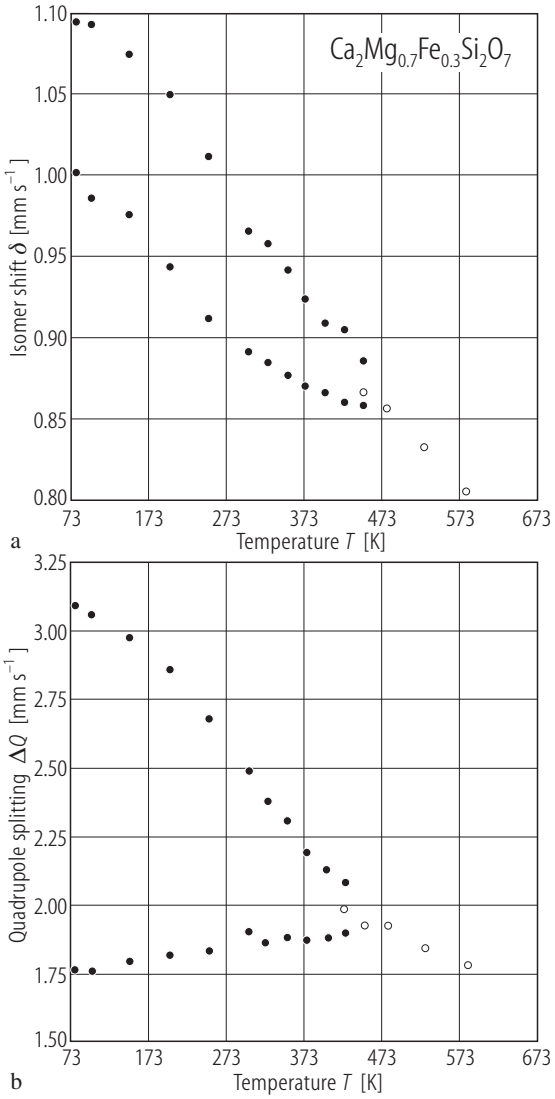


**Fig. 31.** $Ca_2Mg_{0.7}Fe_{0.3}Si_2O_7$. Temperature dependences of the isomer shifts ($\delta$, relative to α-Fe) and quadrupole splittings ($\Delta Q$) [87S1].

For Fig. 30 see next page

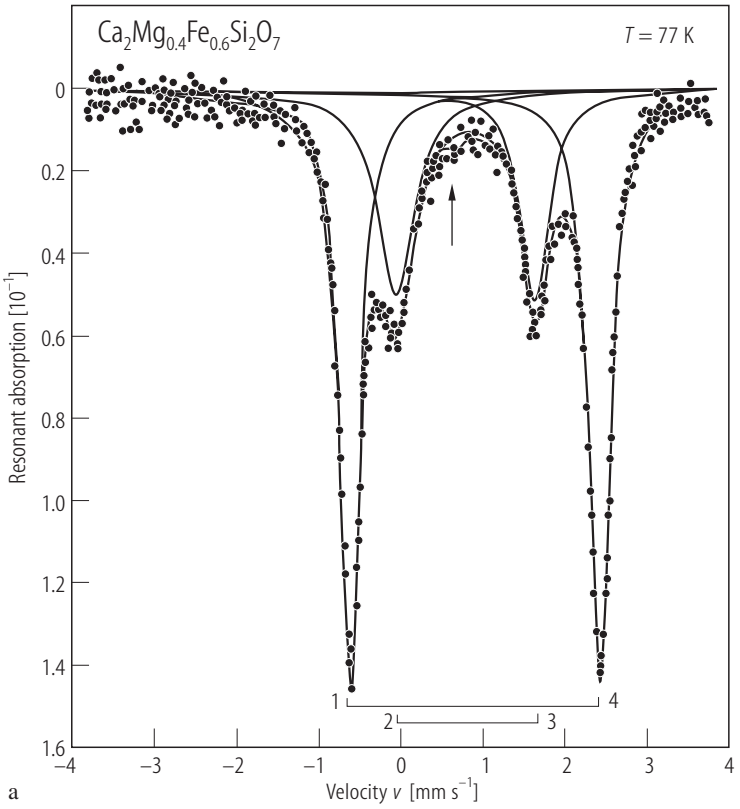


a

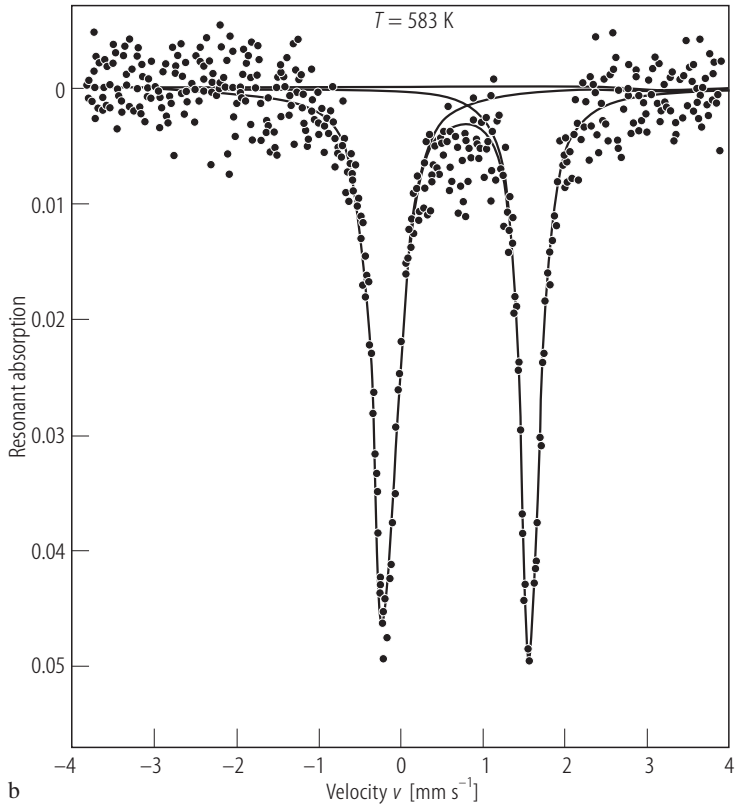


b

**Fig. 30.** $Ca_2Mg_{0.4}Fe_{0.6}Si_2O_7$. $^{57}Fe$ NGR spectra at **(a)** 77 K and **(b)** 583 K [87S1]. Arrow in **(a)** points to the position where a peak due to $Fe^{3+}$ would be expected.

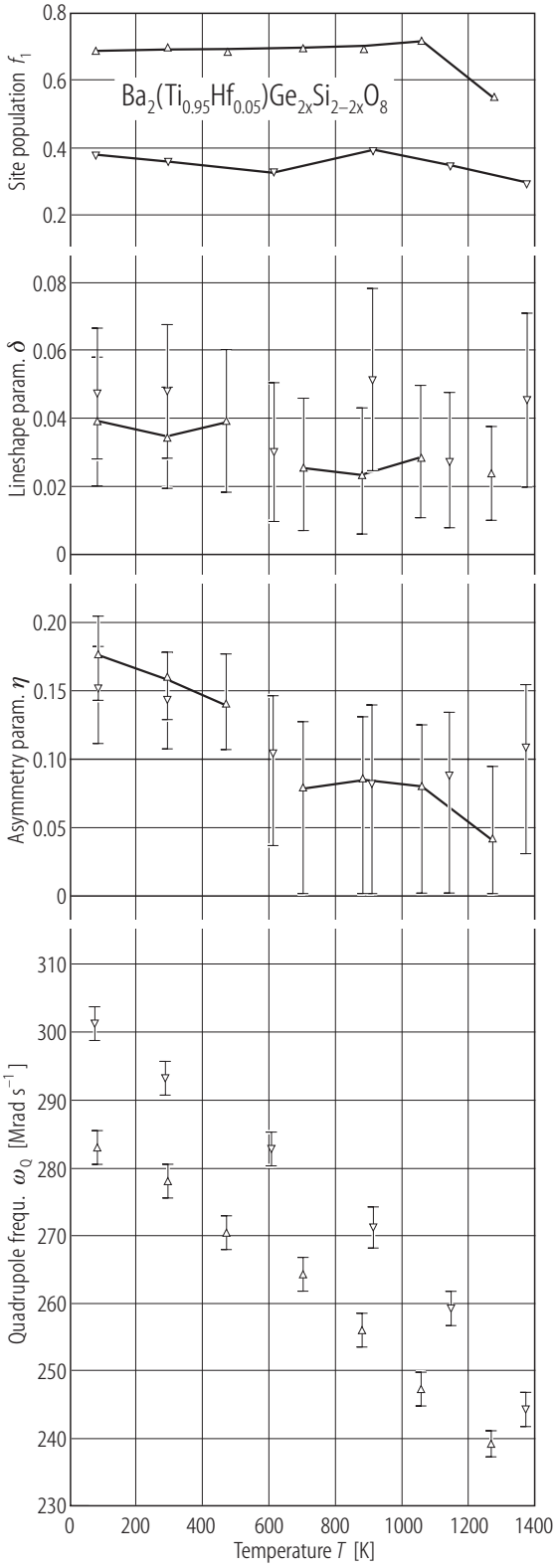


←

**Fig. 32.** $Ba_2(Ti_{0.95}Hf_{0.05})Ge_{2x}Si_{2-2x}O_8$ (x = 1.0 (Δ) and 0.2 (∇)). Quadrupole frequency $\omega_Q = [eQV_{zz}/ 4I(2I–1)\hbar]$ where $Q$ is the nuclear quadrupole moment and $I$ is the nuclear spin; the asymmetry parameter $\eta = (V_{xx}–V_{yy})/V_{zz}$ which describes the deviation from axial symmetry, $f_1=A_1/(A_1+A_2+A_3)$ is the site population and $\delta$ the lineshape parameter [89C1].

→

**Fig. 33.** $Ca_2MgSi_2O_7$. **(a)** $^{29}Si$ MAS NMR spectra at different temperatures. Only the center bands are shown, which are accompanied by moderate spinning sidebands of less than 10 % of the total signal intensity. **(b)** $^{29}Si$ spectrum at 340 K (1), calculated line shape (2) and the Gaussian fit to five individual bands (3). **(c)** $^{29}Si$ chemical shifts of the constituent Gaussian bands for the fitted spectra from 290 K…385 K.The percentage figures, shown at 290 K and 385 K, indicate the intensity of the specific band as a percentage of the total envelope intensity [89M1].

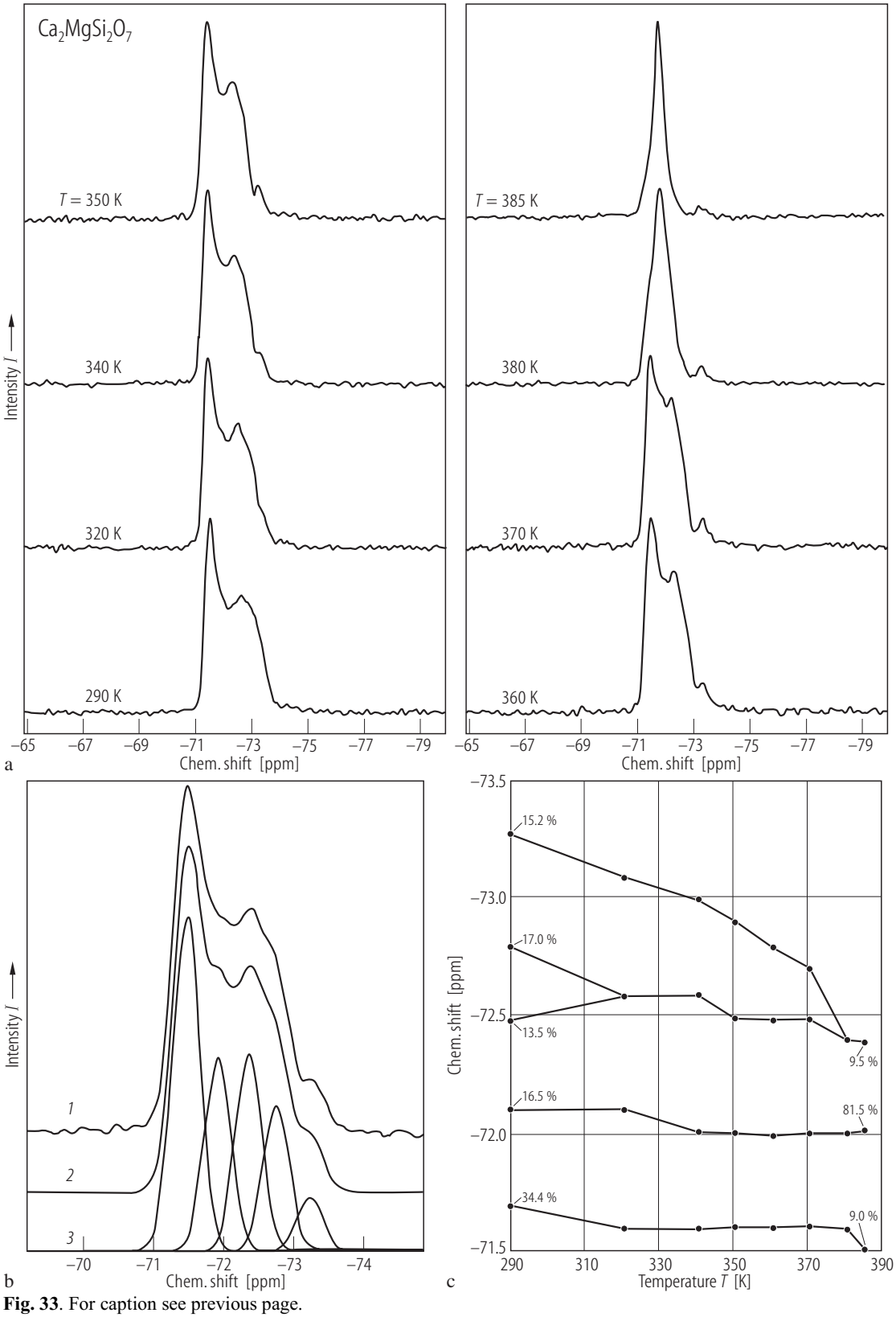


**Fig. 33**. For caption see previous page.

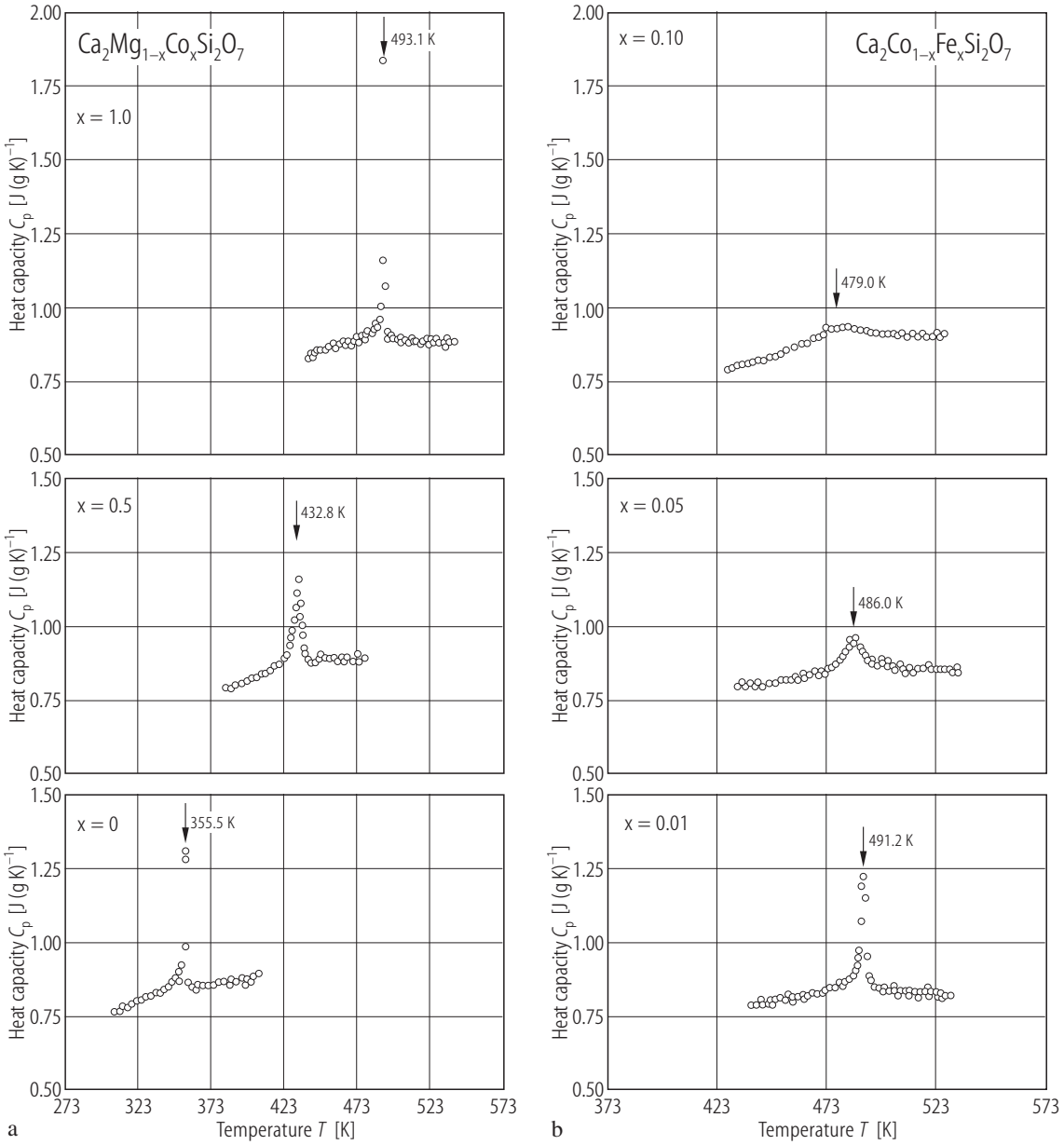


**Fig. 34.** $Ca_2Mg_{1-x}Co_xSi_2O_7$ **(a)**, $Ca_2Co_{1-x}Fe_xSi_2O_7$ **(b)**. Temperature dependence of the heat capacity around the IC-N transition points [91I1].

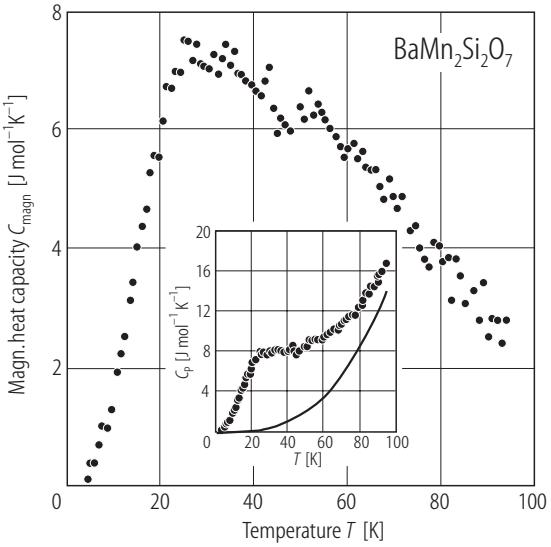


**Fig. 35.** $BaMn_2Si_2O_7$. Temperature dependence of the magnetic specific heat. The inserted figure shows the specific heat $C_p$ and lattice contribution (line) versus temperature [00L1].

For Fig. 36 see next page

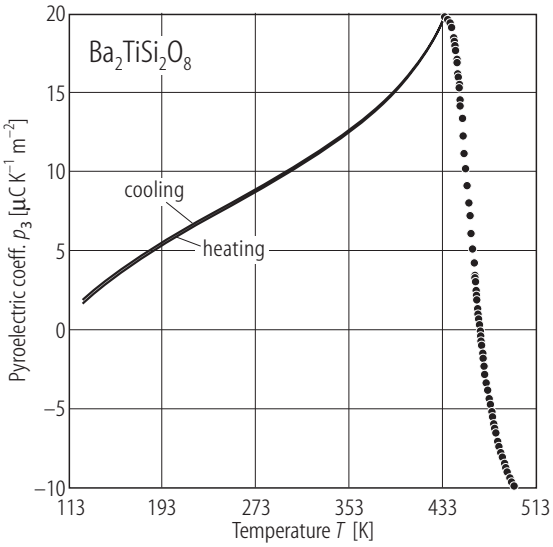


**Fig. 37.** $Ba_2TiSi_2O_8$ single crystal. Pyroelectric coefficeint ($p_3$) as a function of temperature [85M1].

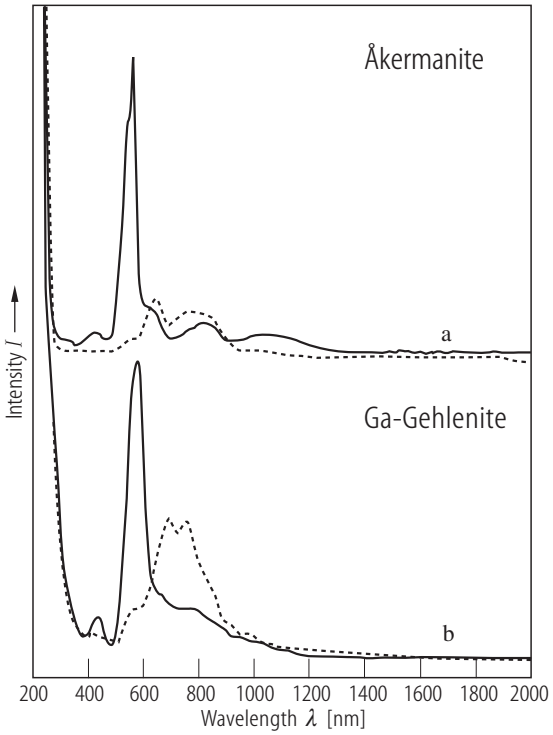


**Fig. 38.** Chromium doped åkermanite **(a)** and Ga-gehlenite **(b)**. Polarized absorption spectra [97S1]. Solid lines are for $\boldsymbol{E} \parallel \boldsymbol{c}$ and broken lines for $\boldsymbol{E} \perp \boldsymbol{c}$ , where $\boldsymbol{E}$ is the electric field vector.

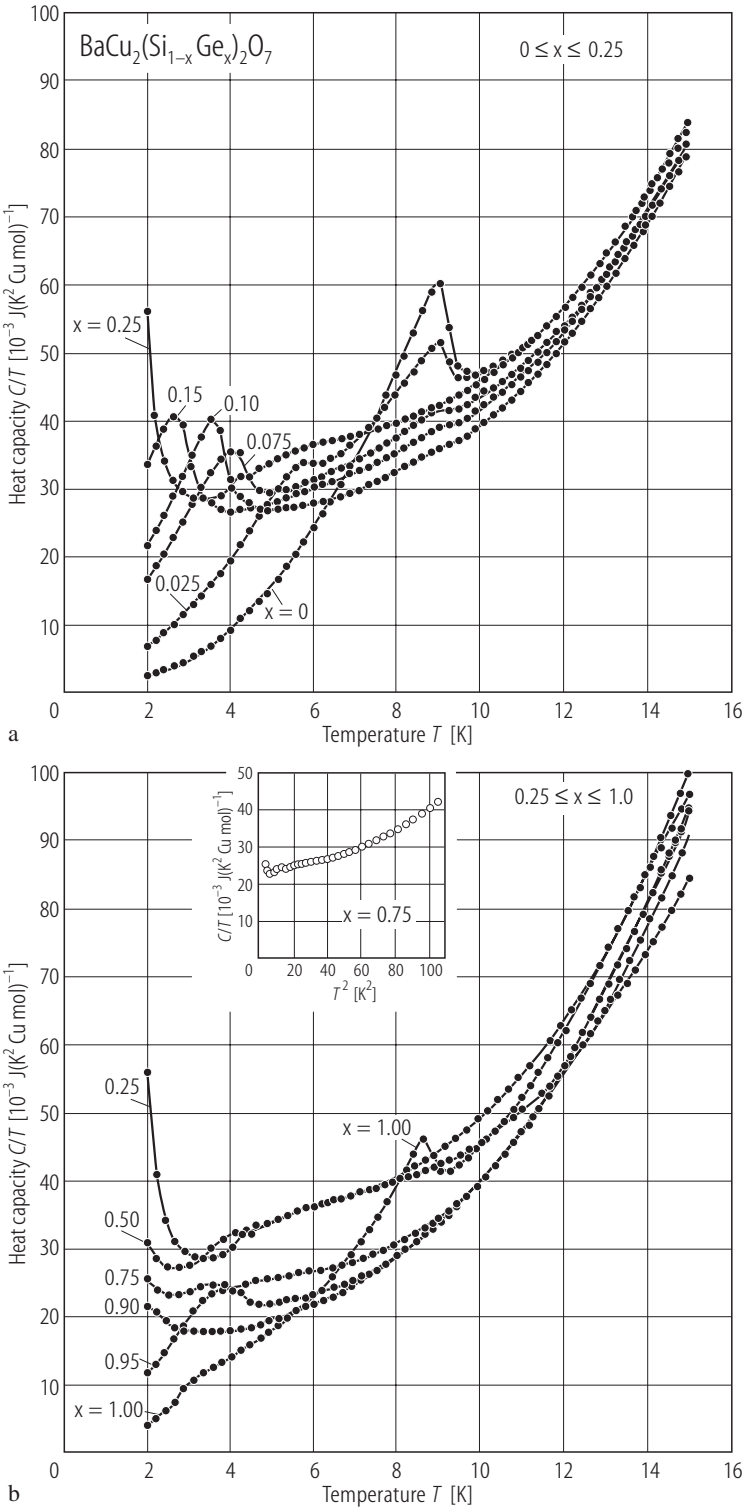


**Fig. 36.** $BaCu_2(Si_{1-x}Ge_x)_2O_7$. Temperature dependences of the specific heat $C/T$ in samples with $0 \le x \le 0.25$ **(a)** and $0.25 \le x \le 1.0$ **(b)**; the inset in **(b)** shows $C/T$ values versus $T^2$ for $T \le 10$ K and $x = 0.75$ implying that a large $T$-linear contribution remained at low temperature [01Y1].

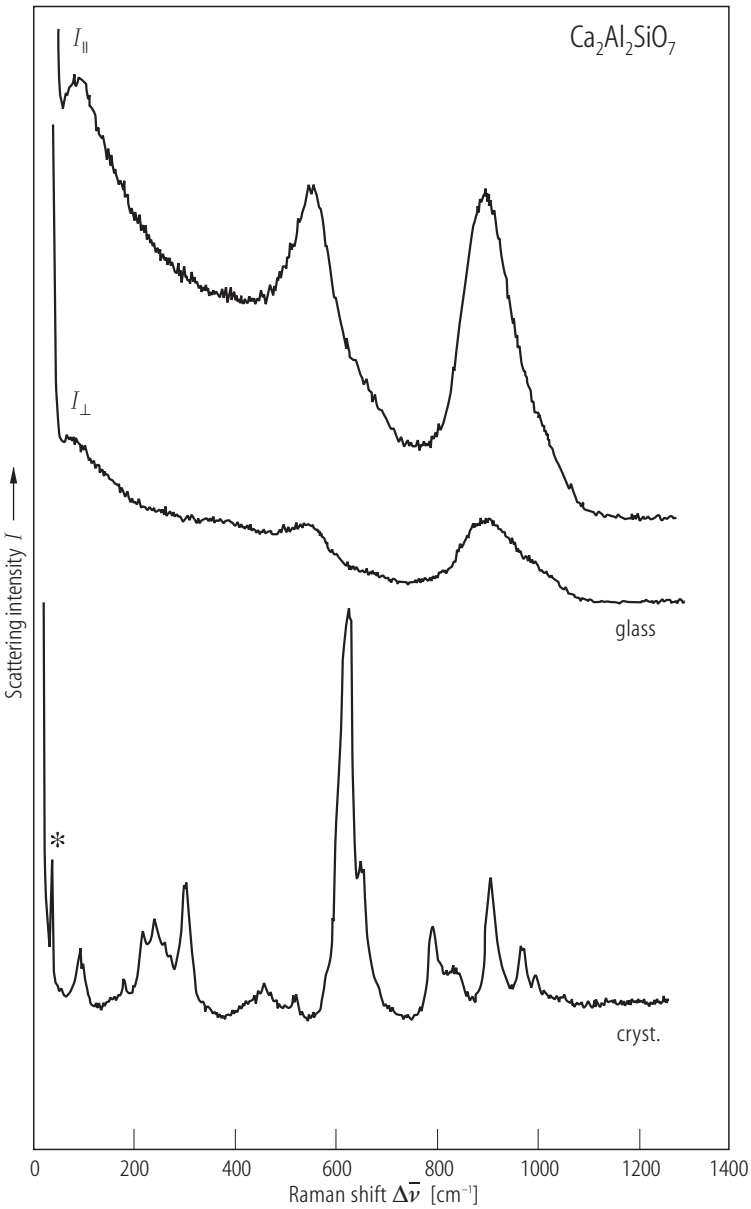


**Fig. 39.** $Ca_2Al_2SiO_7$ (crystalline and glass). Raman spectra [83S1]. $I_{\parallel}$ and $I_{\perp}$ of the glass spectra, respectively, refer to the spectra recorded with electric field vector of the scattered light parallel and perpendicular to the electric vector of the laser beam. Asterisk mark a plasma line from the laser.

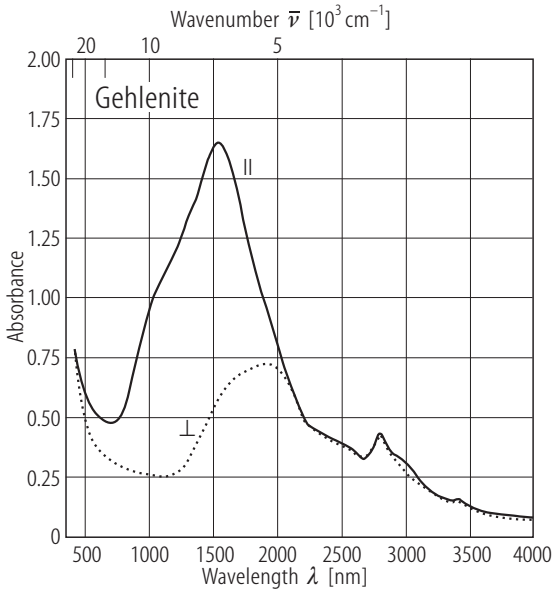


**Fig. 40.** Natural gehlenite. Polarized optical absorption spectra for a sample having thickness of 0.20 mm [01R1].

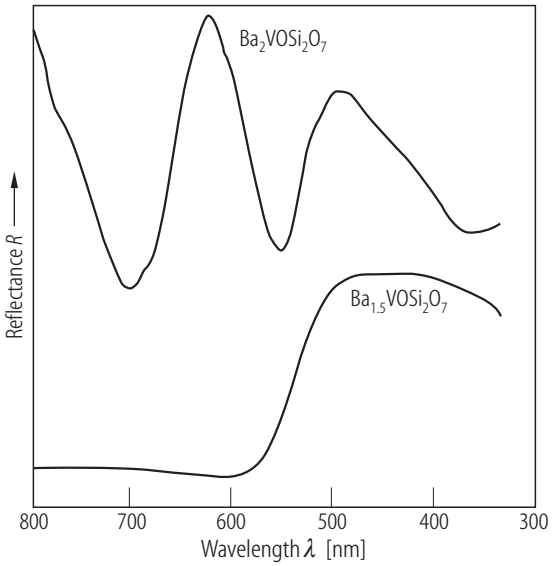


**Fig. 41.** $Ba_2VOSi_2O_7$ **(a)**, $Ba_{1.5}VOSi_2O_7$ **(b)**. Diffuse reflectance spectra [01R2].

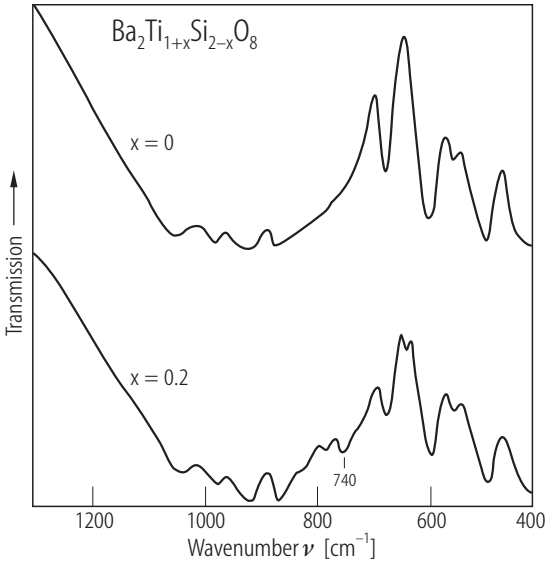


**Fig. 42.** $Ba_2Ti_{1+x}Si_{2-x}O_8$. Infrared spectra for x = 0 **(a)** and x = 0.2 **(b)** [96C1].

## References for 8.1.2.2


30R1 Raaz, F.: Anz. Akad. Wiss. Wien Math. Naturwiss. Kl. 18 (1930) 203
30W1 Warren, B.E.: Z. Kristallogr. 74 (1930) 131
30W2 Warren, B.E., Trautz, O.R.: Z. Kristallogr. 75 (1930) 525
30Z1 Zachariasen, W.H.: Z. Kristallogr. 74 (1930) 226
31Z1 Zachariasen, W.H.: Nor. Geol. Tidsskr. 12 (1931) 577
41Y1 Ygberg, E.R.: Geol. Foeren. Stockholm Foerh. 134 (1941) 394
53G1 Gloria, C.: Atti Acad. Sci. Torino, Cl. Sci. Fis. Mat. Nat. 88 (1953) 153
53S1 Smith, J.V.: Am. Mineral. 38 (1953) 643
54S1 Segnit, E.R.: J. Am. Ceram. Soc. 37 (1954) 273
57D1 Dear, P.S.: Bull. Va. Polytech. Inst. Eng. Exp. Stn. Ser. 50 (1957) 1
58D1 Durif, A., Forrat, F.: Bull. Soc. Fr. Miner. Cristallogr. 81 (1958) 107
60B1 Brisi, C., Abbattista, F.: Ann. Chim. (Roma) 50 (1960) 1061
61D1 Dear, P.S.: Bull. Va. Polytech. Inst. Eng. Exp. Stn. Ser. 54 (1961) 1
61T1 Tarte, P.: Nature 191 (1961) 1002
62P1 Peng, C.J., Tsao, R.L., Chou, Z.R.: Sci. Sin. 11 (1962) 977
64B1 Bonner, J.C., Fisher, M.E.: Phys. Rev. 135 (1964) A640
64Y1 Yoder, H.S.: Yearbook Carnegie Inst. Washington 63 (1964) 86
65A1 Alfors, J.T., Stimson, M.C., Matthews, R.A.: Am. Mineral. 50 (1965) 314
65E1 Edgar, A.D.: Can. J. Earth Sci. 2 (1965) 596
65S1 Schairer, J.F., Yoder, H.S., Tilley, C.D.: Yearbook Carnegie Inst. Washington 64 (1965) 95
67A1 Astahova, L.P., Pobedinskaya, E.A., Simonov, V.I.: Dokl. Akad. Nauk. SSSR 173 (1967) 171
67C1 Cannillo, E., Giuseppetti, G., Tazzoli, Y.: Acta Crystallogr. 23 (1967) 255
67D1 Dal Negro, A., Rossi, G., Ungaretti, L.: Acta Crystallogr. 23 (1967) 260
67K1 Kachalov, O.V., Kreines, N.M.: Zh. Exp. Fiz. 53 (1967) 858
67K2 Korczak, P., Raaz, F.: Oesterr. Akad. Wiss. Math.-Naturwiss. Kl. Sitzungsber. 13 (1967) 383
67M1 Masse, R., Grenier, J.C., Durif, A.: Bull. Soc. Fr. Mineral. Cristallogr. 90 (1967) 20
67M2 Moore, P.B., Louisnathan, S.J.: Science 156 (1967) 1361
67N1 Negro, A.D., Rossi, G., Ungaretti, L.: Acta Crystallogr. 23 (1967) 260
67S1 Sahama, T.G., Lehtinen, M.: Bull. Comm. Geol. Finl. 229 (1967) 29
69A1 Astahova, L.P., Simonov, V.I.: Kristallografiya 14 (1969) 3
69B1 Bartram, S.F.: Acta Crystallogr. B25 (1969) 791
69C1 Cannillo, E., Giuseppetti, G., Tazoli, V.: Acta Crystallogr. B25 (1969) 993
69D1 Dingle, R., Lines, M.E.: Phys. Rev. 187 (1969) 643
69I1 Ito, J., Peiser, H.H.: J. Res. Natl. Bur. Stand. Sect. A: 73 (1969) 69
69L1 Louisnathan, S.J.: Z. Kristallogr. 130 (1969) 427
69M1 Moore, P.B., Louisnathan, S.J.: Z. Kristallogr. 130 (1969) 438
69S1 Skshat, S.M., Simonov, V.I., Belov, N.V.: Dokl. Akad Nauk. SSSR 184 (1969) 337
69W1 Wöllenkle, H., Wittmann, A., Nowotny, H.: Monatsh. Chem. 100 (1969) 295
70B1 Bakakin, V.V., Belov, N.V., Borisov, S.V., Solovyeva, L.P.: Am. Mineral. 55 (1970) 1167
70B2 Barry, T.L.: J. Electrochem. Soc. 117 (1970) 381
70L1 Louisnathan, S.J.: Z. Kristallogr. 130 (1970) 314
70S1 Segnit, E.R., Holland, A.E.: Aust. J. Chem. 23 (1970) 1077
70W1 West, A.R., Glasser, F.P.: Mater. Res. Bull. 5 (1970) 837
71F1 Filipenko, O.S., Pobedinskaya, E.A., Ponomarov, V.I., Belov, I.V.: Dokl. Akad. Nauk SSSR 200 (1971) 591
71L1 Louisnathan, S.J.: Can. Mineral. 10 (1971) 822
71R1 Robinson, K., Gibbs, G.V., Ribbe, P.H.: Science 172 (1971) 567
72D1 Dubey, B.L., West, A.R.: Nat. Phys. Sci. 235 (1972) 155
72F1 Filipinko, O.S., Pobedimskaya, E.A., Ponmarev, V.I., Belov, N.V.: Vestn. Mosk. Univ. Geol. 1 (1972) 100
72K1 Korczak, P.H., Schichl, H., Raaz, F.: Fortschr. Mineral. 50 (1972) 211
74D1 De Wolff, P.M.: Acta Crystallogr. A30 (1974) 777

74H1 Haritonov, Yu.A., Golyschev, V.M., Rastzvetaeva, R.K., Belov, I.V.: Kristallografiya 19 (1974) 1078
74I1 Ito, H., Hafner, S.S.: Am. Mineral. 59 (1974) 700
74S1 Seifert, F.: Yearbook Carnegie Inst. Washington 73 (1974) 500
75K1 Khomyakov, A.P., Semenov, E.I., Bikova, A.V., Voronkov, A.A., Smolyanikova, N.N.: Dokl. Akad. Nauk. SSSR 221 (1975) 699
76E1 Eckstein, J., Recker, K., Wallrafen, F.: Naturwissenchaften 63 (1976) 453
76K1 Kimura, M., Fujino, Y., Kawamura, T.: Appl. Phys. Lett. 9 (1976) 227
77H1 Haussuhl, S., Eckstein J., Recker, K., Wallrafen, F.: J. Cryst. Growth 40 (1977) 200
77K1 Kimura, M.: J. Appl. Phys. 48 (1977) 2850
77R1 Robinson, P.D., Fang, J.H.: Am. Mineral. 62 (1977) 167
78H1 Huckenholtz, H.G., Ott, W.D.: Neues Jahrb. Mineral Monatsh. 12 (1978) 521
78L1 Liu, L.G.: Earth Planet. Sci. Lett. 40 (1978) 401
78M1 Melngailis, J., Vetelino, J.F., Jhunjhenwala, A., Reed, T.B., Fahey, R.E., Stern, E.: Appl. Phys. Lett. 32 (1978) 203
78S1 Schmid, H., Genequad, P., Tippman, H., Pouilly, G., Guedu, H.: J. Mater. Sci. 13 (1978) 2257
78Y1 Yamauchi, H.: J. Appl. Phys. 49 (1978) 6162
79B1 Blasse, G.: J. Inorg. Nucl. Chem. 41 (1979) 639
79H1 Hesse, K.F.: Acta Crystallogr. B35 (1979) 724
79M1 Maksimov, B.A., Zhdanova, T.A., Voronkov, A.A.: Dokl. Akad. Nauk. SSSR 247 (1979) 103
79S1 Sharma, S.K., Yoder, H.S.: Yearbook Carnegie Inst. Washington 78 (1979) 526
79Y1 Yamauchi, H., Yamashita, K., Takeuchi, H.: J. Appl. Phys. 50 (1979) 3160
80B1 Belov, N.V.: Itogi Nauki Tekh. Ser.: Kristallokhim. 1980, p. 14
80R1 Ragimov, K.G., Chiragov, M.I., Mamedov, H.S.: Dokl. Akad. Nauk. SSSR 253 (1980) 1130 (Sov. Phys. Dokl 25 (1980) 583)
80S1 Satiya, S.K., Axe, J.D., Shirane, G., Yoshizawa, H., Hirakawa, K.: Phys. Rev. B21 (1980) 2001
81F1 Fitton, I.G., Hughes, D.J.: Mineral. Mag. 44 (1981) 261
81H1 Halliyal, A., Bhalla, A.S., Newnham, R.E., Cross, L.E.: J. Mater. Sci. 16 (1981) 1023
81H2 Heller-Kalai, L., Rozenson, I.: Phys. Chem. Minerals 7 (1981) 223
81K1 Kimata, M., Ii, N.: Neues Jahrb. Mineral. Monatsh. 15 (1981) 1
81M1 Merinov, B.V., Maksimov, B.A., Belov, I.V.: Dokl. Akad. Nauk. SSSR 263 (1981) 1128
81M2 Merlino, S.: Acta Crystallogr. A 37 (1981) C189
81S1 Sharma, S.K.: EOS, Trans. Am. Geophys. Union 62 (1981) 425
82B1 Brown, I.D.: in Structure and Bonding in Crystals Vol. II, M. O'Keefe, A., Navrotsky, (eds.), Springer, New York, 1982, p. 1-30
82I1 Iijima, K., Marumo, F., Kimura, M., Kawamura, T.: Mineral J. 11 (1982) 107
82K1 Kimata, M.: Naturwissenschaften 69 (1982) 40
82K2 Kimata, M., Ii, N.: Neues Jahrb. Mineral. Abh. 144 (1982) 254
82K3 Kimata, M., Ohashi, H.: Neues Jahrb. Mineral. Abh. 143 (1982) 210
82L1 Liebertz, J., Stähr, S.: Z. Kristallogr. 159 (1982) 271
82O1 Otroschenko, L.L., Simonov, V.I.: Dokl. Akad. Nauk. SSSR 265 (1982) 76
82S1 Sone, K., Ohashi, H.: Bull. Chem. Soc. Jpn. 55 (1982) 3206
83B1 Baturin, S.V., Malinovskii, Yu.A., Bondareva, O.S.: Dokl. Akad. Nauk. SSSR 271 (1983) 349
83K1 Kimata, M.: Z. Kristallogr. 163 (1983) 295
83K2 Kimata, M.: Neues Jahrb. Mineral. Abh. 146 (1983) 221
83N1 Nöller, R., Knoll, H.: Solid State Commun. 47 (1983) 237
83S1 Sharma, S.K., Simons, B., Yoder, H.S.: Am. Mineral. 68 (1983) 1113
83S2 Smith, K.A., Kirkpatrick, R.J., Oldfield, E., Henderson, D.M.: Am. Mineral. 68 (1983) 1206
84G1 Grice, J.D., Robinson, G.W.: Can. Mineral. 22 (1984) 443
84H1 Hemingway, B.S., Robie, R.A.: Am. Mineral. 69 (1984) 307
84K1 Kimata, M.: Z. Kristallogr. 167 (1984) 103
84M1 Malinovskii, Yu.A.: Dokl. Akad. Nauk. SSSR 278 (1984) 616
84M2 Mägi, M., Lippmaa, E., Samoson, A., Engelhardt, G., Grimmer, A.R.: J. Phys. Chem. 88 (1984) 1518
84R1 Roult, G., Bacher, P., Liebaut, X., Marchard, R., Goursat, P., Laurent, Y.: Acta Crystallogr. A40 (1984) C266

84S1 Sigalovskaya, Yu.I., Sandomirskii, P.A., Urusov, V.S.: Mineral. Zh. 6 (1984) 3
85A1 Akasaka, M., Ohashi, H.: Phys. Chem. Miner. 12 (1985) 13
85J1 Janes, N., Oldfield, E.: J. Am. Chem. Soc. 107 (1985) 6769
85K1 Kimata, M.: Neues Jahrb. Mineral. Monatsh. (1985) 85
85M1 Markgraf, S.A., Halliyal, A., Bhala, A.S., Newnhaam, R.E., Prewitt, C.T.: Ferroelectrics 62 (1985) 17
85S1 Sandomirskii, P.A., Sigalovskaya, Yu.I., Urusov, V.S.: Mineral. Zh. 7 (1985) 8
85S2 Sebais, M., Pobedimskaya, E.A., Dimitrova, O.X.: Kristallografiya 30 (1985) 802 (Sov. Phys. Cristallogr. 30 (1985) 466)
86A1 Akasaka, M., Ohasi, H., Shimoto, I.: Phys. Chem. Miner. 13 (1986) 152
86B1 Bowen, H.K.: Sci. Am. 255 (1986) 146
86H1 Hemingway, B.S., Evans, H.T., Nord, G.L., Haselton, H.T., Robie, R.A., McGee, J.J.: Can. Mineral. 24 (1986) 425
86K1 Kaminskii, A.A., Belokoneva, E.L., Mill, B.V., Sarkisov, S.E., Kurbanov, K.: Phys. Status Solidi (a) 97 (1986) 279
86S1 Slasor, S., Liddel, K., Thompson, D.P.: Ceram. Progr. 37 (1986) 51
87D1 Dowty, E.: Phys. Chem. Miner. 14 (1987) 122
87J1 Janssen, Y., Janner, A.: Adv. Phys. 36 (1987) 519
87S1 Seifert, F., Czank, M., Simons, B., Schmahl, W.: Phys. Chem. Miner. 14 (1987) 26
88D1 Dupree, R., Lewis, M.H., Smith, M.E.: J. Am. Chem. Soc. 110 (1988) 1083
88H1 Halliyal, A., Bhalla, A.S., Markgraf, S.A., Cross, L.E., Newnhaam, R.E.: Ferroelectrics 62 (1988) 27
88S1 Sharma, S.K., Yoder, H.S., Matson, D.W.: Geochim. Cosmochim. Acta 52 (1988) 1961
88T1 Tamazyan, R.A., Malinovskii, Yu.A., Sirota, M.I., Simonov, V.I.: Kristallografiya 33 (1988) 1128 (Sov. Phys. Crystallogr. 38 (1988) 668)
89C1 Catchen, G.L., Menke, L.H., Jamil, K., Blaszkuwicz, M., Scheetz, B.E.: Phys. Rev. B39 (1989) 3826
89G1 Grice, J.D., Hawthorne, F.C.: Can. Mineral. 27 (1989) 193
89H1 Harris, R.K., Leach, M.J., Thompson, D.P.: Chem. Mater. 1 (1989) 336
89I1 Iishi, K., Fujimoto, K., Fujino, K.: Neues. Jahrb. Mineral. Monatsh. (1989) 219
89K1 Kanzaki, M., Xue, X., Stebbins, J.F.: EOS, Trans. Am. Geophys. Union 70 (1989) 1418
89M1 Merwin, L.H., Sebald, A., Seifert, F.: Phys. Chem. Miner. 16 (1989) 752
89S1 Sigalovskaya, Yu.I., Nozik, Yu.Z., Tovbis, A.B.: Sov. Phys. Crystallogr. 34 (1989) 185
90A1 Armbruster, T., Röthlisberger, F., Seifert, F.: Am. Mineral. 75 (1990) 847
90I1 Iishi, K., Fujino, K., Furukawa, Y.: Phys. Chem. Miner. 17 (1990) 467
90J1 Jaczak, J., Kuciak, R.: Acta Crystallogr. C46 (1990) 1383
90L1 Li, Z., Chan, S.K., Ghose, S.: Phys. Chem. Miner. 17 (1990) 462
90L2 Li, Z., Chan, S.K., Ghose, S.: EOS, Trans. Am. Geophysical Union 71 (1990) 619
90R1 Röthlisberger, F., Seifert, F., Czank, M.: Eur. J. Mineral.2 (1990) 585
91A1 Allik, T.H., Chain, B.H.T., Merkle, L.D.: Proc. Adv. Solid State Lasers, 1991, p. 84
91D1 Denisov, A.L., Zharikov, E.V., Zubenko, D.A., Noginov, M.A., Ostroumov, V.G., Smirnov, V.A., Kholodova, M.E., Scherbakov, I.A.: Proc. Adv. Solid State Lasers, 1991, p. 82
91F1 Fitz Gerald, J.D., Ringwood, A.E.: Phys. Chem. Miner. 18 (1991) 40
91F2 Finger, L. W., Hazen, R. M.: Acta Crystallogr. B47 (1991) 561
91G1 Garret, M.H., Chan, V.H., Jenssen, H.P., Whitmore, M.H., Sacra, A., Singel, D.J.: Proc. Adv. Solid State Lasers, 1991, p. 76
91I1 Iishi, K., Mizola, T., Fujino, K., Furukawa, Y.: Phys. Chem. Miner. 17 (1991) 720
91N1 Nickel, E.H., Nichols, M.C.: Mineral Reference Manual, Van Nostrand Reinhold, 1991
92C1 Cannillo, E., Giuseppetti, G., Mazzi, F., Tazzoli, V.: Z. Kristallogr. 202 (1992) 71
92D1 Deka, C., Bass, M., Chai, B.H.T., Zang, X.X.: Proc. Adv. Solid. State Lasers, 1992, p. 47
92S1 Shannon, R.D., Iishi, K., Allik, T.H., Rossman, G.R., Lieberetz, J.: Eur. J. Mineral. 4 (1992) 1241
92S2 Swainson, I.P., Dove, M.T., Schmahl, W.W., Putnis, A.: Phys. Chem. Miner. 19 (1992) 185
92V1 Van Heurck, Van Tendeloo, G., Amelinckx, S.: Phys. Chem. Miner. 18 (1992) 441
92W1 Webb, S.L., Ross, C.R., Lieberetz, J.: Phys. Chem. Miner. 18 (1992) 522
93A1 Adams, R.D., Layland, R., Datta, T., Payen, C.: Polyhedron 12 (1993) 2075
93A2 Amelinckx, S., Van Dyck, D.: in Electron Diffraction Techniques, Vol. 2, Ed. Coweley, J. M., Oxford University Press, Oxford, U.K., 1993, p.309-372

93H1 Hagiya, K., Ohmasa, M., Iishi, K.: Acta Crystallogr. B49 (1993) 172
93S1 Seifert, F., Röthlisberger, F.: Mineral. Petrol. 48 (1993) 179
93W1 Whitmore, M.H., Sacra, A., Singel, D.J.: J. Chem. Phys. 98 (1993) 3656
94B1 Brown, N.E., Ross, C.R., Webb, S.L.: Phys. Chem. Miner. 21 (1994) 469
94C1 Cheng, Y.B.: J. Am. Ceram. Soc. 77 (1994) 143
94I1 Iishi, K., Hagiya, K., Ohmasa, M.: Phys. Chem. Miner. 21 (1994) 6
94M1 Mizota, T., Iishi, K.: Netsu Sokutei 21 (1994) 12
94T1 Thayaparam, S., Dove, M.T., Heine, V.: Phys. Chem. Miner. 21 (1994) 110
95F1 Fleet, M. E., Hendrson, G. S.: Phys. Chem. Miner. 22 (1995) 383
95S1 Shimizu, M., Kimata, M., Iida, I.: Neues Jahrb. Mineral. Monatsh. (1995) 39
95S2 Sun, W.Y., Yan, D.S., Guo, L., Mandal, H., Thompson, D.P.: J. Eur. Ceram. Soc. 15 (1995) 349
96C1 Coats, A.M., Hirose, N., Marr, J., West, A.R.: J. Solid State Chem. 126 (1996) 105
96C2 Cruciani, G., Waccaro, C.: Plinius 16 (1996) 85
96G1 Ganster, K., Milsch, B., Rager, H.: Z. Kristallogr. Suppl. 11 (1996) 139
96K1 Koroglu, A., Apperley, D.C., Harris, D.C., Thompson, D.P.: J. Mater. Chem. 6 (1996) 1031
96M1 MacKenzie, K.J.D., Gainsford, G.J., Ryan, M.J.: J. Eur. Ceram. Soc. 16 (1996) 553
96T1 Tamura, T., Yoshiasa, A., Iishi, K., Takeno, S., Maeda, H., Emura, S., Kato, K.: Phys. Chem. Miner. 23 (1996) 81
97E1 Essler, F.H.L., Tsvelik, A.M., Delfino, G.: Phys. Rev. B56 (1997) 11001
97H1 Haussuhl, S., Echstein, J., Recker, K., Wallrefren, F.: J. Cryst. Growth 40 (1997) 200
97K1 Kimata, M., Saito, S., Shimizu, M., Nishido, N.: 17$^{th}$ Eur. Crystall. Meeting, Lisbon, Portugal, 1997 p. 156
97R1 Riester, M., Böhn, H.: Z. Kristallogr. 212 (1997) 506
97R2 Rager, H., Melch, B.: DFG Reports, Ra 554/6 and Mi 426/2 (1997)
97S1 Sugimoto, A., Nobe, Y., Yamazaki, T., Anzai, Y., Yamagishi, K., Segawa, Y., Takei, H.: Phys. Chem. Miner. 24 (1997) 326
97S2 Scott, M.A., Han, T.P.J., Gallagher, H.G., Henderson, B.: J. Lumin. 72-74 (1997) 260
97W1 Wang, P.L., Werner, P.E.: J. Mater. Sci. 32 (1997) 1025
97W2 Wang, P.L., Werner, P.E., Gao, L., Harris, R.K., Thompson, D.P.: J. Mater. Chem. 7 (1997) 2127
97Y1 Yang, H., Hazen, R.M., Downs, R.T., Finger, L.W.: Phys. Chem. Miner. 24 (1997) 510
98D1 Dupree, R., Lewis, M.H., Smith, M.E.: J. Am. Chem. Soc. 110 (1998) 1083
98J1 Jiang, J.C., Schosnig, M., Schaper, A.K., Ganster, K., Rager, H., Toth, L.: Phys. Chem. Miner. 26 (1998) 128
98K1 Kusaka, K., Ohmasa, M., Hagiya, K., Ishi, K., Haga, N.: Mineral. J. 20 (1998) 47
98Y1 Yao, G.Q., Lin, J.H., Zhang, L., Lu, G.X., Gong, M.L., Su, M.Z.: J. Mater. Chem. 8 (1998) 585
99G1 Gopalakrishanan, J., Ramesha, K., Kasthuri Rangan, K., Pandey, J.: J. Solid State Chem. 148 (1999) 75
99K1 Kusaka, K.: PhD Thesis, Himeji Institute of Technology, Japan, 1999, cited by [01H1]
99L1 Lauterbach, R., Schnick, W.: Z. Anorg. Allg. Chem. 625 (1999) 429
99L2 Lin, J.H., Lu, G.X., Du, J., Su, M.Z., Loong, C.K., Richaardson, J.W.: J. Phys. Chem. Solids 60 (1999) 975
99M1 Mandrino, J.A.: Fleischer's Mineral Species, The Mineralogical Record Inc., Tucson, 1999
99M2 McConnell, J.D.C.: Z. Kristallogr. 214 (1999) 457
99T1 Tsukada, I., Sasago, Y., Uchinokura, K., Zheludev, A., Maslov, S., Shirane, G., Kakurai, K., Ressouche, E.: Phys. Rev. B60 (1999) 6601
00B1 Bagautdinov, B., Hagiya, K., Kusaka, K., Ohmasa, M., Ishi, K.: Acta Crystallogr. B56 (2000) 811
00F1 Fang, C.M., De Wijs, G.A., De Groot, R.A., Metselaar, R., Hintzen, H.T., De With, G.: Chem. Mater. 12 (2000) 1071
00G1 Giuli, G., Bindi, L., Bonazzi, P.: Am. Mineral. 85 (2000) 1512
00L1 Lu, G.X., Yang, L.Q., Lin, J.N.: Solid State Commun. 114 (2000) 113
00M1 Mc Connell, J.D.C., Mc Cannon, C.A., Angel, R.J., Seifert, F.: Z. Kristallogr. 215 (2000) 669
00M2 Matijasic, A., Marler, B., Patarin, J.: Int. J. Inorg. Mater. 2 (2000) 209
00R1 Riester, M., Böhm, H., Petricek, P.H.: Z. Kristallogr. 215 (2000) 102

00Y1 Yuan, J., Fu, P., Wang, J., Guo, F., Yang, Z., Wu, Y.: Progress Crystal Growth and Characterization (2000) 103
00Z1 Zheludev, A., Kenzelmann, M., Raymond, S., Ressouche, E., Masuda, T., Kakurai, K., Maslov, S., Tsukada, I., Uchinokura, K., Wildes, A.: Phys. Rev. Lett. 85 (2000) 4799
01B1 Bindi, L., Gank, M., Röthlisberger, F., Bonazzi, P.: Am. Mineral. 86 (2001) 747
01H1 Hagiya, K., Kusaka, Ohmasa, M., Iishi, K.: Acta Crystallogr. B57 (2001) 271
01K1 Kenzelmann, M., Zheludev, A., Raymond, S., Ressouche, E., Masuda, T., Böni, P., Kakurai, K., Tsukada, I., Uchinokura, K., Coldea, R.: Phys. Rev. B64 (2001) 054422
01K2 Kusaka, K., Hagiya, K., Ohmasa, M., Okano, Y., Mukai, Iishi, K., Haga, N.: Phys. Chem. Miner. 28 (2001) 150
01R1 Rossman, G.R., Taran, M.N.: Am. Mineral. 86 (2001) 896
01R2 Ramesha, K., Gopalakrishnan, J.: Solid State Science 3 (2001) 113
01S1 Schaper, A. K., Schosing, M., Kutoglu, A., Treutmann, W., Rager, H.: Acta Crystallogr. B57 (2001) 443
01Y1 Yamada, T., Hiroi, Z., Takano, M.: J. Solid State Chem. 156 (2001) 101
02B1 Bagautdinov, B., Hagiya, K., Naguchi, S., Ohmasa, M., Ikeda, N., Kusaka, K., Iishi, K.: Phys. Chem. Miner. 29 (2002) 346
02K1 Kahlenberg, V., Hösch, A.: Z. Kristallogr. 217 (2002) 155